
π^0 electroproduction from $\Delta(1232)$ at high momentum
transferred with CLAS

by Maurizio Ungaro

Version 1.4.1 (2009/05/11)

ABSTRACT

The $N \rightarrow \Delta$ transition has played a major role for many years in understanding the structure of the nucleon. The electromagnetic quadrupole to dipole ratios $R_{EM} = E_{1+}/M_{1+}$ and $R_{SM} = S_{1+}/M_{1+}$ of the transition are considered key observables in the study of the dynamics of baryons.

The object of this analysis is the study of unpolarized π^0 electroproduction of the $\Delta(1232)$ resonance at high Q^2 produced in Hall B at Jefferson Laboratory. The electron beam had an energy of 5.75 GeV and impinged on a cryogenic Hydrogen target. The experiment was performed between September 2001 and January 2002.

The CLAS spectrometer was used to detect the scattered electron and final state proton, and the π^0 was reconstructed by the missing mass technique.

The π^0 angular distributions were obtained over the full c.m. angles coverage for a Q^2 range 2 to 6 GeV^2/c^2 . The quantities R_{EM} and R_{SM} have been extracted using two methods: a multipole truncation technique that assumes M_{1+} dominance in the $\Delta(1232)$ region, and the JANR fit, which is based on the JLAB isobar model.

CONTENTS

ABSTRACT	2
LIST OF TABLES	6
LIST OF FIGURES	7
1. Data processing	1
1.1 SEB and PID	1
1.2 Electron identification	1
1.2.1 Čerenkov signal cut	2
1.2.2 Total energy in the calorimeter	2
1.2.3 Minimum p cut	3
1.2.4 EC_{out}/p vs EC_{in}/p cut	5
1.2.5 E_{in}/E_{out} cut	5
1.2.6 Track position cut	5
1.3 Proton Identification	9
1.4 Vertex correction and cut	13
1.5 Electron Fiducial cuts	17
1.5.1 ϕ boundaries	17
1.5.2 θ versus momentum cuts	21
1.6 Proton Fiducial cuts	23
1.6.1 ϕ boundaries	23
1.6.2 θ versus momentum cuts	29
1.7 Kinematic corrections	31
1.7.1 Beam Energy measurement	31
1.7.2 Elastic selection	31
1.7.3 Angle corrections	35
1.7.4 Momentum corrections	41
1.8 Bethe Heitler processes	45
1.9 Čerenkov efficiency	52

2.	Acceptance	54
2.1	Geometrical acceptance	54
2.2	MonteCarlo simulation	56
2.2.1	Drift Chamber smearing	56
2.2.2	Time of flight smearing	59
2.2.3	Drift chamber inefficiencies	60
2.3	Bethe Heitler events	64
2.4	Comparison between data and MonteCarlo	67
2.5	Acceptance calculation	69
3.	Analysis	71
3.1	Bins size	71
3.2	Bin averaging correction	72
3.3	Raw data	73
3.4	Radiative correction	75
3.5	Extraction of the structure functions	78
3.6	Multipole Truncation Analysis	80
3.6.1	Legendre expansion	80
3.6.2	The M_{1+} dominance assumption	87
3.6.3	Effect of M_{1+} dominance and $\ell \leq 2$ approximation	87
3.6.4	Multipole Truncation Results for R_{EM} and R_{SM}	94
3.6.5	Amplitudes of M_{1-} , E_{0+} , S_{0+}	96
3.7	The JANR fit	98
3.7.1	JANR Results for R_{EM} and R_{SM}	102
3.8	Different models and the P_{11} signal	105
3.9	Conclusions	111
4.	Systematic Errors Study	112
4.1	Calculation of the c.m. angle θ^*	112
4.1.1	The Lorentz Method	112
4.1.2	The Invariant Method	112
4.1.3	Comparison	113
4.1.4	Conclusions	115
4.2	Missing mass cuts	121

4.3 $\cos \theta^*$ cuts	123
4.4 χ^2 plots for the systematic studies	125
LITERATURE CITED	126
APPENDICES	
A. Kinematic variables	129
B. Summary of cuts used	131
B.1 Electron particle id cuts	131
B.1.1 Čerenkov signal cut	131
B.1.2 Total energy in calorimeter and lower momentum cut	131
B.1.3 Inner - Outer energy in calorimeter cut	131
B.1.4 Inner / Outer energy cut	131
B.2 Proton particle id cuts	131
B.2.1 Electron fiducial cuts	132
B.2.2 Electron bad regions	132
B.2.3 Proton fiducial cuts	133
B.2.4 Proton bad regions	135
C. $\cos \theta^*$ plots	137

LIST OF TABLES

1.1	The 6 parameters for electron fiducial cut for each of the 6 sectors.	20
2.1	Number of wires in each layer	61
2.2	Example of 18 wires sample from real CLAS data	63
3.1	The binning in Q^2	71
3.2	Results for R_{EM} and R_{SM} in the multipole truncation analysis.	94
4.1	Missing mass cuts	121
4.2	$\cos \theta^*$ cuts	123

LIST OF FIGURES

1.1	The CC signal threshold cut	3
1.2	E_{tot} and p_{min} cut	4
1.3	EC_{out}/p vs EC_{in}/p cut	6
1.4	The E_{in}/E_{tot} cut.	7
1.5	Track coordinates (x, y) cut	8
1.6	β versus momentum for positive particles in e1-6 running period	10
1.7	TOF mass spectra for CLAS	12
1.8	x and y position of the vertex at the window	13
1.9	The vertex correction	14
1.10	The vertex correction effect on electron z distributions for each sector .	15
1.11	Δz versus $z_{electron}$ uncorrected (top) and corrected (bottom) for all sectors	16
1.12	ϕ versus θ for sector 1 electrons before the electron ID	17
1.13	ϕ versus θ for sector 1 and $p = 1.6 - 1.9$ GeV	18
1.14	ϕ distributions (sector 3) for different θ and $p = 1.9 - 2.2$ GeV	19
1.15	The electron fiducial cut for sector 1	20
1.16	θ versus p for sector 5	21
1.17	ϕ versus θ distribution for sector 6 after fiducial cuts	22
1.18	ϕ versus θ for sector 5 protons	23
1.19	The trapezoid function used for the ϕ fit	24
1.20	Trapezoid fit for sector 5	25
1.21	Result of the trapezoid fit	26
1.22	Sector 5 parameters fit	27
1.23	Sector 5 $\Delta\phi$ fiducial cut as a function of θ and ϕ	28
1.24	θ versus p for protons sector 5	29

1.25	Sector 5 ϕ versus θ after fiducial cut	30
1.26	Radiative elastic events	33
1.27	The cuts for elastic selection for sector 2	34
1.28	ΔE as a function of ϕ for electrons in sector3	35
1.29	The constraint of elastic scattering	36
1.30	The angle correction algorithm	37
1.31	The combined angle correction for electron and proton for different θ slices	38
1.32	Angle correction parameters as a function of θ for sector 1	39
1.33	ΔE as a function of ϕ for each sector	40
1.34	W distribution as a function of electron ϕ for elastic events after angle corrections	41
1.35	Fits of the third order polynomial parameters as a function of θ for sector 3	42
1.36	Fits of the Δp distributions for different θ slices as a function of ϕ . . .	43
1.37	The W versus ϕ distribution for electrons in sector 1 before (left) and after (right) momentum correction	44
1.38	Missing mass M_X^2 versus W after particle ID, vertex fiducial cuts and kinematic corrections for the whole e1-6 data	45
1.39	Bethe Heitler events contributing to the (eP) final state	46
1.40	$\phi_P^{c.m.}$ versus missing mass M_x^2 for different W values	47
1.41	missing mass M_x^2 versus $\Delta\theta$ for different W values before the $\phi_P^{c.m.}$ versus missing mass M_x^2 cut	48
1.42	missing mass M_x^2 versus $\Delta\theta$ for different W values after the $\phi_P^{c.m.}$ versus missing mass M_x^2 cut	49
1.43	missing mass M_x^2 versus $\Delta\theta_2$ after the first two B.H. cuts	50
1.44	The effect of all the cuts on the W and missing mass M_x^2 distributions .	51
1.45	The $nphe$ spectra for $1.1 < p < 1.5$ GeV, $35^0 < \theta < 45^0$, $15^0 < \phi < 25^0$.	53

2.1	Geometrical acceptance for $W = 1.25 \pm 0.01$ GeV and Q^2 from 3.79 to 4.52 GeV^2 as a function of $\cos \theta^*$ and ϕ^*	55
2.2	A charged particle passing through a DC cell	56
2.3	The space residual for DC Region 3	57
2.4	The σ of the space residual for DC Region 3	58
2.5	Comparison of real data and MonteCarlo DC resolution for Region 2.	58
2.6	Square of TOF mass M^2	59
2.7	The timing resolution as determined from cosmic ray tests	60
2.8	σ as a function of the smearing factor f	61
2.9	Drift chamber occupancy distribution for sector 6	62
2.10	The next neighbor technique: the <i>buddies</i> histogram	63
2.11	Comparison between real and simulated efficiency.	64
2.12	$\phi_P^{c.m.}$ versus missing mass M_x^2 for different W values for the MonteCarlo events	65
2.13	Missing mass M_x^2 spectra for data and MonteCarlo	66
2.14	Missing mass M_x^2 spectra for data and MonteCarlo	67
2.15	Comparison Geometrical and MonteCarlo acceptances, $1.26 \leq W \leq 1.28$ GeV and $Q^2 = 3.0$ GeV^2	69
2.16	Comparison Geometrical and MonteCarlo acceptances, $1.30 \leq W \leq 1.32$ GeV and $Q^2 = 4.2$ GeV^2	70
3.1	W and Q^2 binning for π^0 events	71
3.2	$\cos \theta^*$ and ϕ^* binning for π^0 events	72
3.3	The bin correction	73
3.4	Bin averaging correction.	74
3.5	Feynman diagrams for the Born and radiative processes	76
3.6	Radiative correction as a function of $\cos \theta^*$ and ϕ^* for $W = 1.23$ GeV and $Q^2 = 3$ GeV^2	77
3.7	ϕ fits of the cross section for different $\cos \theta$ values	79

3.8	Reduced χ^2 distribution of the ϕ fits	80
3.9	$\sigma_L + \epsilon\sigma_T$ for different W at $Q^2 = 2.4$ GeV 2	82
3.10	σ_{TT} for different W at $Q^2 = 2.4$ GeV 2	83
3.11	σ_{LT} for different W at $Q^2 = 2.4$ GeV 2	84
3.12	Reduced χ^2 distribution of the Legendre fits	85
3.13	Legendre coefficients at $Q^2 = 2.4$ GeV 2	86
3.14	$Re(E_{1+}M_{1+}^*)$ as a function of W for different Q^2	88
3.15	$Re(S_{1+}M_{1+}^*)$ as a function of W for different Q^2	89
3.16	Comparison between the model (dashed blue line) and extracted (red points) multipole ratios for MAID 2000	90
3.17	Comparison between the model (dashed blue line) and extracted (red points) multipole ratios for DMT 2001	91
3.18	Model and extracted E_{1+}/M_{1+} as a function of Q^2	92
3.19	Model and extracted S_{1+}/M_{1+} as a function of Q^2	93
3.20	Result for R_{EM} as a function of Q^2	95
3.21	Result for R_{SM} as a function of Q^2	95
3.22	Amplitude of M_{1-}	96
3.23	Amplitudes of E_{0+} and S_{0+}	97
3.24	JANR fit of the cross section.	98
3.25	JANR fit of the cross section: $\sigma_T + \epsilon_L\sigma_L$	99
3.26	JANR fit of the cross section: $\sigma_T + \epsilon_L\sigma_L$	100
3.27	JANR fit of the cross section: $\sigma_T + \epsilon_L\sigma_L$	101
3.28	JANR result for R_{EM} as a function of Q^2	102
3.29	JANR result for R_{SM} as a function of Q^2	103
3.30	JANR truncated result for R_{EM} as a function of Q^2	104
3.31	Coefficients of the Legendre expansion of $\sigma_T + \epsilon_L\sigma_L$ for the JANR generated cross section and experimental data	106

3.32	Coefficents of the Legendre expansion of $\sigma_T + \epsilon_L \sigma_L$ for the maid 2002 generated cross section and experimental data	107
3.33	Coefficents of the Legendre expansion of $\sigma_T + \epsilon_L \sigma_L$ for the DMT generated cross section and experimental data	108
3.34	Coefficents of the Legendre expansion of $\sigma_T + \epsilon_L \sigma_L$ for the maid 2003 with Roper on generated cross section and experimental data	109
3.35	Coefficents of the Legendre expansion of $\sigma_T + \epsilon_L \sigma_L$ for the maid 2003 with Roper off generated cross section and experimental data	110
4.1	Schematics of π^0 electroproduction	113
4.2	Generated, Lorentz and Invariant reconstructed $\cos\theta^*$ distribution for $Q^2 = 3.5 \text{ GeV}^2$. All histograms are normalized to 1.	114
4.3	Acceptance for $W = 1.23 \text{ GeV}$ and $Q^2 = 3.0 \text{ GeV}^2$. Blue: Lorentz method. Red: Invariant method. The differences of the two methodes are maximum at the extremes $\cos\theta^*$, especially at $\cos\theta^* = -0.9$	115
4.4	C.m. cross section for $W = 1.23 \text{ GeV}$ and $Q^2 = 3.0 \text{ GeV}^2$. Blue: Lorentz method. Red: Invariant method. the two methods are similar except at the $\cos\theta^*$ extremes.	116
4.5	$\sigma_T + \epsilon\sigma_L$ for $Q^2 = 3.0 \text{ GeV}^2$. Blue: Lorentz method. Red: Invariant method. Note that the curvature of $\sigma_T + \epsilon\sigma_L$ at the Δ pole determines the amplitude of the electric quadrupole E_{1+} . See also Figure 4.6	117
4.6	The coefficients of the $\sigma_T + \epsilon\sigma_L$ expansions as a function of W for the Invariant and Lorentz method. Blue: Lorentz method. Red: Invariant method. The A_2 coefficient at the Δ pole differs by a factor of two. A non zero value of the A_3 , A_4 coefficients would be the signal of $\ell > 1$ components of the (π^0, p) orbital angular momentum.	118
4.7	The E_{1+}/M_{1+} and S_{1+}/M_{1+} ratios calculated using the truncated multipole analysis for the Invariant and Lorentz method. Blue: Lorentz method. Red: Invariant method. The big discrepancy for E_{1+}/M_{1+} is due to the curvature difference of the $\sigma_T + \epsilon\sigma_L$ at the Δ pole.	119
4.8	Missing mass square distribution for π^0 events and the different cuts used for the systematic study.	121
4.9	Variation of the ratios R_{EM} (top) and R_{SM} (bottom) for the missing mass square cuts: $-0.05 < mm^2 < 0.08$ and $-0.02 < mm^2 < 0.06$	122
4.10	Different cuts for $\cos\theta^*$ as shown in Table 4.2. The distribution comes from the MonteCarlo reconstructed events, and it's normalized to 1.	123

4.11	Variation of the ratios R_{EM} (top) and R_{SM} (bottom) for the $\cos\theta^*$ cuts: $-1 < \cos\theta^* < 1$ and $-0.95 < \cos\theta^* < 0.95$	124
A.1	Schematics of π^0 electroproduction	129
C.1	Generated, Lorentz and Invariant reconstructed $\cos\theta^*$ distribution for $Q^2 = 2 \text{ GeV}^2$. All histograms are normalized to 1.	137
C.2	Generated, Lorentz and Invariant reconstructed $\cos\theta^*$ distribution for $Q^2 = 2.4 \text{ GeV}^2$. All histograms are normalized to 1.	138
C.3	Generated, Lorentz and Invariant reconstructed $\cos\theta^*$ distribution for $Q^2 = 3 \text{ GeV}^2$. All histograms are normalized to 1.	139
C.4	Generated, Lorentz and Invariant reconstructed $\cos\theta^*$ distribution for $Q^2 = 3.5 \text{ GeV}^2$. All histograms are normalized to 1.	140
C.5	Generated, Lorentz and Invariant reconstructed $\cos\theta^*$ distribution for $Q^2 = 4.2 \text{ GeV}^2$. All histograms are normalized to 1.	141
C.6	Generated, Lorentz and Invariant reconstructed $\cos\theta^*$ distribution for $Q^2 = 5 \text{ GeV}^2$. All histograms are normalized to 1.	142
C.7	Generated, Lorentz and Invariant reconstructed $\cos\theta^*$ distribution for $Q^2 = 6 \text{ GeV}^2$. All histograms are normalized to 1.	143

CHAPTER 1

Data processing

1.1 SEB and PID

During the data processing the particle ID is done in two ways, so that two bos banks contain the calculated four momenta of all the particles in the event, the EVNT and PART banks. EVNT is based on the SEB algorithm (Simple Event Builder) while PART is based on the PID algorithm. Both yield similar result for all the particles except the electrons, where PID is more restrictive than SEB.

The resulting particle ID is not final. What follows illustrates the work to refine and improve it.

1.2 Electron identification

Only 1/3 of the triggers during the initial data processing have reconstructed negative tracks, and out of these only 1/2 are identified as containing an electron. In this identification, there is still a pion contamination problem. The *candidate electron* of this analysis is the combination of

- Any reconstructed PART bank electron.
- Any reconstructed EVNT bank electron.
- Any negative unknown PART bank particle if there is no PART bank electron.
- Any negative unknown EVNT bank particle if there is no EVNT bank electron.

There are 6 ID cuts defining a *good electron* starting from a *candidate electron* based on its momentum p , its signal in the Čerenkov $nphe$, its signals in the forward calorimeter (total energy EC_{tot} , inner energy EC_{in} , outer energy EC_{out}) and its position on the EC (x, y):

- Čerenkov npe cut
- minimum p cut
- EC_{tot}/p versus p cut
- EC_{out}/p vs EC_{in}/p cut
- EC_{in} / EC_{tot} cut
- x_{EC} vs y_{EC} cut

Each cut is discussed below.

1.2.1 Čerenkov signal cut

A threshold for the signal in the Čerenkov detector (CC) is necessary to eliminate electronic noise and the fact that pions produce Čerenkov light when their momentum is above ~ 2.5 GeV.

The signal from the CC is amplified by 10 and converted in *number of photoelectrons* (nphe). Fig.1.1 shows the cut used:

$$nphe > 2.5$$

1.2.2 Total energy in the calorimeter

In the momentum range detected at CLAS, when going through the forward calorimeter charged pions are minimum ionizing particles, while electrons shower with a total energy deposition E_{tot} proportional to their momentum P . Hence E_{tot}/P should be constant. In reality this ratio shows a slight momentum dependance as it is illustrated in Figure 1.2 where the E_{tot}/P distribution is plotted versus P . This distribution was sliced along P and each slice is fitted with a gaussian distribution, giving the mean and sigma as a function of p :

$$\begin{aligned}\bar{p} &= \bar{p}(p) \\ \sigma &= \sigma(p)\end{aligned}$$

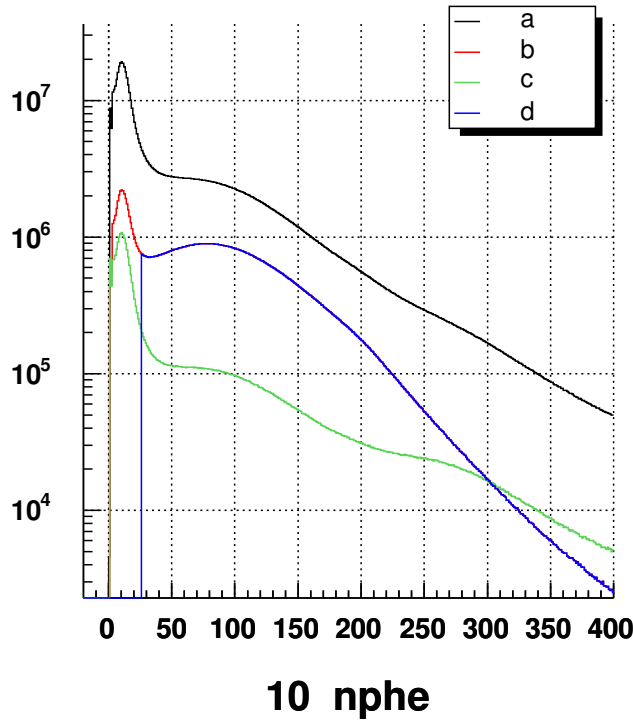


Figure 1.1: The CC signal threshold cut: 10 nphe.

(a) all electrons. (b) electrons with all other ID cuts (aside from Čerenkov cut) applied. One can see that the signal at 100 (~ 10 nphe) is enhanced while the noise at $nphe \sim 10$ is suppressed. (c) electrons with all other ID anti-cuts (aside from Čerenkov cut) applied. This events corresponds to the pions and the noise. (d) electrons with all ID cuts applied.

A second order polynomial is fitted to those distributions and events are accepted if they occur within 3σ around \bar{p} , i.e. if

$$\bar{p} - 3\sigma \leq E_{tot}/P \leq \bar{p} + 3\sigma$$

The cut is shown in Figure 1.2 as dotted red lines. The function is reported in B.1.2.

1.2.3 Minimum p cut

A study [18] of the inclusive cross section at various beam energies in CLAS results in a low momentum cut p_{min} depending on the calorimeter low total threshold (in milliVolts) of the trigger discriminator:

$$p_{min} (MeV) = 214 + 2.47 \times EC_{threshold}(mV)$$

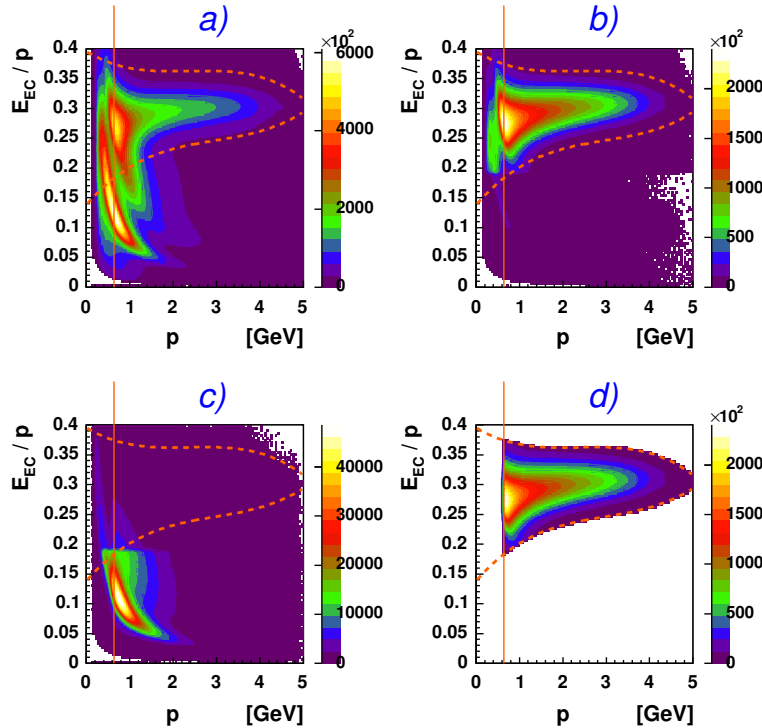


Figure 1.2: E_{tot} and p_{min} cut. For minimum ionizing particles E_{tot} is constant so they show as an hyperbole. The vertical line represents the p_{min} cut. The remaining two dashed lines are the $\bar{p} \pm 3\sigma$ cuts. (a) all electrons. (b) electrons with all other ID cuts (aside from E_{tot} and p_{min} cuts) applied. The band corresponding to minimum ionizing particles disappears almost completely. (c) electrons with all other ID anti-cuts (aside from E_{tot} and p_{min} cuts) applied. These events correspond to minimum ionizing particles and background. (d) electrons with all ID cuts applied.

The threshold for e1-6 was 172 mV therefore the minimum momentum cut is fixed at:

$$p_{min} = 0.64 \text{ GeV}$$

The cut is shown in Figure 1.2 as a vertical line.

1.2.4 EC_{out}/p vs EC_{in}/p cut

The outer EC is $5/3$ times larger than the inner EC. Therefore pions, which do not shower and are minimum ionizing, release a small quantity of energy in the outer and inner part in the ratio $5 : 3$. On the other hand electrons release a lot more energy because they shower. Due to the shower geometry electrons release more energy in the inner part than in the outer part.

The quantity E_{in}/p is plotted versus E_{out}/p in Figure 1.3. One can see the pions along the cyan line $y = \frac{5}{3}x$ and the electrons on the right part of the red line, which represents the cut and assumes the form

$$y = 0.19 - x$$

A bug in the reconstruction code sometimes gives a wrong (zero) values for E_{in} , E_{out} . For those events, this cut was not applied.

1.2.5 E_{in}/E_{out} cut

Electrons release more energy in the inner part of the calorimeter than in the outer part because of the shower conformation. This can be seen in Figure 1.4 where E_{in}/E_{out} is plotted against p .

By looking at the plot, a low threshold cut on E_{in}/E_{TOT} is introduced at 40%:

$$E_{in}/E_{TOT} \geq 0.4$$

The cut is shown in the figure as an horizontal red line.

1.2.6 Track position cut

Electrons that shower near the edges of the calorimeter will not loose all their energy in the detector because the shower is truncated. Hence their energy cannot be properly reconstructed.

For this reason a fiducial cut is introduced on the track coordinates x, y of the electrons at the EC plane. The cut is illustrated in Figure 1.5.

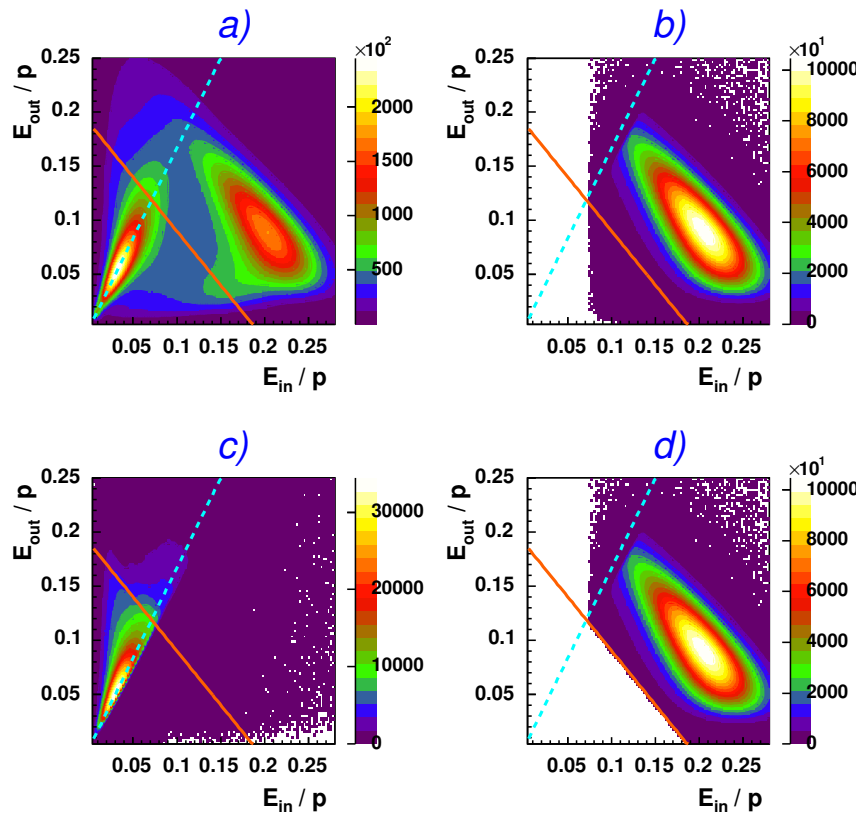


Figure 1.3: EC_{out}/p vs EC_{in}/p cut. (a) all electrons. (b) electrons with all other ID cuts (aside from EC_{out}/p vs EC_{in}/p cut) applied. The band corresponding to minimum ionizing particles disappears almost completely. (c) electrons with all other ID anti-cuts (aside from EC_{out}/p vs EC_{in}/p cut) applied. This corresponds to minimum ionizing particles and background. (d) electrons with all ID cuts applied.

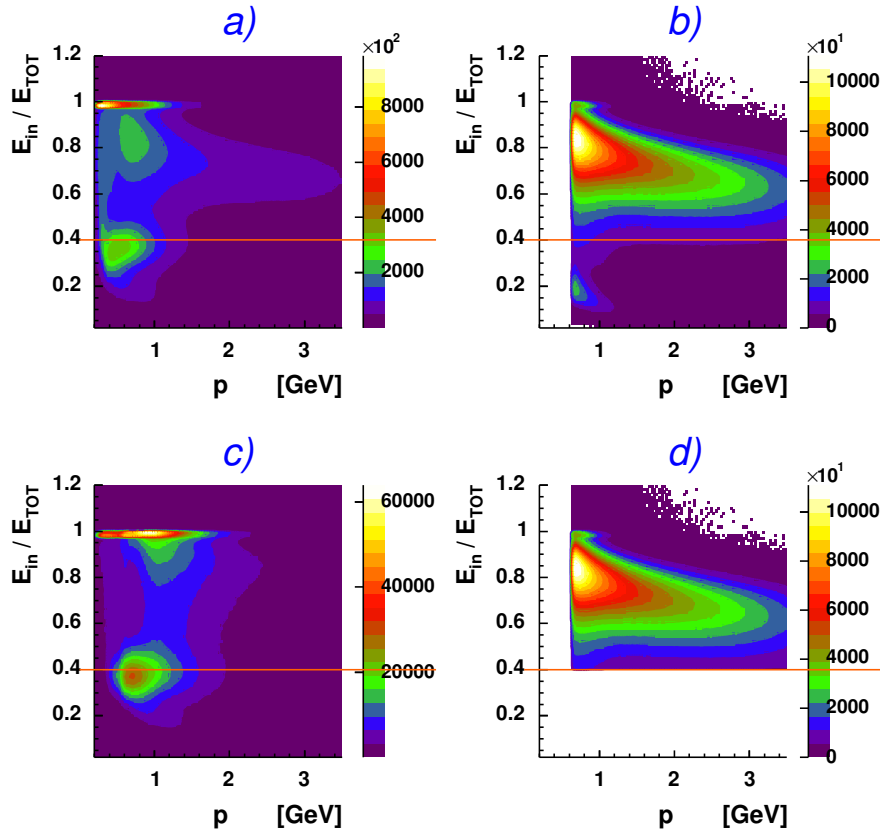


Figure 1.4: The E_{in}/E_{tot} cut. Particles that are stopped in the inner part (hence have small energy) have $E_{in} = E_{tot}$ so they show up at $E_{in}/E_{tot} = 1$. Most of these are cut out with the ID cuts. (a) all electrons. (b) electrons with all other ID cuts (aside from E_{in}/E_{tot} cut) applied. (c) electrons with all other ID anti-cuts (aside from E_{in}/E_{tot} cut) applied. Minimum ionizing particles are enhanced here. They release comparable energy in the inner and outer part. Since the inner part is 3/8 of the total calorimeter, they peak in this plot at $3/8 = 0.375\%$. (d) electrons with all ID cuts applied.

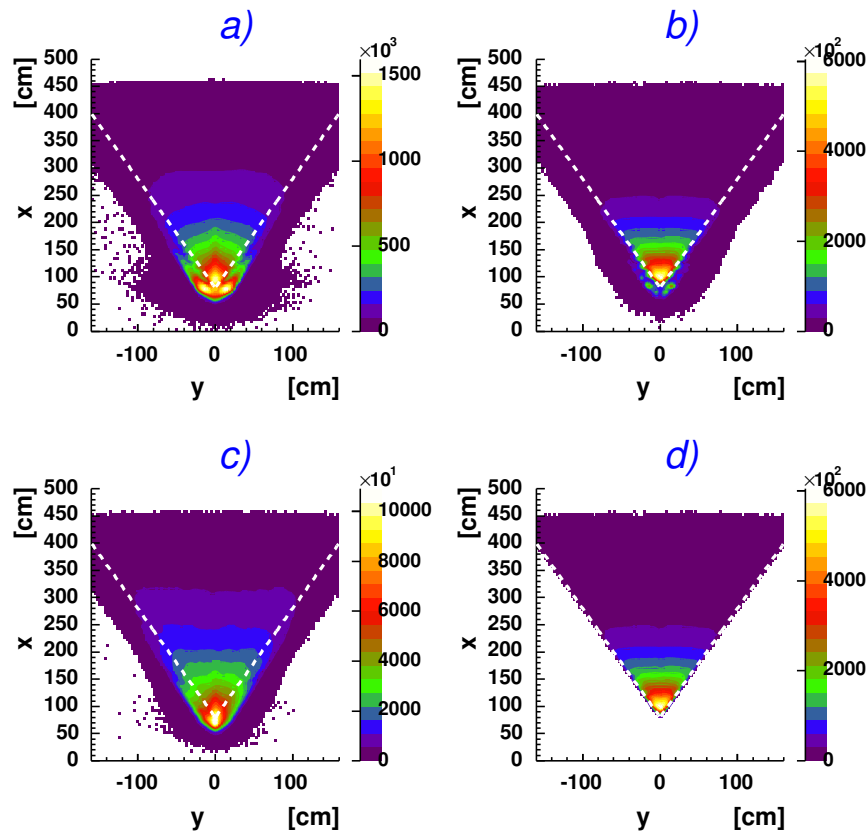


Figure 1.5: Track coordinates (x, y) cut. (a) all electrons. (b) electrons with all other ID cuts (aside from E_{in}/E_{tot} cut) applied. The x, y cut is chosen so that it encompass the electrons in this plot. (c) electrons with all other ID anti-cuts (aside from E_{in}/E_{tot} cut) applied. (d) electrons with all ID cuts applied.

1.3 Proton Identification

During the event reconstruction tracks are labelled with particle types depending on their **speed**, their **momentum** and how they bend in the magnetic field.

The momentum of the track is calculated during the event reconstruction with the tracking procedure [37]. To determine the speed of the track, a start time T_0 is calculated as

$$T_0 = T_{el} - \frac{\ell}{c} - \frac{z - z_0}{c}$$

where T_{el} is the electron time from TOF measurement, z is the vertex position of the electron track, ℓ is the pathlength of the electron track from its vertex to its TOF hit, z_0 is the z position of the center of the target¹ and c is the speed of light. The starttime is used as the reference for all the remaining tracks in the event.

The speed β for each track with pathlength ℓ and TOF time T is therefore calculated as

$$\beta = \frac{v}{c} = \frac{1}{c} \frac{\ell}{T - T_0}$$

In Figure 1.6 is plotted beta versus momentum for all particles after the electron particle ID. One can clearly see bands corresponding to pions, kaons, protons, deuterons.

The calculation of the mass of the track M (referred as TOF Mass) is straightforward from β and p :

$$M^2 = \frac{p^2(1 - \beta^2)}{\beta^2}$$

M is the quantity upon which the software reconstruction is based to determine the particle ID.

In the main torus configuration of e1-6 running period negative particles bend toward the beam line and positive particles bend away from it. Every outbending EVNT or PART track in each event is considered a *proton candidate*.

M is plotted for the candidates in Figure 1.7 where the y-axis is logarithmic. One can see a well defined proton peak.

¹For this experiment $z_0 = -4$ cm.

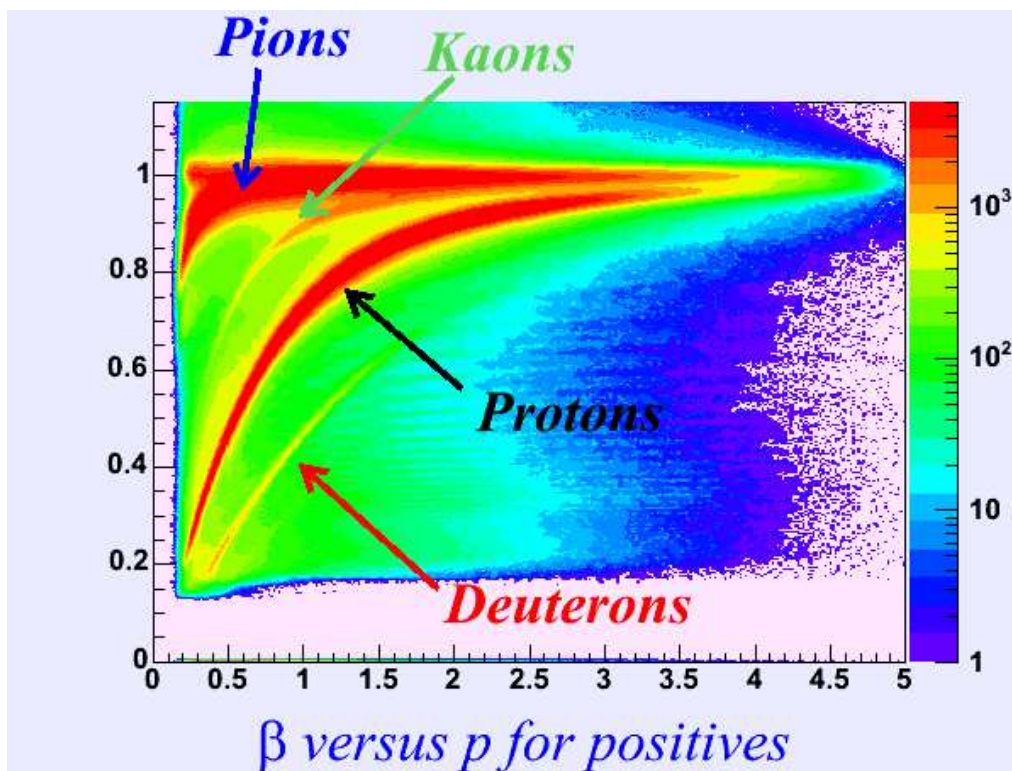


Figure 1.6: β versus momentum for positive particles in e1-6 running period. Bands corresponding to pions, kaons, protons and deuterons are visible.

For the proton, the default cut is $0.8 \leq M \leq 1.2$. The proton ID has been redone relaxing the default cut. Kinematic constrains will get rid of possible ambiguities between protons and other particles and background.

The cut used in this analysis, illustrated in Figure 1.7, is simply:

$$0.6 \leq M \leq 1.6$$

and it is illustrated in Figure 1.7.

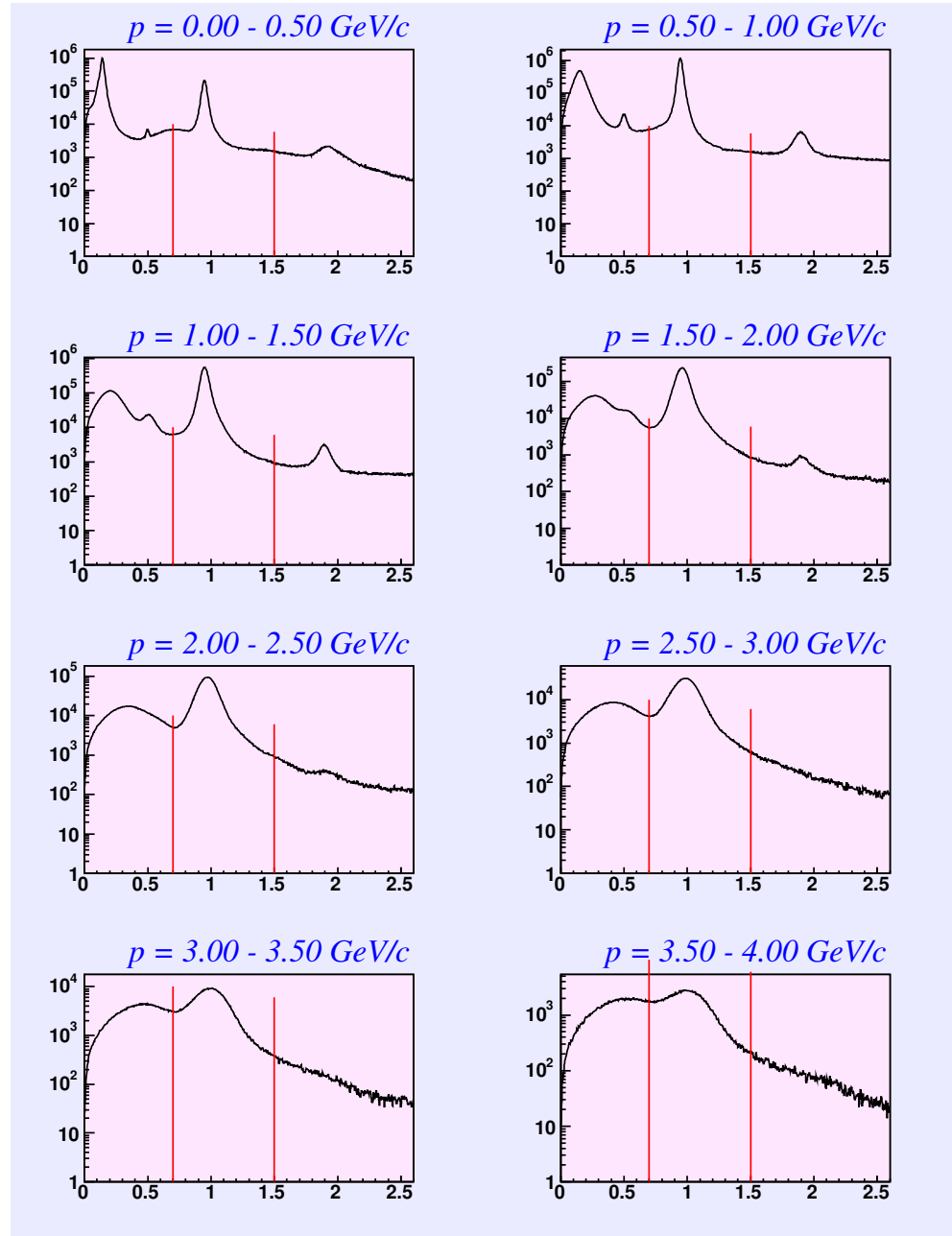


Figure 1.7: TOF mass spectra for CLAS for different momentum bins. Starting from massless particles are visible: electrons (zero mass), pions, kaons, protons and finally deuterons.

1.4 Vertex correction and cut

For each track found with the reconstruction code, a vertex (x, y, z) is calculated from the intersection of that track with the midplane² of the corresponding sector. If during the experiment the beam was not centered at $(0, 0)$ an offset is introduced in the vertex calculation.

During the e1-6 running period the beam was not centered at $(0, 0)$ and an offset was introduced in the vertex calculation as one can see in Figure 1.8, where the events on the window³ downstream of the target were selected to fix the z position as reference.

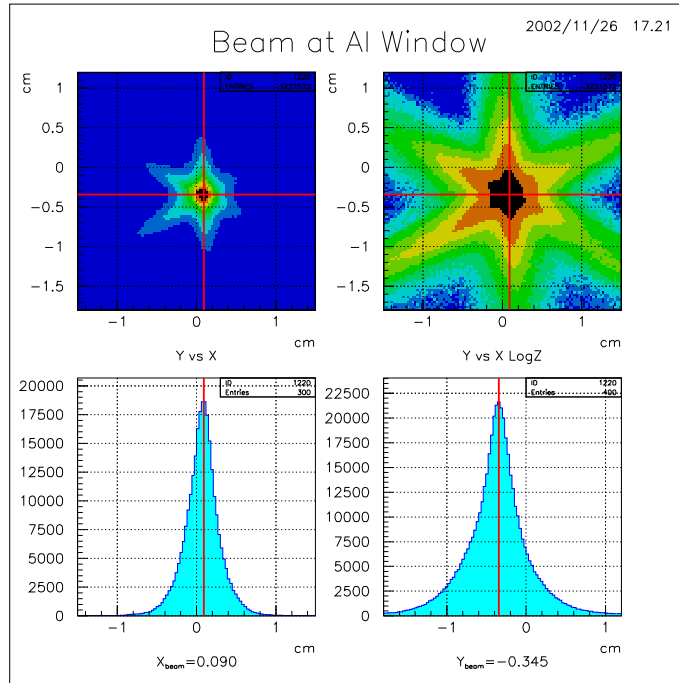


Figure 1.8: Top: y versus x position of the vertex at the window. Upper right: same as upper left, except plotted logarithmically. One can see that the beam spot was slightly shifted from $(0, 0)$. Bottom: the x (left) and y (right) distributions which led to the x_0 and y_0 calculation.

²The midplane of a sector is defined by the plane that divide that sector in half and contains the beamline $(0, 0, z)$.

³A window was placed at $z = +0.5$ cm to help these kind of studies and to be a z -position reference.

The obtained values [30] for the beam position are:

$$\begin{aligned}x_0 &= 0.090 \text{ cm} \\y_0 &= -0.345 \text{ cm}\end{aligned}$$

To correct the vertex position it is sufficient to shift the midplanes so that they contain the correct beamline $(0.09, -0.345, z)$ and recalculate the intersection of the tracks with the new planes. This is illustrated in Figure 1.9.

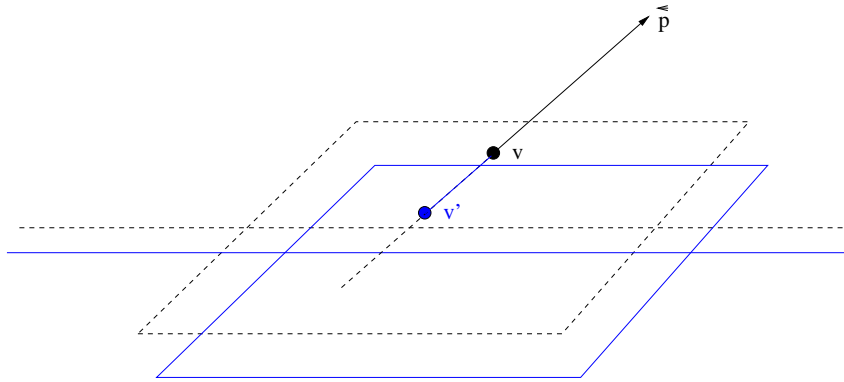


Figure 1.9: The vertex correction. The dashed plane is the original midplane containing the wrong beamline $(0, 0, 0)$. The point v is the intersection of the track (straight line along momentum \vec{p}) with this plane. The solid blue plane represents the corrected midplane containing $(0.09, -0.345, z)$. The correction algorithm simply intersects the same track with the corrected midplane.

The effect of the correction on the electron z position sector by sector is shown in Figure 1.10.

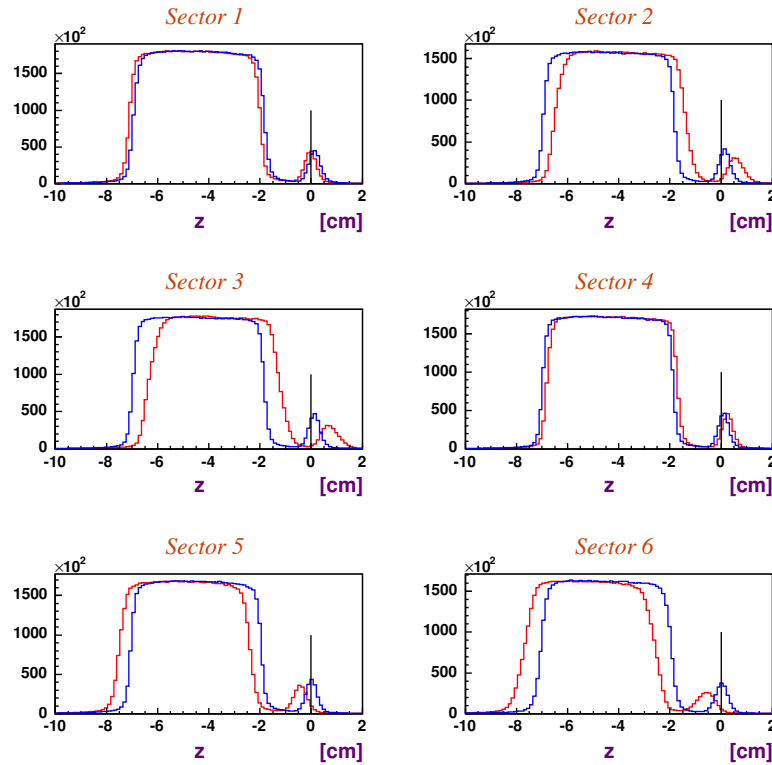


Figure 1.10: The vertex correction effect on electron z distributions for each sector. Blue: before correction. Red: after correction. The corrected distributions are aligned with each other and the resolution is improved as one can see looking at the window events. Similar effects on the other particles are observed.

The vertex resolution at this point is good enough to introduce a cut on the z vertex of electron and protons in order to select events inside the target cell as follows:

$$-8 \text{ cm} \leq z \leq -0.8 \text{ cm} \quad (1.1)$$

Furthermore the electron and proton vertices are required to be coincident along the z axis within the reconstruction resolution, so an additional cut on $\Delta z = z_{\text{electron}} - z_{\text{proton}}$ ensures that the electron and proton z vertex positions lie within 1.6 cm:

$$|\Delta z| < 1.6 \text{ cm} \quad (1.2)$$

Figure 1.11 illustrates the effect of the vertex correction on Δz integrated over all sectors and both the 1.1 and 1.2 cuts.

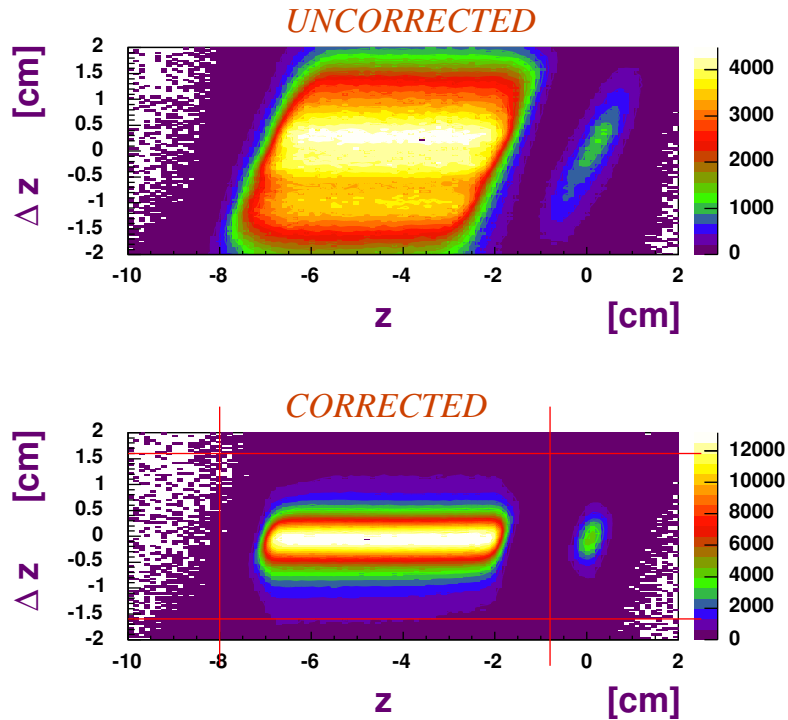


Figure 1.11: Δz versus z_{electron} uncorrected (top) and corrected (bottom) for all sectors. The distortions disappear with the correction and the resolution improves.

1.5 Electron Fiducial cuts

A fiducial cut on electrons is introduced to constrain regions of phase space where the CLAS response peaks at its maximum and remains rather smooth. The Čerenkov detector presents a drop in optical efficiency (see Figure 1.12) which is not simulated by the MonteCarlo, therefore these regions have to be removed. Drift chamber and time of

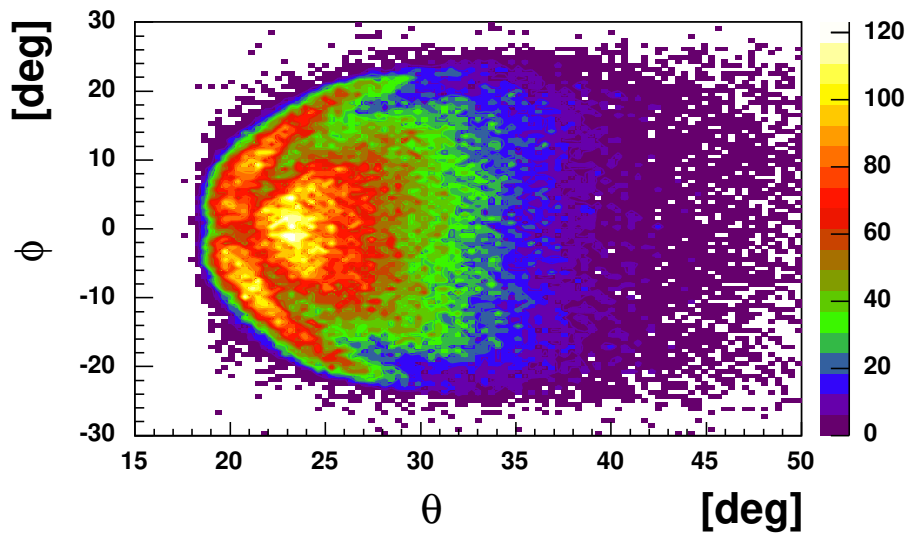


Figure 1.12: ϕ versus θ for sector 1 electrons before the electron ID. The electron ID suppress the external bands as shown in Figure 1.13.

flight inefficiencies (dead or inefficient wires, dead phototubes) cause holes and depletions in the acceptance. While most of these symptoms appears in the GSIM simulation, some do not⁴.

Furthermore the boundaries of all these regions differ when comparing actual data and simulation.

1.5.1 ϕ boundaries

For each sector, an empirical cut on ϕ is introduced as a function of theta and momentum:

$$\phi \leq \Delta\phi(\theta, p)$$

which is aimed to define regions of phase space whose distributions are flat in ϕ . After careful study [39], the mathematical form of the cut depends on 6 parameters C_i and assumes the form:

⁴One reason is that there are switched wires in the DC not accounted in the simulation.

$$\Delta\phi = C_4 (\sin(\theta - \theta_{cut}))^E$$

$$E = C_3 p^{C_5}$$

$$\theta_{cut} = C_1 + \frac{C_2}{p + C_6}$$

A ϕ vs θ distribution was plotted for 10 different momentum bins from 1.6 to 4.6 GeV. Figure 1.13 shows one example ($p = 1.9 - 2.2$ GeV) of such distributions. The ϕ distribu-

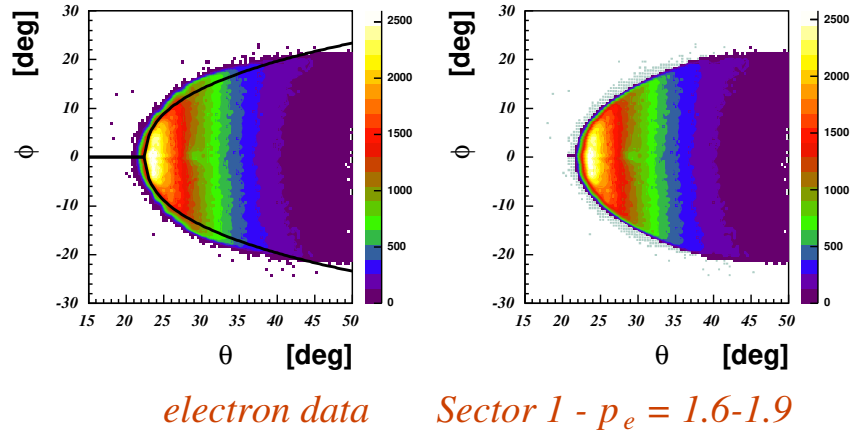


Figure 1.13: ϕ versus θ for sector 1 and $p = 1.6 - 1.9$ GeV after the electron ID. Left: before fiducial cut. Right: before fiducial cut (box/gray) and after fiducial cut (color contour). For all the bins in all the sectors, see http://www.jlab.org/~ungaro/pi0eprod/fiducial_cut_e

tions are also plotted for θ slices one degree wide as in Figure 1.14 and the C_i parameters are adjusted empirically. See

http://www.jlab.org/~ungaro/pi0eprod/fiducial_cut_e/

for all the plots.

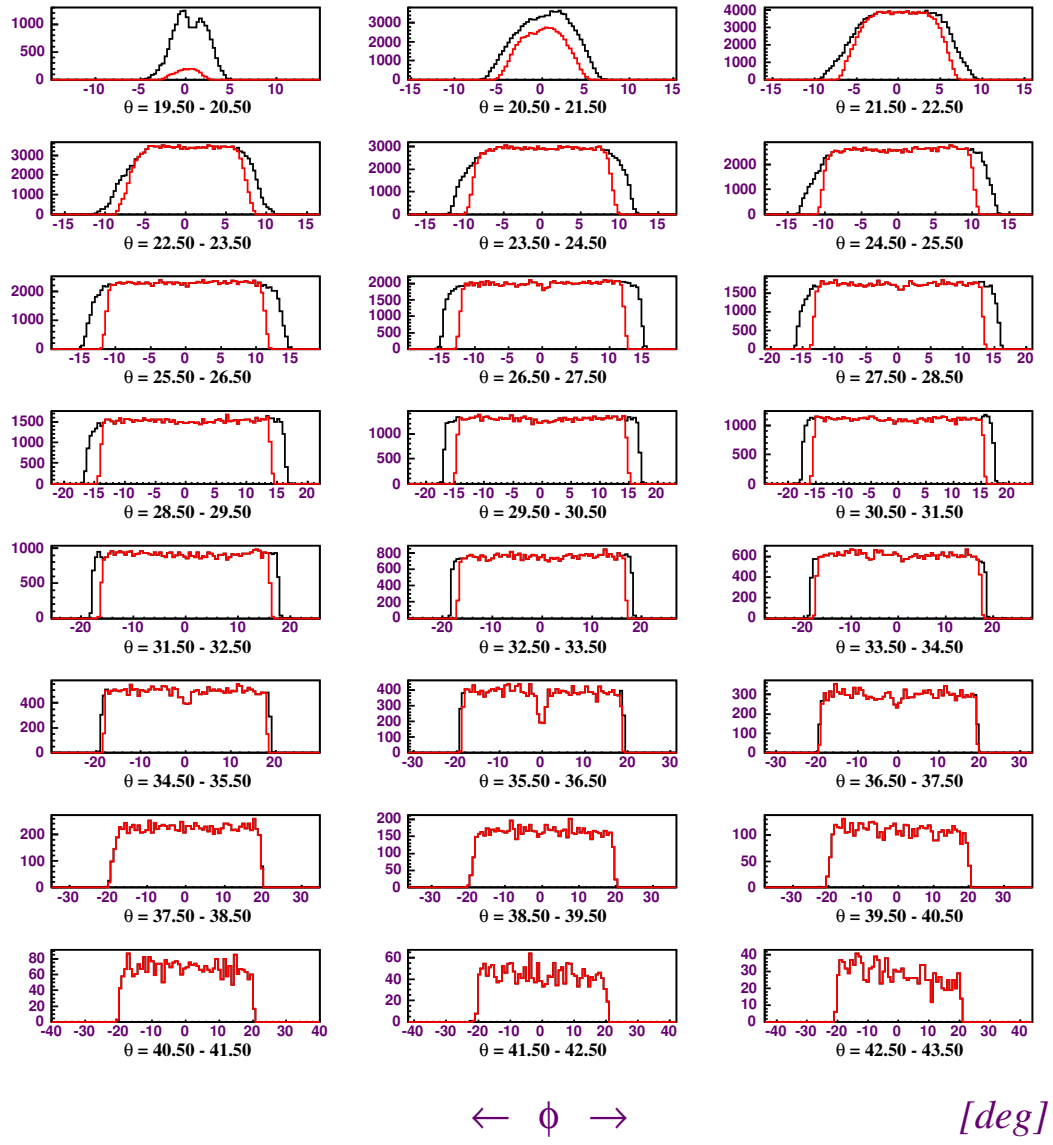


Figure 1.14: ϕ distributions (sector 3) for different θ and $p = 1.9 - 2.2$ GeV. Black: before fiducial cut. Red: after fiducial cut. Čerenkov inefficiency (section 1.9) is responsible for some irregularities at $\phi = 0$ (for example at $\theta = 35.5^0 - 36.5^0$) while drift chamber and time of flight inefficiency (section 2.2.3) causes other irregularities (for example at $\theta = 42.5^0 - 43.5^0$).

Table 1.1 shows the 6 parameters obtained. Figure 1.15 shows the fiducial cut as a function of p , θ and ϕ for sector 1.

Sector	C_1	C_2	C_3	C_4	C_5	C_6
1	12.0	20.0	0.32	32.0	0.416667	0.14
2	//	20.7	0.36	34.0	//	//
3	//	20.2	0.32	32.0	//	//
4	//	20.5	0.32	32.0	//	//
5	//	20.5	0.29	32.0	//	//
6	//	20.0	0.32	32.0	//	//

Table 1.1: The 6 parameters for electron fiducial cut for each of the 6 sectors. Only C_2 , C_3 , C_4 are sector dependent.

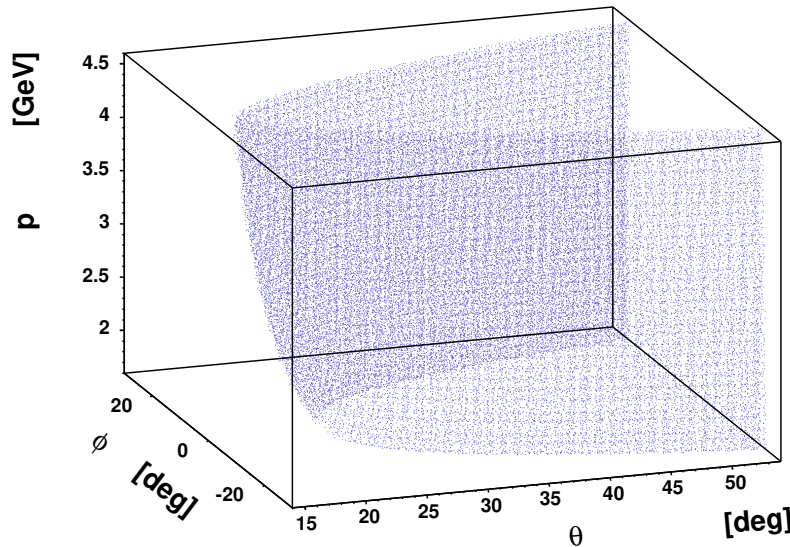


Figure 1.15: The electron fiducial cut for sector 1. The cut starting point moves back as the momentum increases (and θ decreases). This causes the cut to narrow up with momentum because electrons are detected near the lower edges of the detectors.

1.5.2 θ versus momentum cuts

Sector 2, 5 and 6 present holes and depletions (mainly because of dead time of flight paddles) which are taken care of with the cuts shown in Figure 1.16 where θ is plotted versus p .

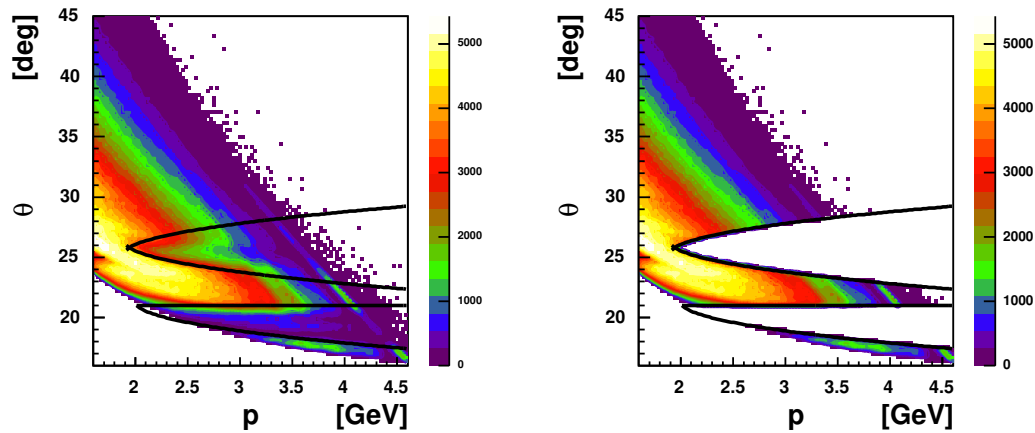


Figure 1.16: θ versus p for sector 5. Two depletions are clearly visible and cut out.

A summary of all the cuts used for the electron fiducial cut can be found in Appendix B.2.1. Figure 1.17 shows the effects of the fiducial cuts on the ϕ versus θ distribution in sector 6.

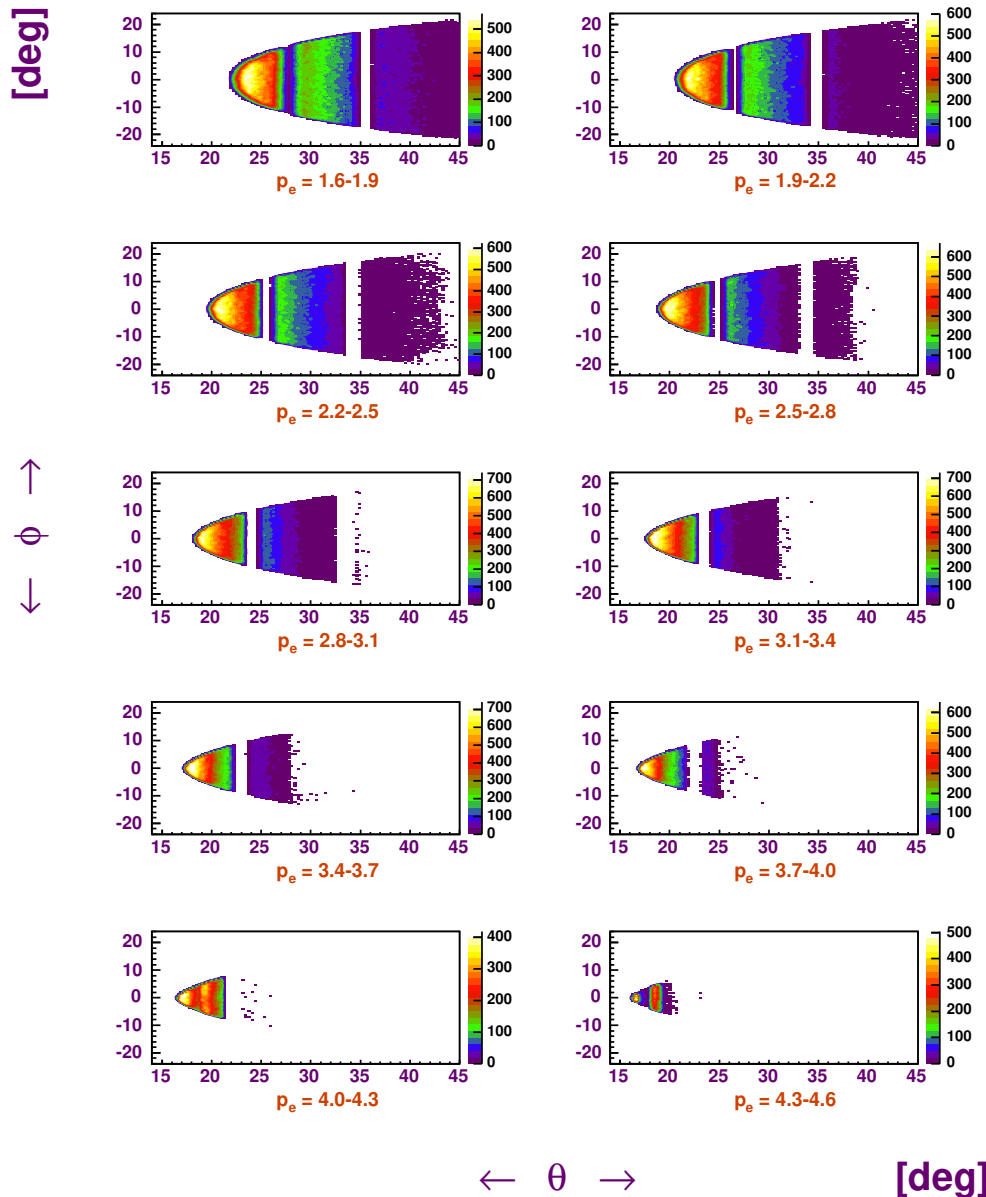


Figure 1.17: ϕ versus θ distribution for sector 6 after fiducial cuts. The θ versus p cuts are reflected on this plane as vertical bands.

1.6 Proton Fiducial cuts

Protons as well as electrons present low efficiency regions. Their detection and reconstruction close to boundaries or dead channels is not well understood.

The holes and depletions are treated with the same way as it was done for the electrons. The depletions, presented as curved bands in ϕ versus θ plots, are shown below (Figure 1.18 and Figure 1.21). The reason the bands are curved is that these are related to TOF or DC wires which are straight, thus not covering regions of $\phi = const$ space.

Unlike the electron case, the ϕ boundaries are asymmetric, as shown in Figure 1.18.

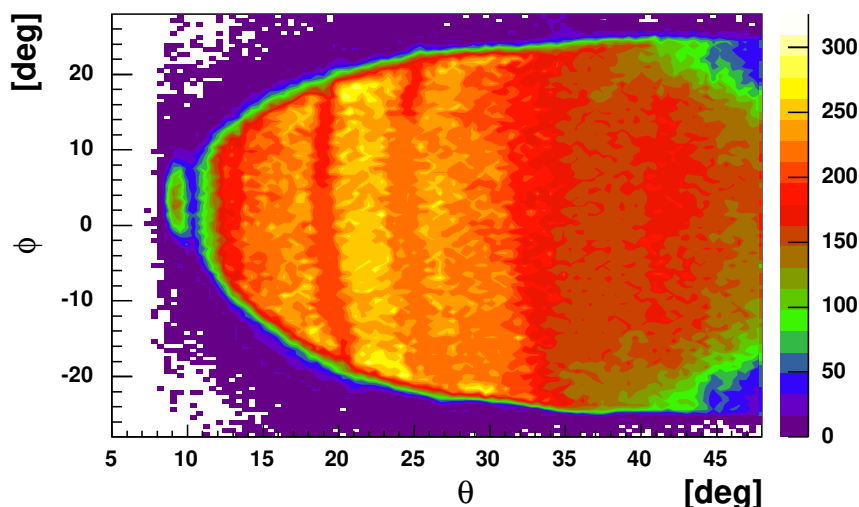


Figure 1.18: ϕ versus θ for sector 5. The momentum ranges from 0.9 to 1.6 GeV. The distribution is ϕ -asymmetric. Depletions along ϕ similar to the electron case are visible.

1.6.1 ϕ boundaries

In order to evaluate ϕ boundaries the momentum has been divided into five bins equally spaced from 0.9 to 4.4 GeV. The momentum dependance of the fiducial cut is not as strong as it was for the electrons, so a fewer number of bins are necessary.

For each momentum bin the ϕ distributions were divided in θ intervals of 1 degree and fitted with a trapezoid function [38]. The fit gives as output the ϕ lower and upper limits in which the ϕ distribution is flat (see Figure 1.20). These limits will determine the fiducial cut.

The trapezoid function is shown in Figure 1.19 and assumes the form

$$y = \begin{cases} 0 & if \quad x \leq p_1 - p_0 \\ p_4(x - p_1 + p_0)/p_0 & if \quad p_1 - p_0 < x \leq p_1 \\ p_4 & if \quad p_1 < x \leq p_2 \\ p_4(-x + p_2 + p_3)/p_3 & if \quad p_2 < x \leq p_2 + p_3 \\ 0 & if \quad p_2 + p_3 < x \end{cases}$$

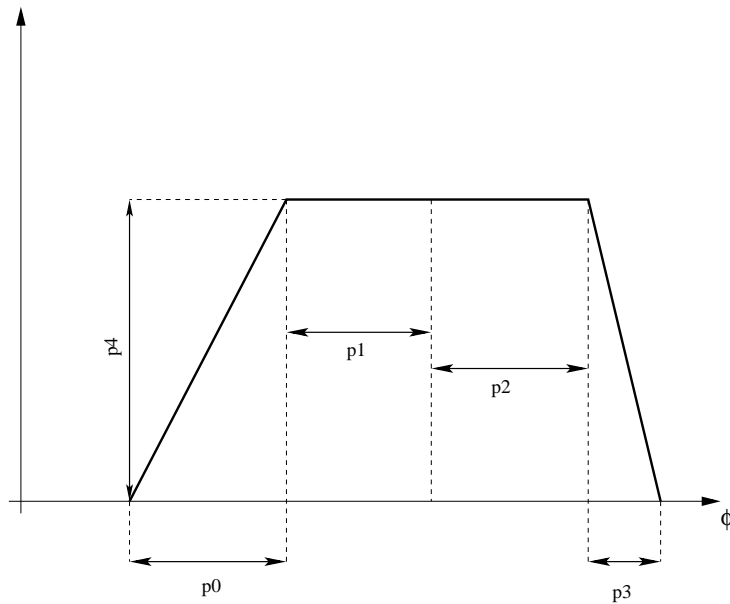


Figure 1.19: The trapezoid function used for the ϕ fit. The parameters p_1 and p_2 determine the fiducial cut lower and upper limits.

The trapezoid fit gives the parameters p_1 and p_2 described above for each θ considered in each momentum bin. These parameters are respectively the ϕ_{MIN} and ϕ_{MAX} and form a $\phi(\theta)$ distribution.

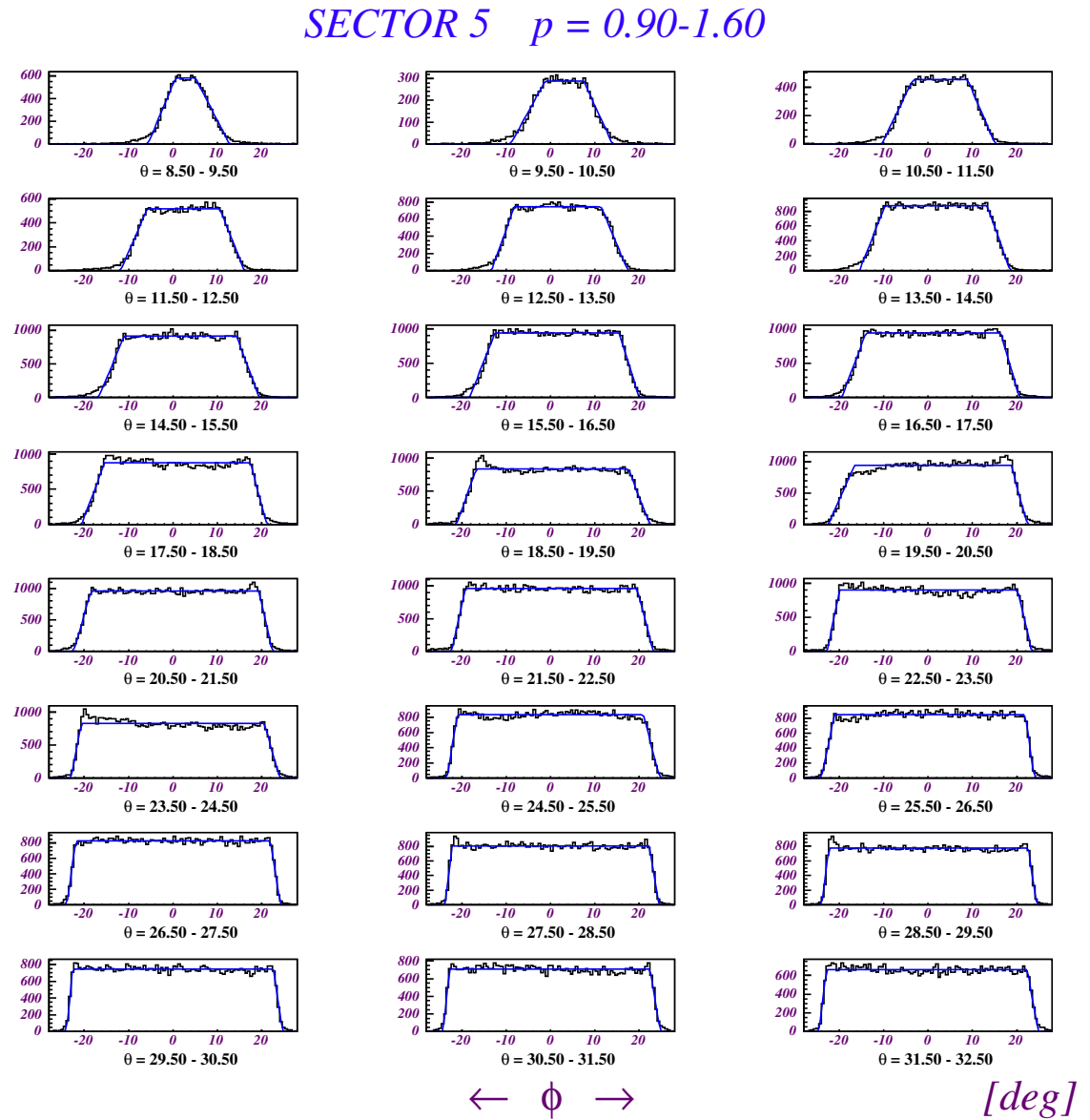


Figure 1.20: Trapezoid fit for sector 5. The limits of the flat ϕ region of each fit will determine the fiducial cut.

The parameters are fitted as a function of θ with a fourth order polynomial:

$$\phi_{MIN} = a_0 + a_1\theta + a_2\theta^2 + a_3\theta^3 + a_4\theta^4$$

$$\phi_{MAX} = b_0 + b_1\theta + b_2\theta^2 + b_3\theta^3 + b_4\theta^4$$

Figure 1.21 shows the calculated ϕ_{MIN} and ϕ_{MAX} and the resulting fit for sector 5 and momentum range 0.9 to 1.6 GeV.

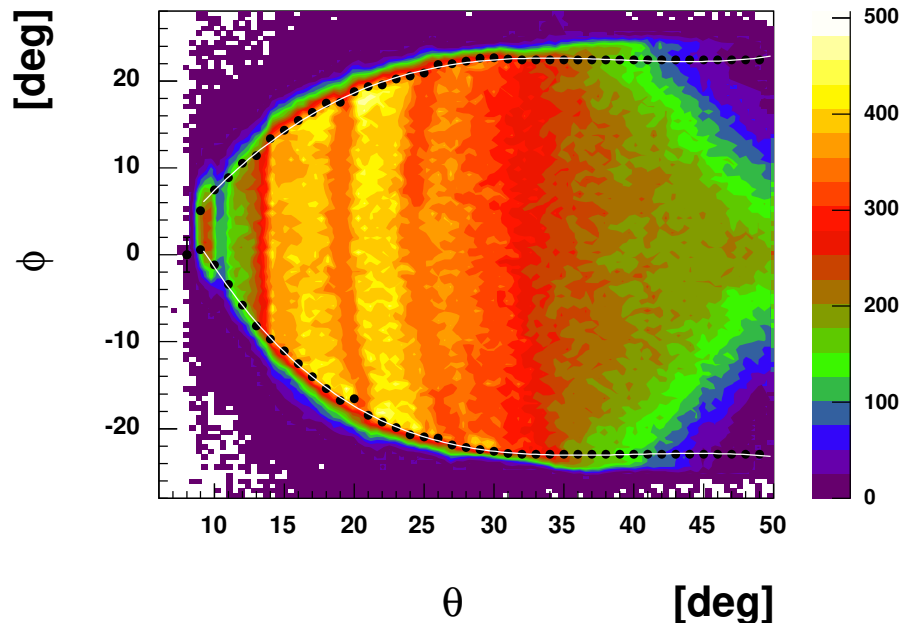


Figure 1.21: Result of the trapezoid fit for sector 5. The proton momentum ranges from 0.9 to 1.6 GeV. The black points are the parameters p_1 (negative ϕ) and p_2 (positive ϕ) for each θ slice considered as shown in Figure 1.20. The white line is a fourth order polynomial fit to the black points.

The parameters a_i , b_i are momentum dependent, since a fit is made for each momentum bin.

$$\begin{aligned} a_i &= a_i(p) \\ b_i &= b_i(p) \end{aligned} \quad i = 0..5$$

In order to exploit the momentum dependance each of these parameters is fitted as a function of p with a second order polynomial as shown in Figure 1.22.

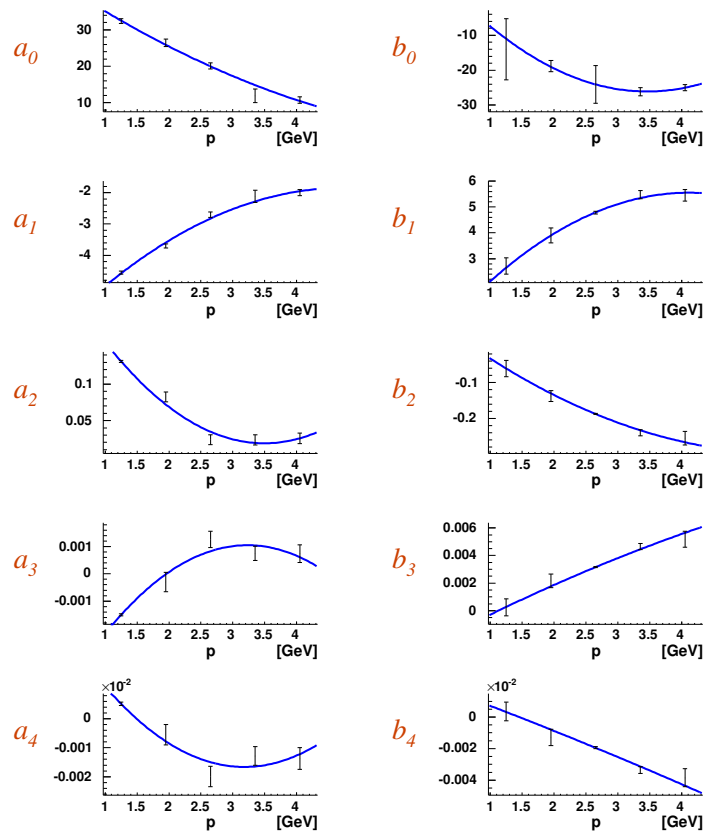


Figure 1.22: Sector 5 parameters fit. Each of the parameters is fitted as a function of the proton momentum with a second order polynomial.

The overall fiducial (shown for sector 5 in Figure 1.23) cut is finally determined, in each sector, by the limits:

$$\phi_{MIN} = \sum_{i=0}^5 a_i(p) \theta^i$$

$$\phi_{MAX} = \sum_{i=0}^5 b_i(p) \theta^i$$

$$\phi_{MIN} \leq \phi \leq \phi_{MAX}$$

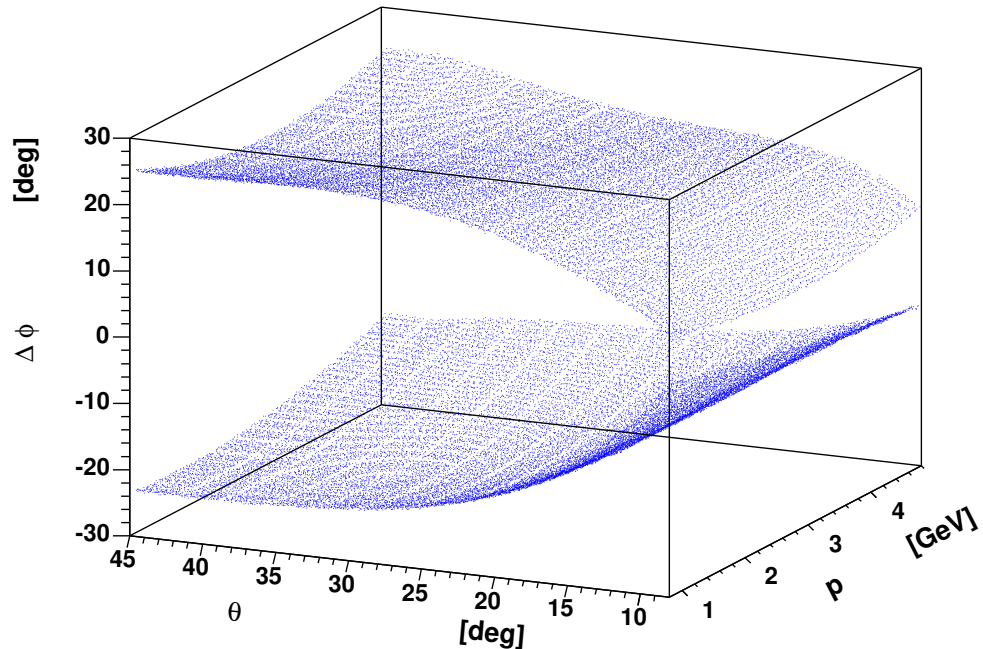


Figure 1.23: Sector 5 $\Delta\phi$ fiducial cut as a function of θ and ϕ .

1.6.2 θ versus momentum cuts

Sector 2, 3, 5 and 6 present holes and depletions which are taken care of with the cuts shown on Figure 1.24 where θ is plotted against the momentum p .

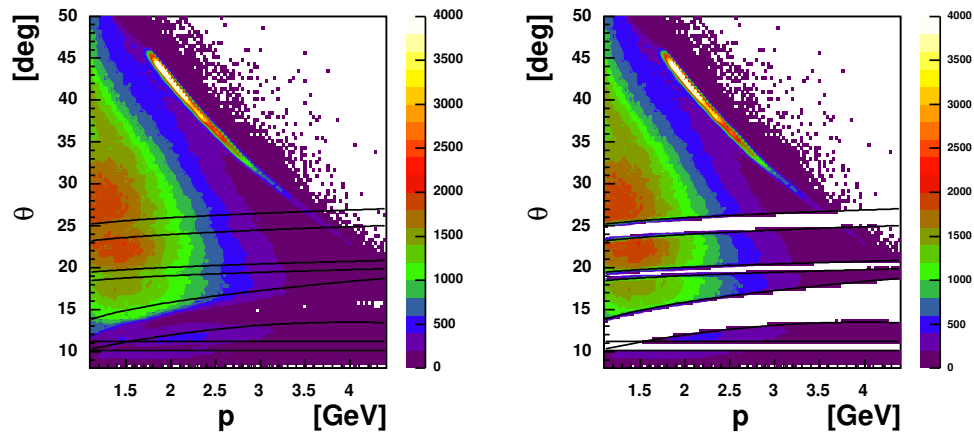


Figure 1.24: θ versus p for protons sector 5. A depletion is clearly visible and cut out.

A summary of all parameters can be found in Appendix B.2.3.

The effect of the fiducial cut on sector 5 is shown in Figure 1.25.

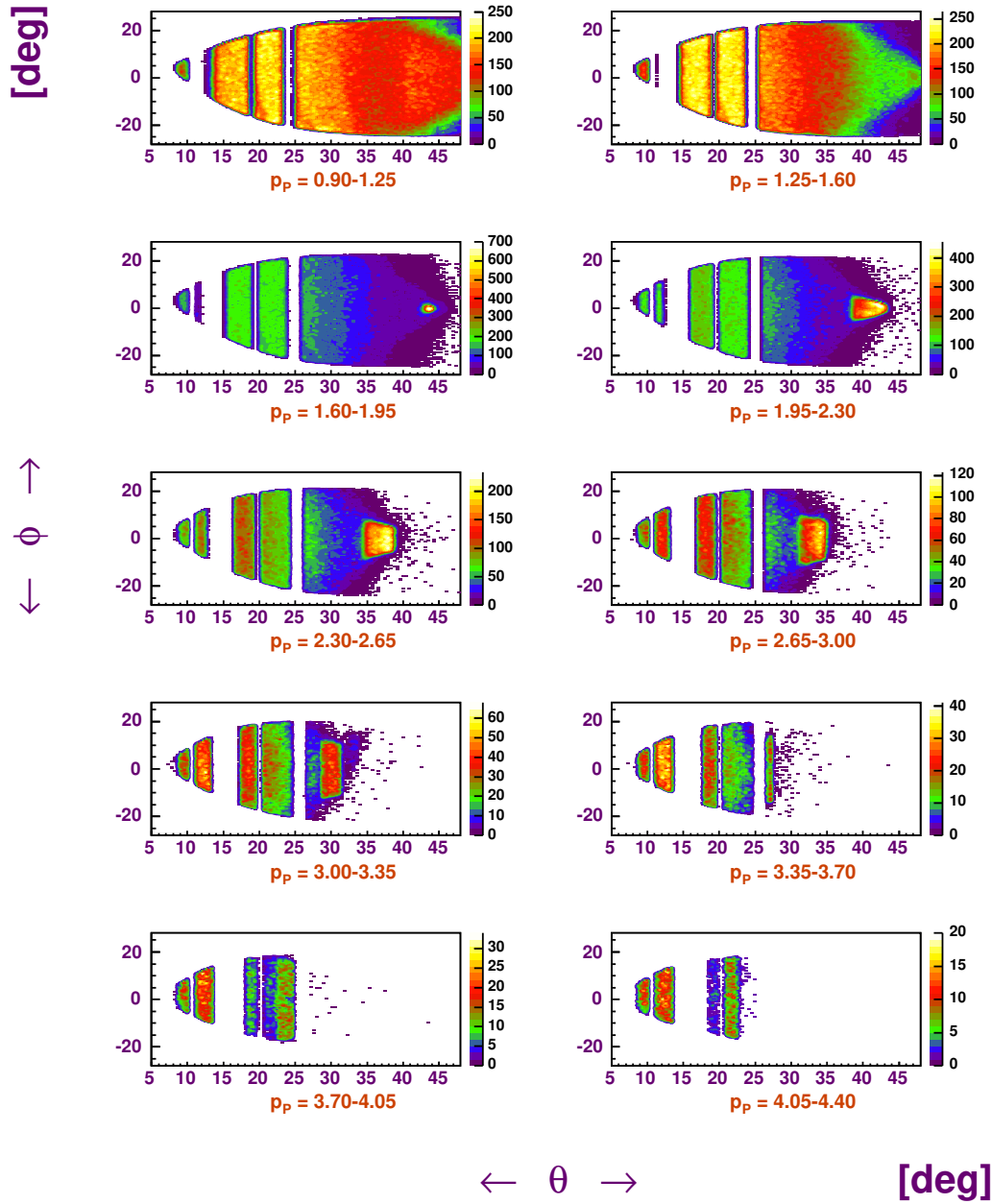


Figure 1.25: Sector 5 ϕ versus θ after fiducial cut. The empty bands in this sector are unfortunate because the forward ones occur where many protons of interest to us are expected. Compare with Figure 1.18 or Figure 1.21 to appreciate the cutoff of the depletions.

1.7 Kinematic corrections

The kinematic corrections presented here are based on the elastic kinematics and the incident electron beam energy value. Both these matters are important, and therefore discussed below.

After selecting elastic events, systematic deviations are found on electron and proton angles and on electron momentum. No significant error is found on proton momemtum.

1.7.1 Beam Energy measurement

The beam energy value chosen for this analysis is the result of measurements from Hall A, which has two means of computing the beam energy:

- **e, P method:** it is based on the angle measurement in the two bodies $^1H(e, e'P)$ kinematics.
- **“arc” method:** it is based on the use of a section of the beam transport line as a magnetic spectrometer.

Both these method are used during Hall-A experiments.

During e1-6 data acquisition time such a measurement was taken on 2/11/2002 (during this experiment) and it gave as results:

$$\begin{array}{ll} e, P & 5754.41 \pm 1.76 \text{ GeV} \\ ARC & 5754.4 \pm 1 \text{ GeV} \end{array}$$

Based on the above, the beam energy value chosen for this analysis is:

$$E = 5.7544 \text{ GeV}$$

1.7.2 Elastic selection

The $eP \rightarrow e' P'$ elastic reaction is useful for many purposes. The constraint allows one to determine systematic errors and corrections, on one or more variables. The hadronic mass of the $P\pi^0$ system is close to M_P , so one can assume that those corrections hold for the $\Delta(1232)$ kinematics as well as they do for the elastic kinematics.

The Bethe Heitler (B.H.) process $eP \rightarrow eP\gamma$ discussed in 1.8 is included in elastic eP events, and cuts are determined to select only low energy (soft) photons.

I present here a series of cuts for e1-6 data to achieve exclusive elastic selection after electron and proton particle ID.

W cut

The first cut, illustrated in Figure 1.27 a), is on W , the outgoing hadron mass, which for elastic scattering is the mass of the proton. A gaussian is fitted to the W distribution for each sector and 3σ around the mean determine the W cut.

$M_x(eP)$ cut

The second cut is on the missing mass of the outgoing eP system. See Figure 1.27 b). No particles except B.H. photons are produced during elastic scattering, therefore the missing mass must be zero. A gaussian is fitted to the $M_x(P)$ distribution for each sector and 3σ around the mean represents the $M_x(EP)$ cut.

$\Delta\theta$ cut

The elastic constraint allows us to determine the proton angle in the lab θ_{calc}^P using only the outgoing electron angle and energy. Assuming that the scattered electron doesn't change direction when it emits a photon (peaking approximation), this calculation is independent of the outgoing electron energy and therefore it is independent of post-radiative effects shown on Figure 1.26 b).

The third cut is on $\Delta\theta = \theta_{meas}^P - \theta_{calc}^P$ (Figure 1.27 c) where

$$\tan \theta_{calc}^P = \frac{1}{\left(1 + \frac{E}{M_P}\right) \tan \frac{\theta_{e'}^P}{2}}$$

A gaussian is fitted to the $\Delta\theta$ distribution for each sector and 2σ around the mean represents the $\Delta\theta$ cut.

$\Delta\theta_2$ cut

The elastic constraint allow us to determine the proton angle in the lab θ_{calc2}^P using only the incident electron energy and the outgoing electron angle. This calculation is independent of the incident electron energy and therefore it is independent of pre-radiative effects shown on the Figure 1.26 a).

The fourth cut is on $\Delta\theta_2 = \theta_{meas}^P - \theta_{calc2}^P$ (Figure 1.27 d) where

$$\tan \theta_{calc2}^P = \frac{1}{\left(1 + \frac{E'}{M_P - E' + E' \cos \theta_{e'}^P}\right) \tan \frac{\theta_{e'}^P}{2}}$$

A gaussian is fitted to the $\Delta\theta_2$ distribution for each sector and 2σ around the mean represents the $\Delta\theta_2$ cut.

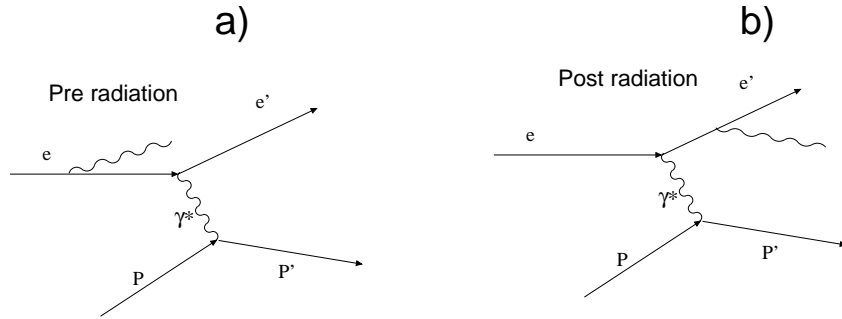


Figure 1.26: Radiative elastic events. a) pre-radiation. A photon is emitted by the incoming electron. b) post-radiation. A photon is emitted by the outgoing electron.

$\Delta\phi$ cut

The fifth and final cut is on the difference between the electron and proton azimuthal angle $\Delta\phi$ (Figure 1.27 e). Both electrons and protons, in the peaking approximation and for elastic events, lie in the same plane therefore $\Delta\phi$ must be equal to π .

A gaussian is fitted to the $\Delta\phi$ distribution for each sector and two σ s around the mean represents the $\Delta\phi$ cut.

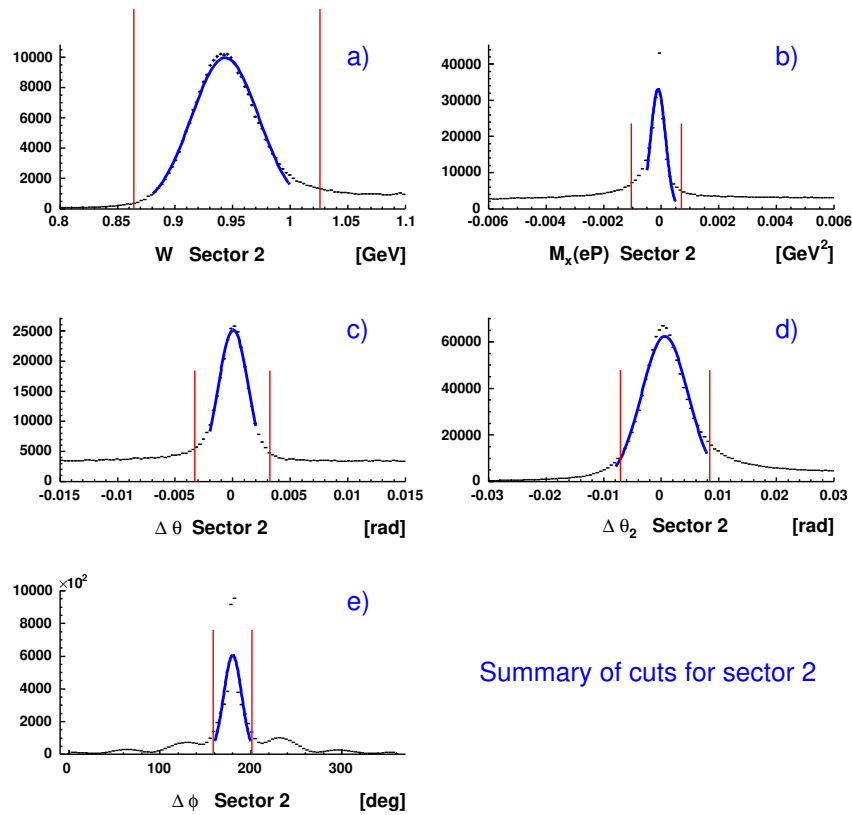


Figure 1.27: The cuts for elastic selection for sector 2. (a) W mass cut. (b) Missing (eP) mass cut. (c) $\Delta\theta$ cut. (d) $\Delta\theta_2$ cut. (e) Coplanarity cut.

1.7.3 Angle corrections

The θ angles of electrons and protons present a distorted ϕ dependence due mainly to misalignments of the drift chambers. This error can be easily seen by looking at elastic events. In particular one can calculate the predicted beam energy E_{calc} using the angles of electron and proton with the formula

$$E_{calc} = M_P - \frac{M_P}{\tan(\theta_e/2) \tan\theta_P} \quad (1.3)$$

and look at the difference between E_{calc} and the nominal beam energy $\Delta E = E_{nom} - E_{calc}$ as a function of ϕ (see Figure 1.28).

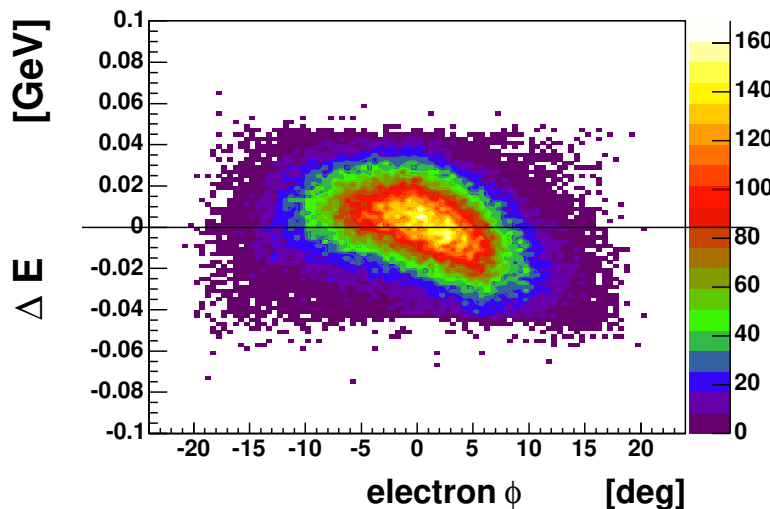


Figure 1.28: ΔE as a function of ϕ for electrons in sector3. One can see distortions as big as 30 MeV.

It turns out that the distortion is small, averaged around 0.4 mrad (0.02 degrees) and peaking at 1 mrad (0.06 degrees). However the momentum correction is based on the angle measurement. Furthermore, the boost in the $\Delta^+(1232)$ c.m. system amplifies small deviations, so the angles measurement have to be as precise as possible.

One can use (1.3) to calculate a correction. For example, one can assume that the electron angle reconstruction is correct and calculate a correction for the proton. Or vice versa.

In the present work, it was assumed that the angle distortion comes from a DC misalignment, and therefore gives similar effect on all particles. Under this assumption, all particles have (the same) systematic error on their angle measurement,

In order to calculate the correction, the theoretical correlation (1.3) between the lab angles of the electron and proton is used. Such correlation is shown in Figure 1.29.

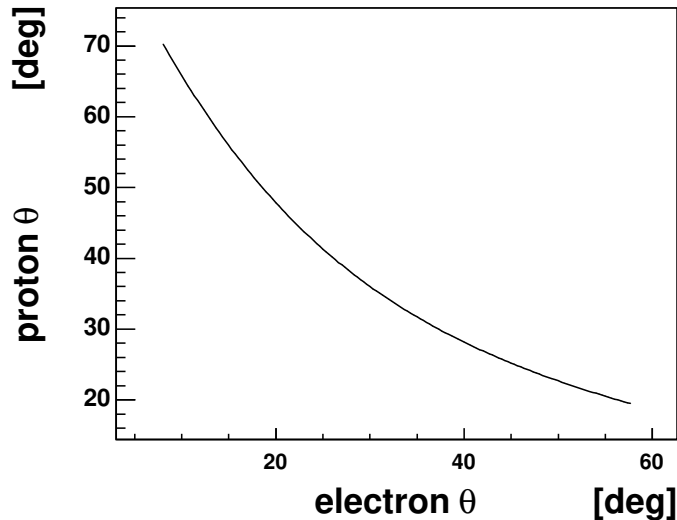


Figure 1.29: The constraint of elastic scattering: proton θ versus electron θ for elastic scattering for a 5.754 GeV beam energy.

During the experiment, the measured angle P deviates from this curve as indicated in Figure 1.30 which is a zoom of Figure 1.29. To calculate the corrections $\Delta\theta_e$ and $\Delta\theta_p$ the point **C** of the curve closest to **P** is found with an algorithm that minimizes the radius of a circle with center in **P** intersecting the curve.

The corrections $\Delta\theta_e$ and $\Delta\theta_p$ for the electrons and protons found with this algorithm are combined together and plotted for different θ slices in Figure 1.31. Notice that, since the correction is the same for all particles, at this point electron and proton lose their identities and “ θ ” is θ_e or θ_p .

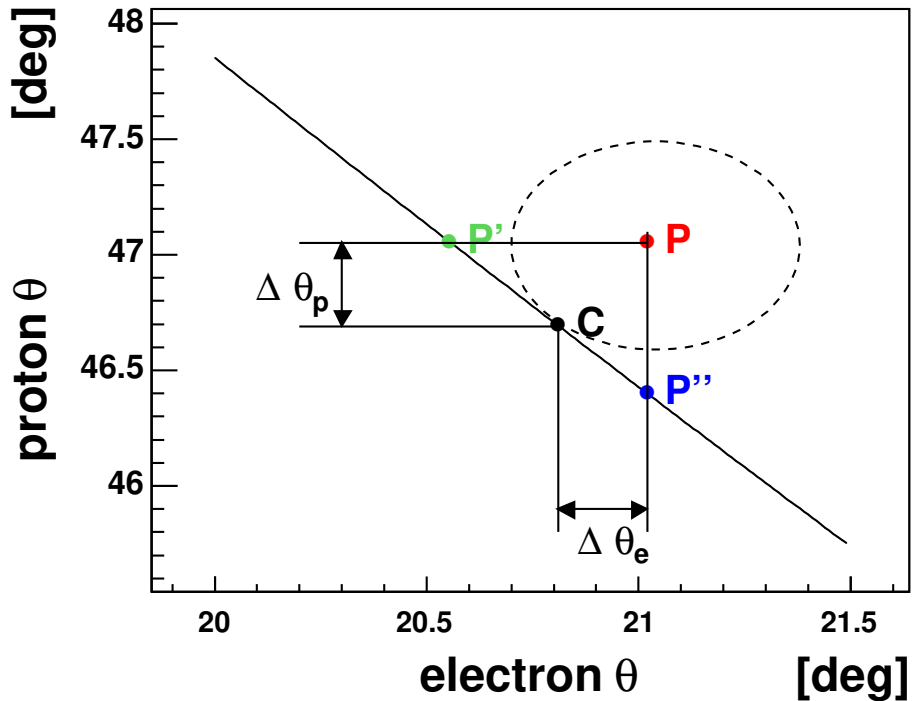


Figure 1.30: The angle correction algorithm. A measured angle of electron and protons (red point P) does not lie in the theoretical curve. The circle with center at P intersecting the curve and with minimum radius is found. Its intersection with the curve is the point C , the point of the curve closest to P . Notice that the x and y scales are different so that the circle looks like an ellipse.

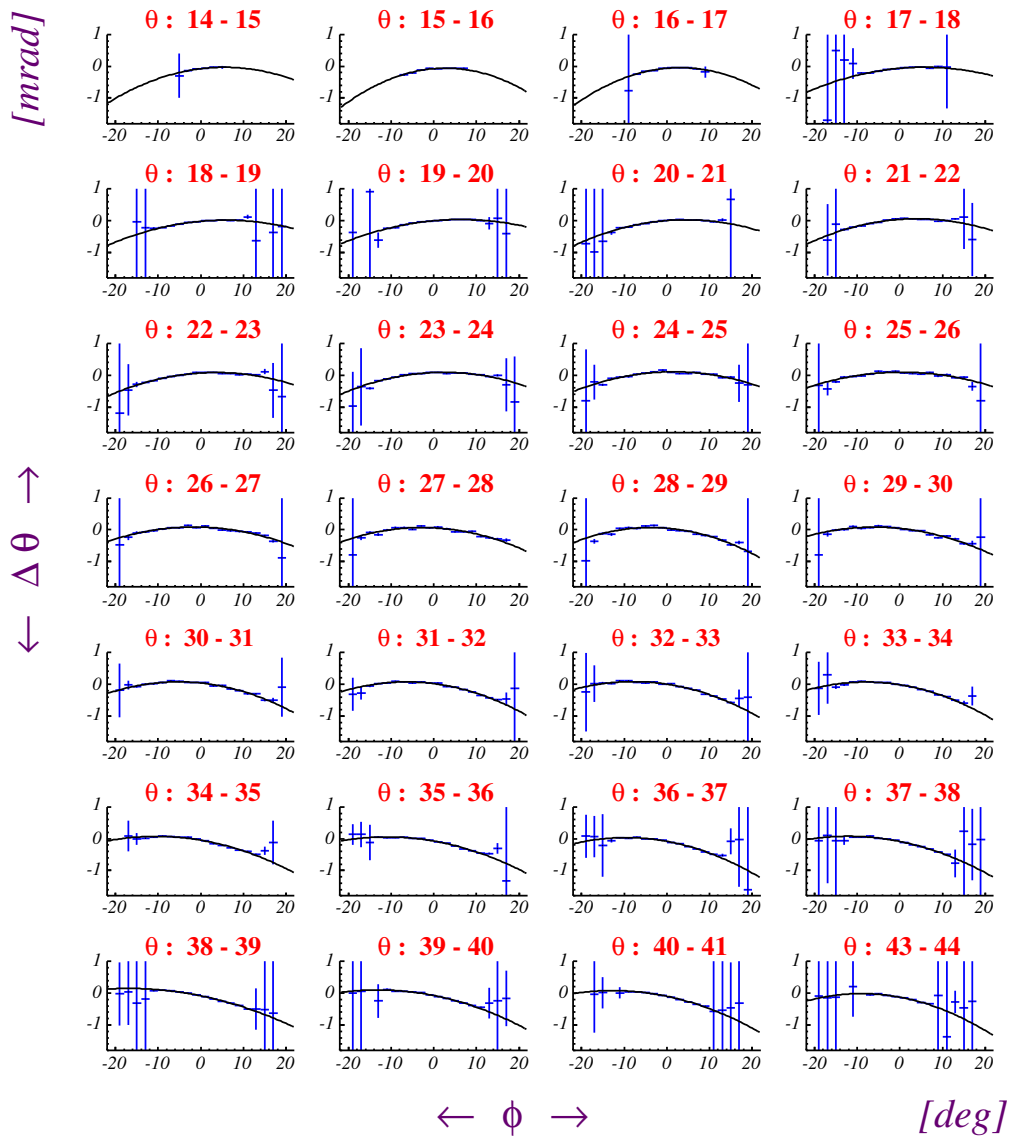


Figure 1.31: The combined angle correction $\Delta\theta$ for electron and proton for different θ slices.
Each slice is fitted with a second order polynomial (black curve).

The correction is fitted with a second order polynomial, yielding three parameters for each θ slice considered:

$$a = a(\theta), \ b = b(\theta), \ c = c(\theta)$$

Each of the three parameters is then plotted as a function of θ in Figure 1.32.

When calculating the parameters for a given θ an interpolation is used, shown in the figure in red.

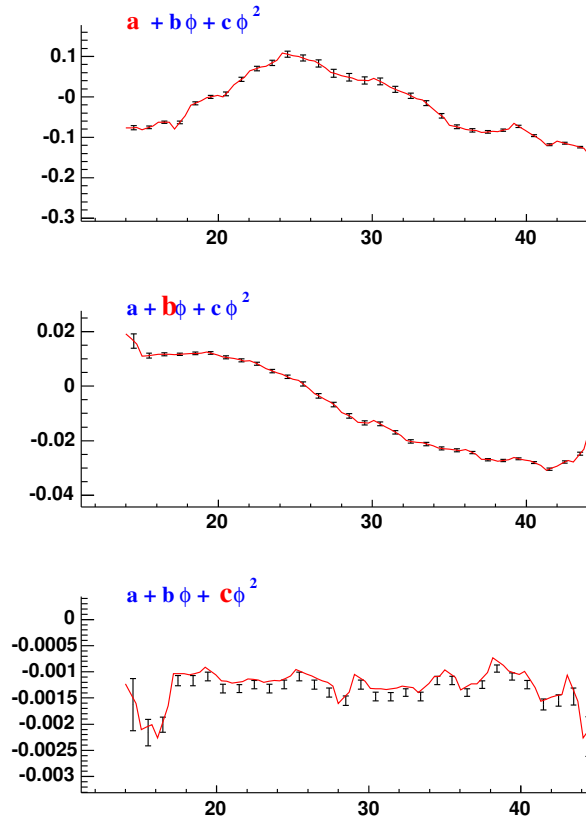


Figure 1.32: Angle correction parameters as a function of θ for sector 1. The red line is the linear interpolation of the points.

The overall angles correction $\Delta\theta$ is

$$\Delta\theta = a(\theta) + b(\theta) \phi + c(\theta) \phi^2$$

To check to quality of the correction the ΔE distribution (like the one in Figure 1.28) is plotted against ϕ before and after the correction for each sector. Figure 1.33 show the mean of the ΔE distribution.

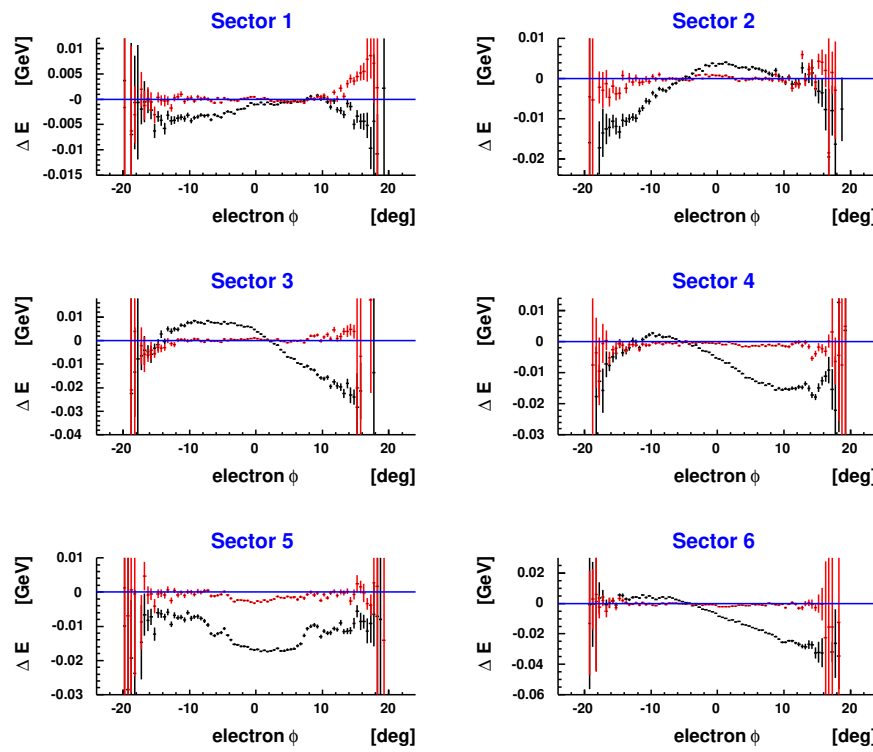


Figure 1.33: ΔE as a function of ϕ for each sector. Black: before correction. Red: after correction.

1.7.4 Momentum corrections

Drift chamber misalignment and an inaccurate magnetic field map are the main reasons why the reconstruction of the momentum is slightly incorrect. This is reflected on quantities like W or missing mass. For example for elastic events the W distribution is distorted as seen in Figure 1.34 where it is plotted against the electron azimuthal angle in the laboratory system after angle corrections.

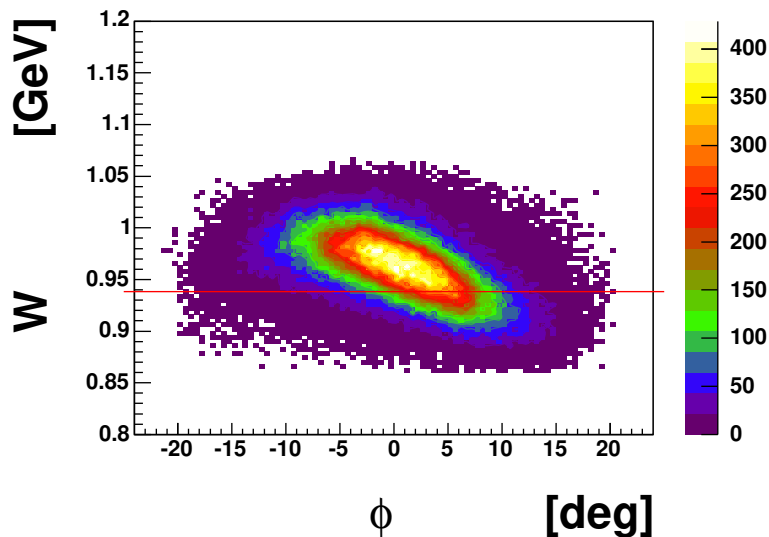


Figure 1.34: W distribution as a function of electron ϕ for elastic events after angle corrections. The red line is the mass of the proton.

The distortion turns out to depend upon ϕ and θ of the electron (and not on its momentum). Recall that for elastic events the θ and the momentum p are highly correlated⁵. Such distortion is sector dependant and needs to be corrected.

The empirical correction discussed below is based upon the elastic kinematics. The mass of the $\Delta(1232)$ is close enough to the one of the proton to fairly justify applying the correction for pion electroproduction in the Δ region because the phase spaces do not differ a lot.

The quantity

$$\Delta p = p_{meas} - p_{calc} = p_{meas} - \frac{E}{(1 + E(1 - \cos \theta)/M_P)}$$

where E is the beam energy, is extracted and plotted versus ϕ for different θ slices in

⁵This is not true for other reactions, where the distortion is also momentum dependent.

Figure 1.36 for sector 3. Δp is the wanted correction. Notice that Δp depends only upon the scattered electron angle.

Each Δp distribution is fitted with a third order polynomial, giving the parameters as a function of θ :

$$a = a(\theta), \ b = b(\theta), \ c = c(\theta), \ d = d(\theta) \quad (1.4)$$

Each parameter is then fitted with a 10th order polynomial to exploit the θ dependance. The fits for sector 3 are shown in Figure 1.35.

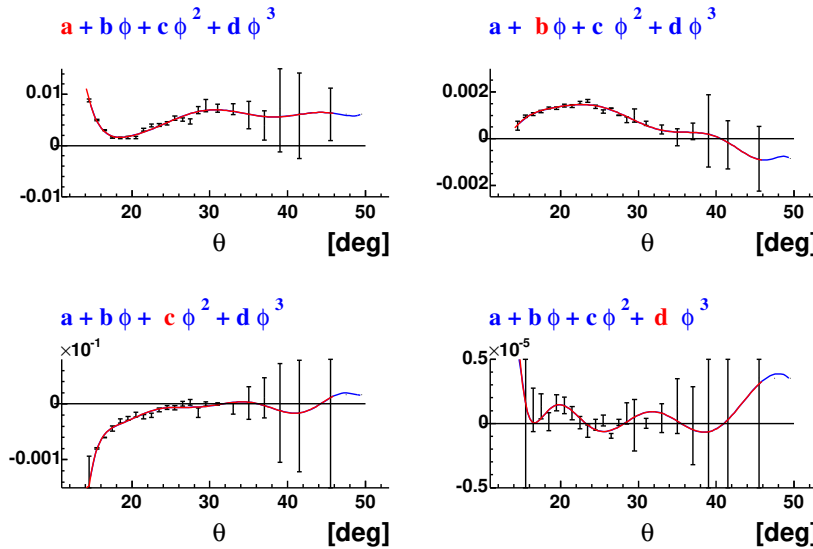


Figure 1.35: Fits of the third order polynomial parameters as a function of θ for sector 3.

The overall correction is

$$\Delta p = a(\theta) + b(\theta) \phi + c(\theta) \phi^2 + d(\theta) \phi^3$$

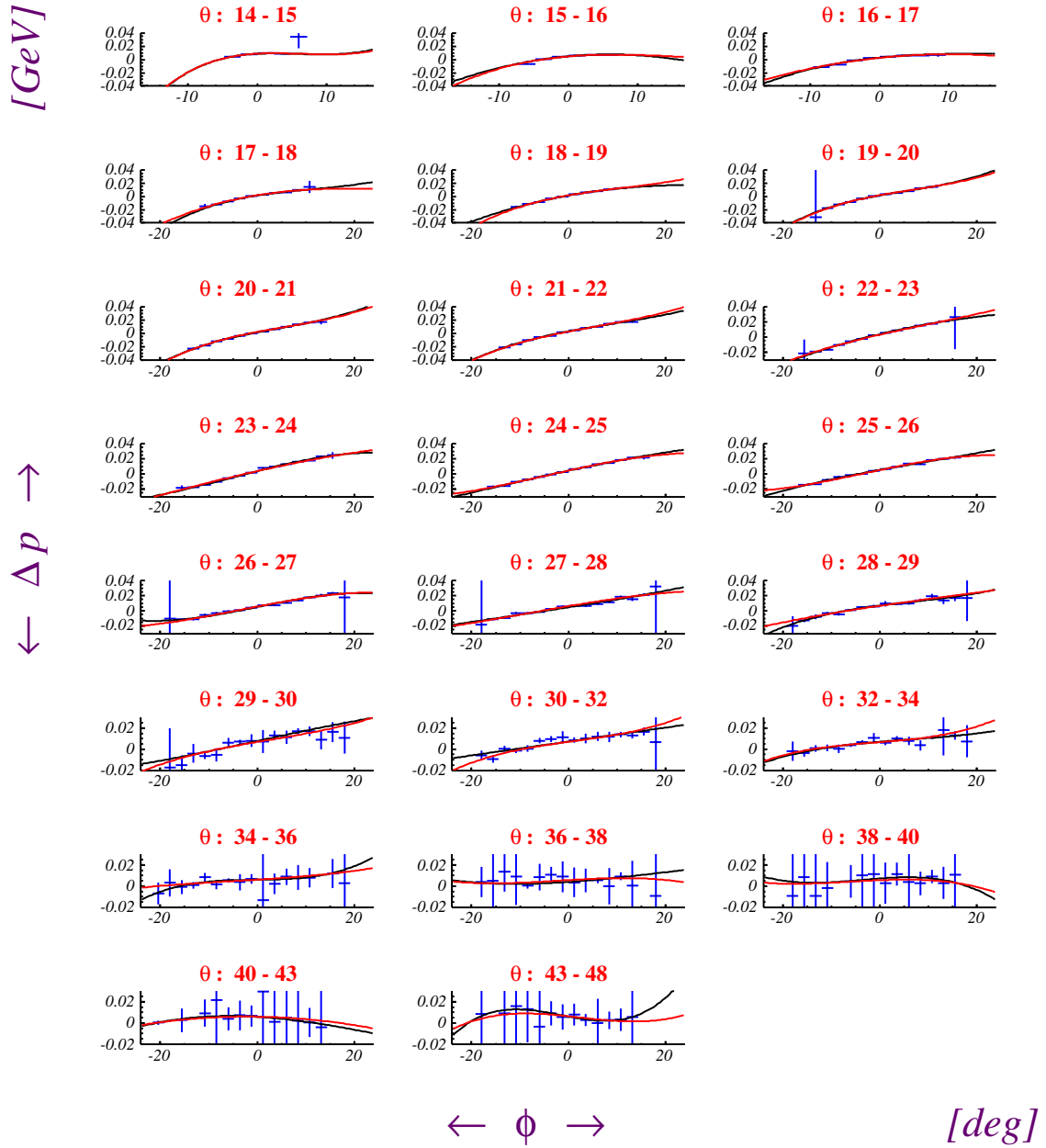


Figure 1.36: Fits of the Δp distributions for different θ slices as a function of ϕ . The black curve is the local fit to the distribution while the red one is the function coming from the global parameters 1.4. The procedures make sure that these two curves are close to each other.

The result of the correction for sector 1 is shown in Figure 1.37. One can see that the distortion disappeared and the W distribution is now centered at the mass of the proton. Similar effects are seen for all sectors.

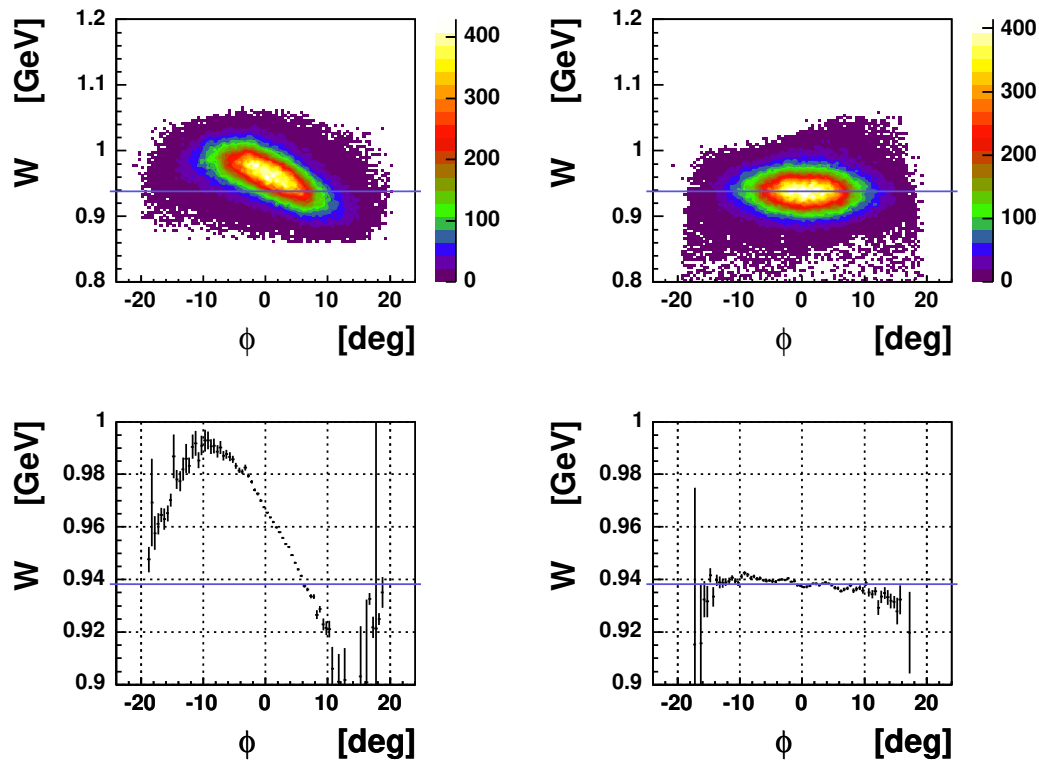


Figure 1.37: The W versus ϕ distribution for electrons in sector 1 before (left) and after (right) momentum correction. The bottom plots are the means of the top distributions sliced along W .

1.8 Bethe Heitler processes

Figure 1.38 shows the (e, P) missing mass M_X^2 versus W distribution for the whole e1-6 period after particle ID, vertex fiducial cuts and kinematic corrections. The elastic and Bethe Heitler (B.H.) events, illustrated in Figure 1.39, are clearly seen at $M_X^2 = 0$, with the characteristic increase of the cross section at high W . Also shown are the $S_{11}(1535)$ resonance decaying in η , the $P_{13}(1720)$ resonance decaying in ρ and the subject of this analysis, the $\Delta_{33}(1232)$ resonance decaying in π^0 .

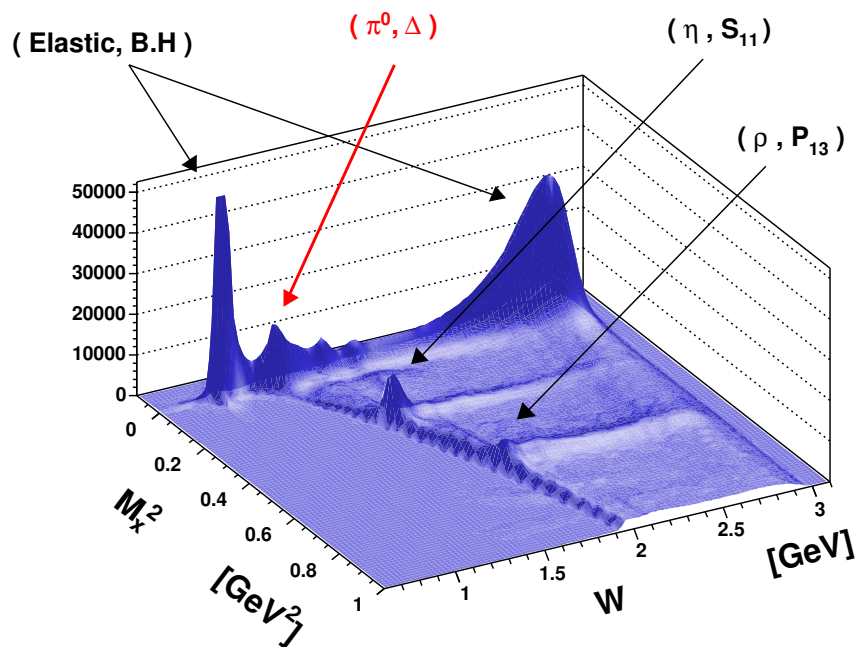


Figure 1.38: Missing mass M_X^2 versus W after particle ID, vertex fiducial cuts and kinematic corrections for the whole e1-6 data. Clearly visible are the elastic and B.H. events, the $S_{11} \rightarrow \eta$, the $P_{13} \rightarrow \rho$ and of course the $\Delta_{33} \rightarrow \pi^0$ events.

To isolate the $p(e, e'p)\pi^0$ reaction a missing mass technique alone cannot separate the B.H. processes from the π^0 events efficiently because of the limited resolution. What follows is the investigation of the kinematic cuts used to remove the B.H. events from the inelastic data.

An important assumption used to identify B.H. events is the so called *peaking approximation*. It means that the direction of the emitted photon in reaction like the ones shown in Figure 1.39 a) and b) is the same as the electron. Therefore the electron does not

change direction when radiating a photon, although it can change energy. This approximation describes well most electron B.H. events [34].

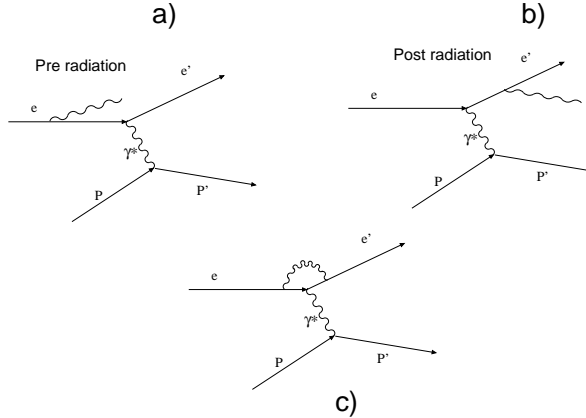


Figure 1.39: Bethe Heitler events contributing to the (eP) final state leaking into the π^0 missing mass.

The variables used for the separation are:

- M_x : missing mass squared of the final state (eP) .
- $\Delta\theta = \theta_{meas}^P - \theta_{calc}^P$: θ_{meas}^P is the measured proton angle and θ_{calc}^P is the proton angle calculated from the outgoing electron energy and angle (see Section 1.7.2). In the peaking approximation, $\Delta\theta$ is independent of **pre-radiation** processes like the ones in Figure 1.39 a) and it assumes the value zero for elastic and B.H. events.
- $\Delta\theta_2 = \theta_{meas}^P - \theta_{calc2}^P$: θ_{meas}^P is the measured proton angle and θ_{calc2}^P is the proton angle calculated from the incoming electron energy and outgoing electron angle (see Section 1.7.2). In the peaking approximation, $\Delta\theta_2$ is independent of **post-radiation** processes like the ones in Figure 1.39 b) and it assumes the value zero for elastic and B.H. events.
- $\phi_P^{c.m.}$: the azimuthal angle of the proton in the resonance center of mass, equal to π for B.H. events in the peaking approximation.

The contamination is W dependent, so eight bins in W have been considered from 1.08 to 1.48 GeV. Three cuts have been used in series as described below.

The $\phi_P^{c.m.}$ of the elastic events narrows in ϕ and broadens in M_x^2 as W increases as it is shown in Figure 1.40 where it is plotted against the missing mass M_x^2 . The first cut, represented by the black curve in Figure 1.40, is composed by:

- A circle whose radius and center vary with W .
- A hyperbole $y = \pi \pm \frac{a}{x - x_0}$ whose a and x_0 vary with W .

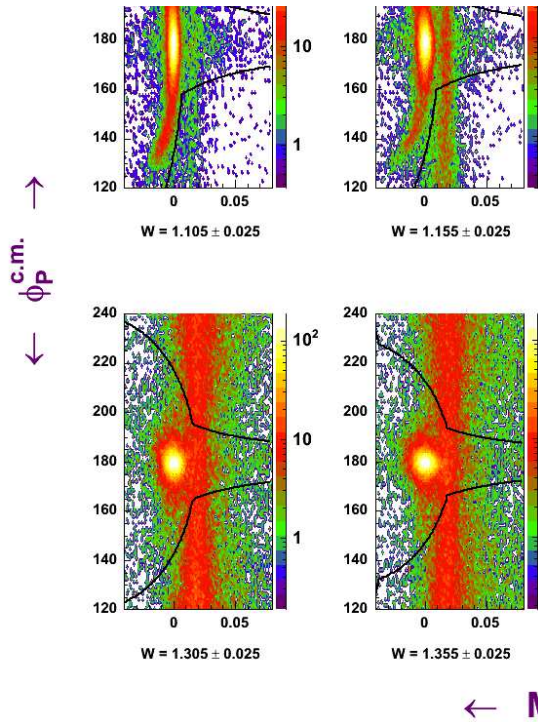


Figure 1.40: $\phi_P^{c.m.}$ versus missing mass M_x^2 for different W values.

One can immediately notice that the cut used eliminates some π^0 s around $\phi_P^{c.m.} = 180^\circ$. These events (and the ones eliminated with the second and third cut below) will be recovered with the MonteCarlo simulation because the exact same cut will be applied (see section 2.3). The closer to data the model used for the simulation, the more accurate will be this recovery.

In Figure 1.41 is plot the (eP) missing mass M_x^2 versus $\Delta\theta$ distribution. One can see the pre-radiative events showing at $x = 0$ and leaking in the π^0 events (horizontal band at $M_x^2 \simeq M_{\pi^0}^2 = 0.0182 \text{ GeV}^2$). The (moving with W) spot on the left refers to post radiation events.

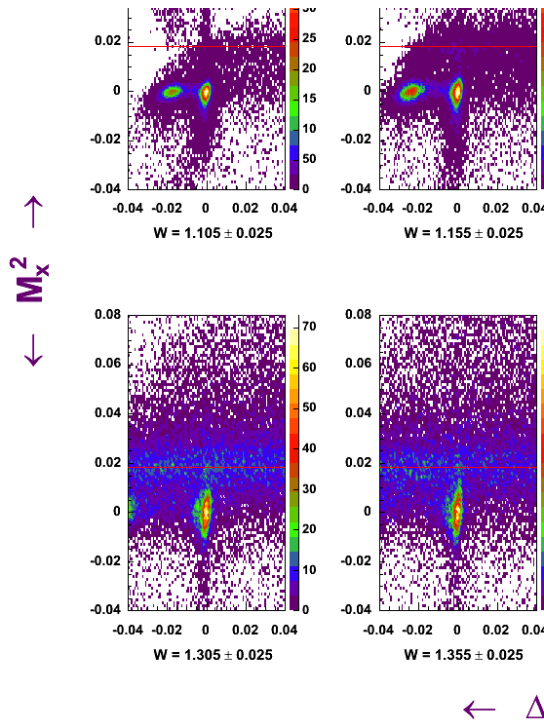


Figure 1.41: missing mass M_x^2 versus $\Delta\theta$ for different W values before the $\phi_P^{c.m.}$ versus missing mass M_x^2 cut. The post-radiative elastic events peak at $x = 0$, while the other spot on the left is due to pre radiation. The horizontal line is at the π^0 mass.

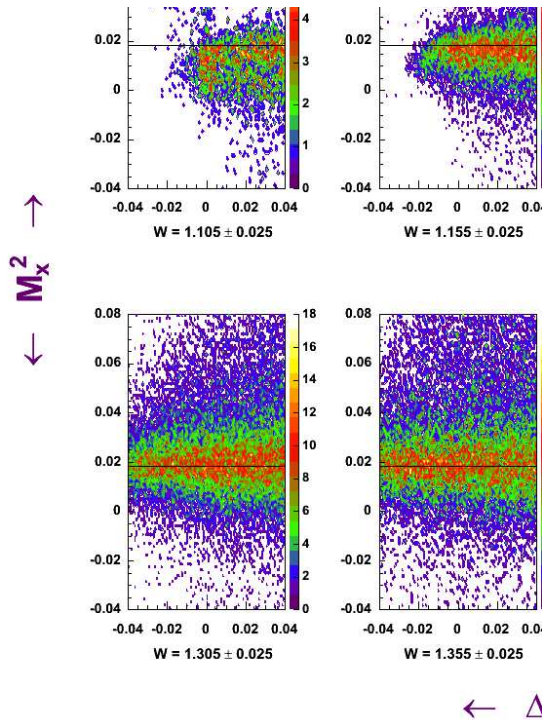


Figure 1.42: missing mass M_x^2 versus $\Delta\theta$ for different W values after the $\phi_P^{c.m.}$ versus missing mass M_x^2 cut. The horizontal line is at the π^0 mass.

Figure 1.42 shows the effect of the first cut on the missing mass M_x^2 versus $\Delta\theta$ distribution. Most of the pre and post radiative events are eliminated but some residual pre-radiative B.H. events at low W survives.

For this reason a second cut is introduced:

$$|\Delta\theta| < 0.01 \text{ rad} \quad \text{when} \quad W < 1.21 \text{ GeV} \quad (1.5)$$

Some residual post radiative B.H. events survive the first and second cut. This can be seen in Figure 1.43 where missing mass M_x^2 is plotted versus $\Delta\theta_2$: a small band shows up at $\Delta\theta_2 \simeq 0$, particularly at low W .

The third cut considered, involving missing mass M_x^2 versus $\Delta\theta_2$, is:

$$M_x^2 < a + b \Delta\theta_2$$

where a, b vary with W .

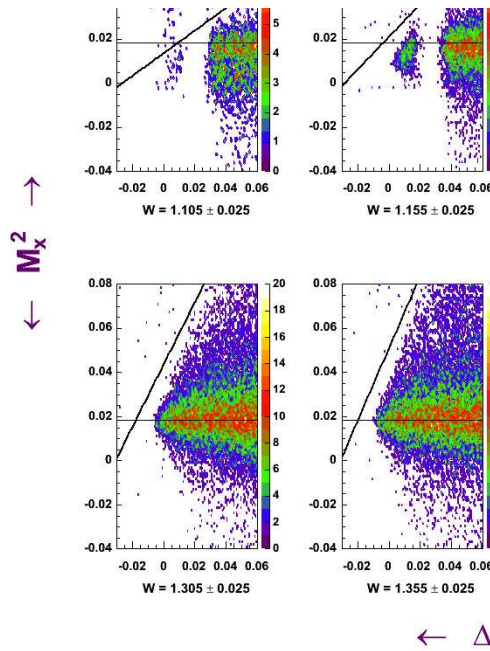


Figure 1.43: missing mass M_x^2 versus $\Delta\theta_2$ after the first two B.H. cuts. Residual post-radiative events are cut out with a straight line $y = a + bx$ whose parameters a and b vary with W . This plot shows also the effect of the second cut (1.5): at low W events with $\Delta\theta \simeq 0 \equiv \Delta\theta_2 \simeq 0.025$ disappeared. The horizontal line is at the π^0 mass.

After the three cuts described above a “clean” sample of π^0 events is ready for analysis. This is shown in Figure 1.44 where W and missing mass M_x^2 are plotted in blue for the events surviving the cuts.

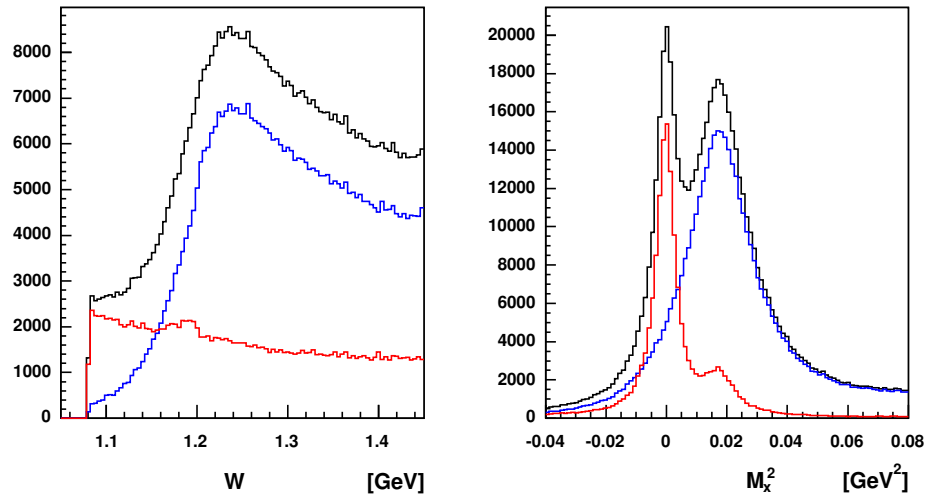


Figure 1.44: The effect of all the cuts on the W and missing mass M_x^2 distributions. Black line: before any cut. Red line: B.H events. Blue line: final π^0 events.

1.9 Čerenkov efficiency

The GSIM simulation does not reproduce accurately the Čerenkov detector due to the incomplete implementation of the detector optics. Furthermore the electron-pions contamination is not present in the simulation. For these reasons the pions and the PMT noise resulting in the peak at 1.0 $nphe$ illustrated in Figure 1.1 do not show in the MonteCarlo, so that the real electrons lost with the cut $nphe < 2.5$ would not be recovered with the acceptance calculation.

Studies [35], [39] of the $nphe$ spectra for the Čerenkov allow one to determine a correction to the simulation that resolves this problem. In Figure 1.45 the $nphe$ spectra is plotted for a particular electron ϕ, θ, p and sector. The distribution is fitted with the Poisson distribution

$$y = A \frac{L^{x/P}}{x/P} e^L \quad (1.6)$$

with A, P, L as parameters. The integral of the obtained function between $nphe = 0$ and $nphe = 25$ (shaded region) is a good estimate of the number of the electrons lost with the CC cut. The the efficiency

$$E = 1 - \frac{\int_0^{25} y dx}{\int_0^\infty y dx} \quad (1.7)$$

is calculated. It was found that there are low efficiency regions around the fiducial cut, as one can expect, but also at $\phi = 0$, as is shown in Figure 1.14.

An efficiency table is obtained with the following binning:

- $0 < p < 5$ GeV in steps of 0.5 GeV.
- $5^0 < \theta < 50^0$ in steps of 5^0 .
- $-25^0 < \phi < 25^0$ in steps of 3.3^0 .

When calculating the acceptance, each MonteCarlo event is weighted by the CC efficiency.

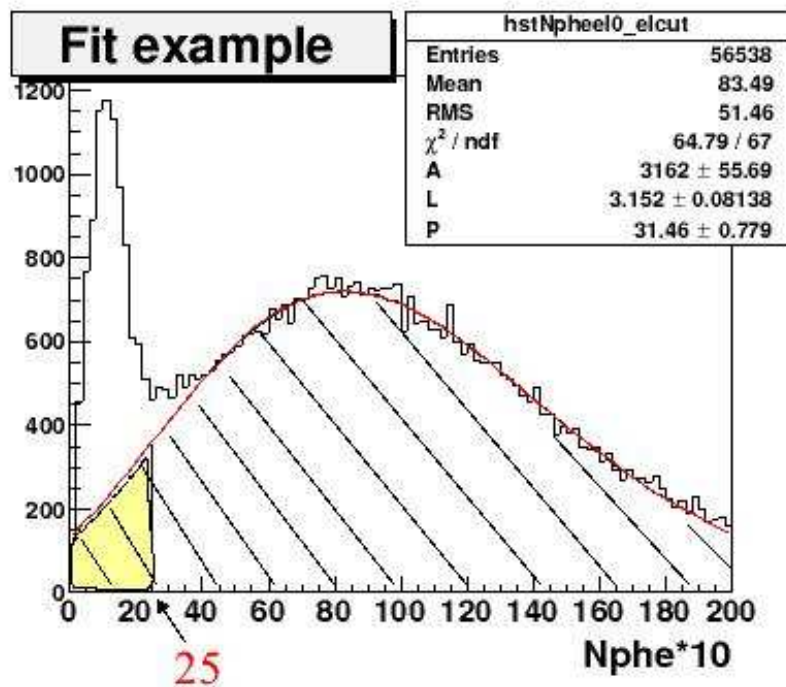


Figure 1.45: The $nphe * 10$ spectra for $1.1 < p < 1.5$ GeV, $35^0 < \theta < 45^0$, $15^0 < \phi < 25^0$ and sector 1. The histogram is fitted for $nphe > 2.5$ with a Poisson distribution. The integral of the obtained function between $nphe = 0$ and $nphe = 2.5$ (shaded region) is a good estimate of the number of the electron lost with the CC cut.

CHAPTER 2

Acceptance

2.1 Geometrical acceptance

A geometrical acceptance is calculated using a Monte Carlo technique. Events are generated flat in the variables W , Q^2 , $\cos\theta^*$, ϕ^* , ϕ_e , then the following quantities are calculated (see App. A for the meaning of the quantities)

$$\begin{aligned}\nu = q_0 &= \frac{W^2 + Q^2 - M_P^2}{2M_P} \Rightarrow E' = E - \nu \\ \cos\theta_{e'} &= \left(1 - \frac{Q^2}{2EE'}\right) \\ p_{\pi^0}^* = p_P^* &= \frac{\sqrt{(W^2 - (M_P + M_{\pi^0})^2)(W^2 - (M_P - M_{\pi^0})^2)}}{2W}\end{aligned}\tag{2.1}$$

so that the proton four momentum in the c.m. p_P^* and the electron four momentum in the lab e'_μ are obtained. A Lorentz transformation from the resonance system to the lab system gives the proton four momentum in the lab P'_μ .

The e'_μ and P'_μ four vectors are then subjected to the same cuts that make use of four vector momenta applied to real data. These are the fiducial cuts (sections 1.5 and 1.6) and the B.H. cuts (section 1.8). The acceptance A is calculated for each bin.

$$A = A(W, Q^2, \cos\theta^*, \phi^*) = \frac{\# \text{ accepted events}}{\# \text{ generated events}} (W, Q^2, \cos\theta^*, \phi^*)\tag{2.2}$$

This method is convenient because it is very fast: billions of events can be processed in only a few hours. However it does not take into account the detector response. For example effects like bin migration, multiple scattering, finite momentum resolution, do not enter in this model. Yet, the geometrical acceptance can be a good approximation for a real acceptance calculation. Figure 2.1 show an example of the acceptance distribution as a function of $\cos\theta^*$ and ϕ^* .

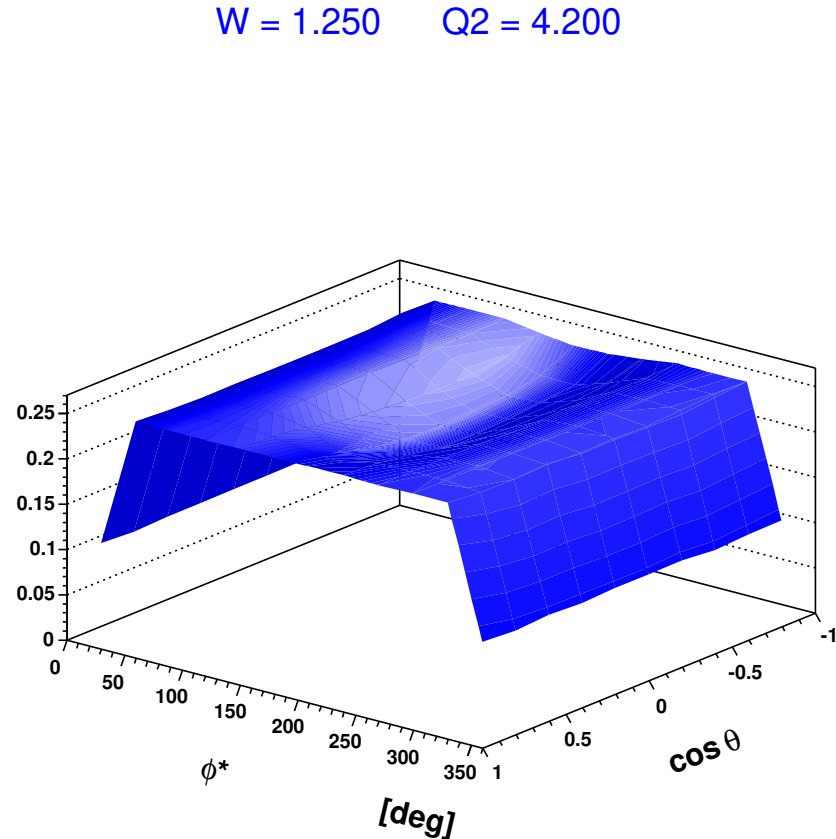


Figure 2.1: Geometrical acceptance for $1.24 \leq W \leq 1.26$ GeV and Q^2 from 3.79 to 4.52 GeV^2 as a function of the π^0 angles in the c.m. frame $\cos \theta^*$ and ϕ^* . The B.H. cut affects the distributions at $\phi_{\pi^0}^*$ extremes (0° and 360°) because it cuts out events with $\phi_P^* \sim 180^\circ$ (the pions and the proton have opposite momentum in the c.m.).

2.2 MonteCarlo simulation

A realistic acceptance calculation must take in account the CLAS detector geometry, efficiency and resolution. The program that simulates the response of CLAS is **GSIM** (**G**EANT **S**imulation) based on the GEANT 3 libraries developed at CERN. What follows are the steps to achieve the desired simulation.

2.2.1 Drift Chamber smearing

The DC resolution must be properly incorporated in the MonteCarlo. The steps below describe this procedure.

When a particle passes through a DC cell, see Figure 2.2, the sensible wire signals a drift time, which is then turned into distance from the wire, or *CalcDoca* (DOCA = distance of closest approach).

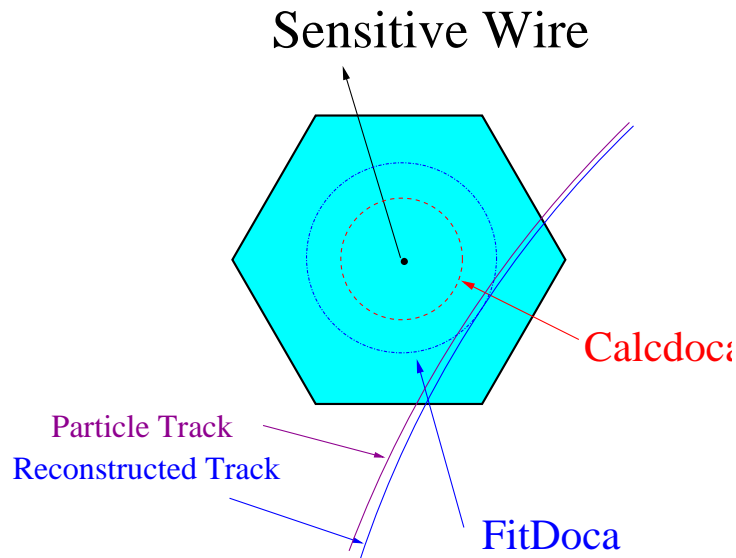


Figure 2.2: A charged particle passing through a DC cell. The drift time is converted into *CalcDoca* which is used by the tracking procedure to find the reconstructed track. The resulting distance from the wire, or *FitDoca*, is much closer to the real track.

During the tracking procedure the information from all the cells is taken into account so that the resulting *FitDoca*, the distance of the wire from the reconstructed track, will be much closer to the actual track.

The quantity

$$SR = |CalcDoca| - |FitDoca| \quad (2.3)$$

(called Spacial Residual) is a good estimate of the DC resolution because it measures the response of a single cell. This quantity is plotted against $FitDoca$ for the DC Region 3 in Figure 2.3. One can see that the mean and the σ of the distribution are not constant, however only the σ can be incorporated in the MonteCarlo¹.

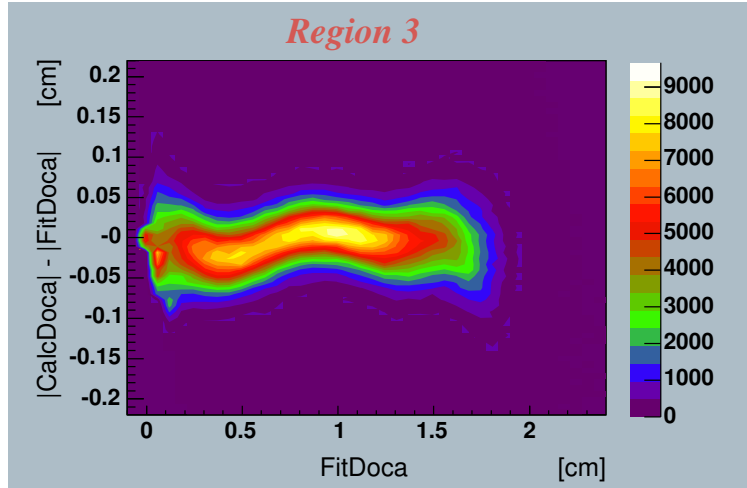


Figure 2.3: The space residual for DC Region 3. The mean and the σ of the distribution are not constant.

The distribution in Figure 2.3 is sliced along the $y-axis$ and each slice is fitted with a gaussian distribution. The result is plotted in Figure 2.4, where a fit is performed. This procedure is applied for each region of the DC. It was found that the sector or superlayer dependance of the σ distribution is negligible. The parameters of the fit in Figure 2.4 are incorporated in the MonteCarlo (by mean of a mysql database).

¹The mean position comes from the convolution, which is unknown, of the actual position in the cell with the tracking procedure. The σ is not affected by this convolution.

In Figure 2.5 is shown the comparison of real data (black) and the obtained MonteCarlo (red) DC resolution for Region 2. The simulated and true data shows good agreement.

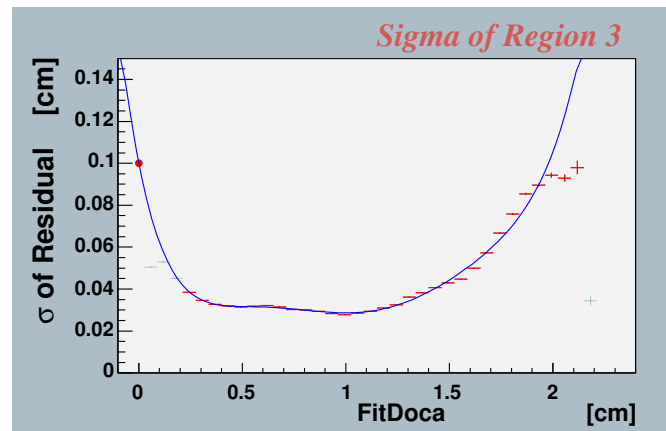


Figure 2.4: The σ of the space residual for DC Region 3. The parameters of the fit are incorporated in the MonteCarlo (by mean of a mysql database).

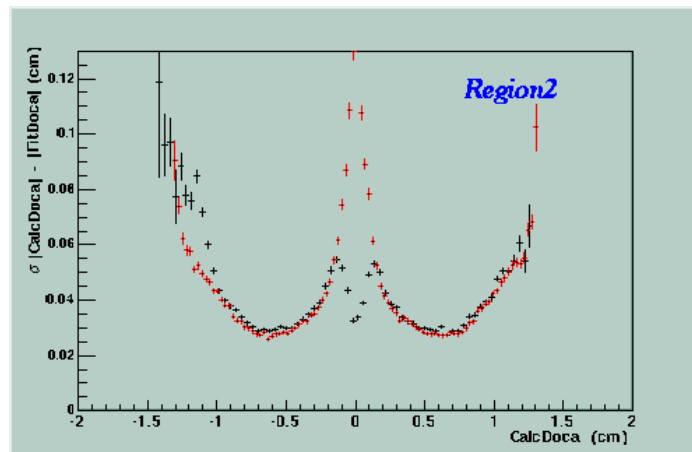


Figure 2.5: Comparison of real data (black) and MonteCarlo (red) DC resolution for Region 2. The difference at $FitDoca \sim 0$ is due to the fact that the residual for the MonteCarlo is calculated before tracking (it is in fact the actual resolution of the cells).

2.2.2 Time of flight smearing

The GSIM simulation of the TOF detector presents finer resolution than for real data. This is shown in Figure 2.6 where the TOF proton mass M^2 , calculated as in Section 1.3, is plotted for real data and MonteCarlo events. Since the proton identification is based on M , it is important that the simulation reproduces this quantity precisely.

It was found that the mean position of M^2 differs between data and simulation due to an imperfect calibration². This is not important because the cuts include such a shift.

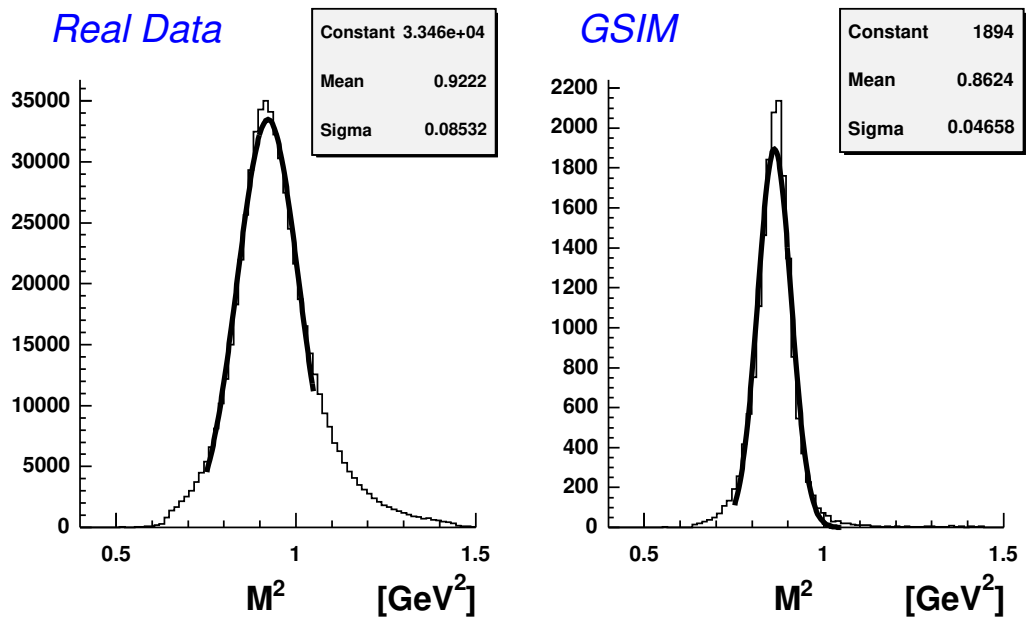


Figure 2.6: Square of TOF mass M^2 . Left: real data π^0 events. Right: MonteCarlo MAID 2000 simulation. The mean position is different due to imperfect calibration of the TOF bars . The MonteCarlo data show a finer resolution: $\sigma_{REAL} = 0.085 \text{ GeV}^2$ while $\sigma_{GSIM} = 0.047 \text{ GeV}^2$.

However the simulation should show the same resolution if one wants to make sure that the background is handled in the same way as the real data. In order to smear the GSIM TOF a realistic σ from a calibration study [47] shown in Figure 2.7 was used. The function shown in the plot makes sure that the response of the MonteCarlo TOF resembles the real data case.

In order to perfectly match the real data and MonteCarlo TOF resolution a few

²The TOF is calibrated using electrons and pions as reference. As a consequence the protons timing is shifted.

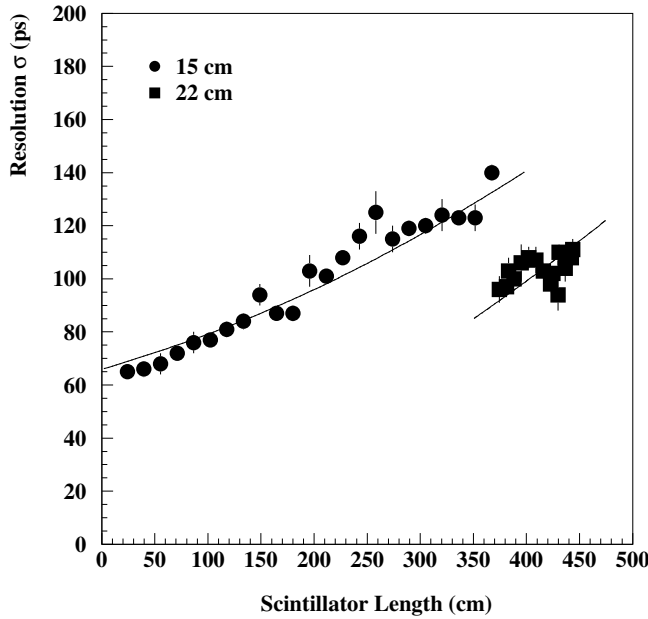


Figure 2.7: The timing resolution as determined from cosmic ray tests (see [47] for details). The curve represent the resolution (for two different paddle sizes) used to smear the MonteCarlo TOF response.

simulations of 20,000 events each were performed. In each simulation the function in Figure 2.7 was multiplied by a trial number f (from 0.5 to 1.4) and used to smear the TOF signal. In each case the resulting TOF mass was fitted with a gaussian and the obtained σ are plotted versus the multiplicative number f . This is shown in Figure 2.8 where the real data σ are also plotted. One can clearly see that σ is linear with f .

The value $f = 1.35$ matches the real data resolution and therefore is the value used throughout all the GSIM simulation.

2.2.3 Drift chamber inefficiencies

The Drift Chambers present inefficiencies which must be taken into account by the MonteCarlo simulation for a correct acceptance calculation. As the DC is repaired or fails with time, each experiment has a different drift chamber status. Some systems (for example HV) might fail during the experiment.

What follows is the description of the calculation of a global DC efficiency to exploit at once the DC inefficiency and theirs time dependency.

Each CLAS sector has the same drift chamber configuration, shown in Table 2.1, which consists of three separate regions containing a total of 34 layers of sense wires. Region 1 has four layers, region 2 and 3 have six layers each.

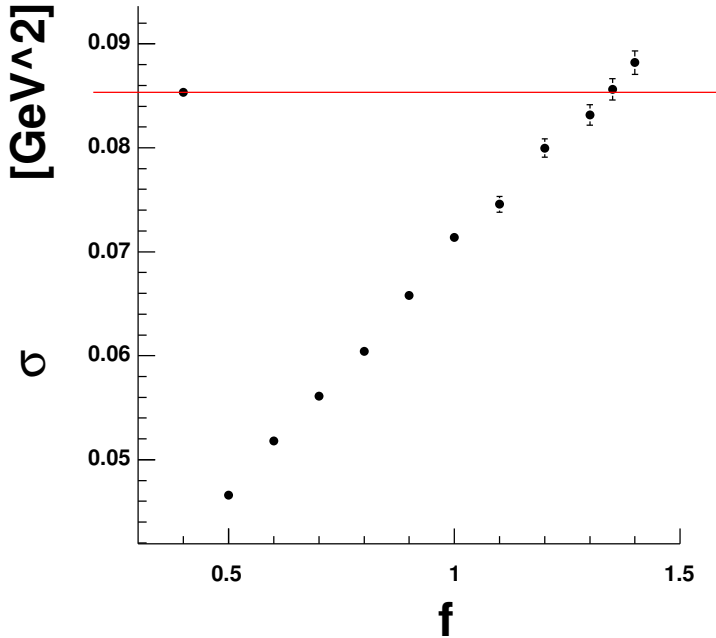


Figure 2.8: σ as a function of the smearing factor f . The first point is the real data resolution (red line). The real resolution is matched at $f = 1.35$.

Layer	1	2	3	4	5	6	7	8	9	10	11	12
Region 1	130	130	130	130	0	0	142	142	142	126	121	120
Region 2	184	185	186	187	188	189	189	189	190	191	192	192
Region 3	192	192	192	192	192	192	192	192	192	192	192	192

Table 2.1: Number of wires in each layer. Region 1 has only 4 layers, so layers 5 and 6 are phantom.

Figure 2.9 shows the occupancy of the drift chamber in sector 6 for the e1-6 experiment.

There are three wires pathologies:

- *holes*: there are nearly no counts in layers 34,35,36 near wire number 150. This is an example of a *hole*. During tracking, a hole could affect track reconstruction because a minimum number of wires are required to define a track.
- *hot* wires: Wires that count significantly more than neighboring ones are “hot”. Track reconstruction is basically undisturbed by those³.
- *warm* wires: wires that count less than neighboring ones but not *substantially less*. For example, a wire can count an average of 70% relative to its neighbours.

³This is an empirical statement.

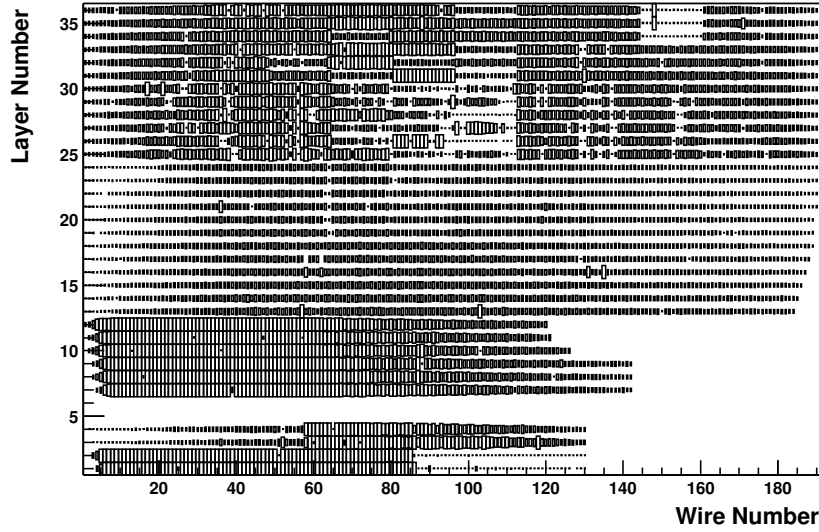


Figure 2.9: Drift chamber occupancy distribution for sector 6. A hole is visible in layers 34–36 near wire number 150.

Some warm wires could be correlated. For example they could be attached to the same (defective) ADB board⁴, so that all wires in that board have *the same efficiency at the same time*. Correlated wires affect tracking in that a group of wires might miss at the same instant, preventing the creation of a track segment.

In order to calculate the efficiency of a wire, the whole e1-6 period has been considered. If a wire has 50% efficiency it could mean that

- it was efficient only half of the time, i.e. the chance of give a signal is 50%
- the wire was alive for half the experiment and dead for the other half.

so that the time dependency problem of the DC has been solved.

For each $w(i, S)$ of the 36,000 wires, with i being the wire index and S its sector, a sample of 18 wires has been considered: its next neighbors in the same sector $w(i-1, S)$ and $w(i+1, S)$ and the corresponding wires in all the other sectors $w(i, S')$, $w(i-1, S')$, $w(i+1, S')$. Table 2.2 shows one example of such a sample.

For each wire w_J in the above sample, with $J = 1 \dots 18$, the variable *buddies* represents the number of wires in the same sample whose occupancy is within 8% of w_J , as illustrated in Figure 2.10.

⁴An Amplifier Discriminator Board is a power supply unit. With a 60Hz varying gain of threshold it might give a correlated efficiency.

Layer	Sector 1	Sector 2	Sector 3	Sector 4	Sector 5	Sector 6
i_o	670080	674517	681877	678828	676214	2207
$i_o - 1$	736412	734450	738558	746698	739865	5281
$i_o + 1$	678419	665103	685710	105299	410887	677456

Table 2.2: Example of 18 wires sample from real CLAS data. For each of the 36,000 wires a similar sample is taken.

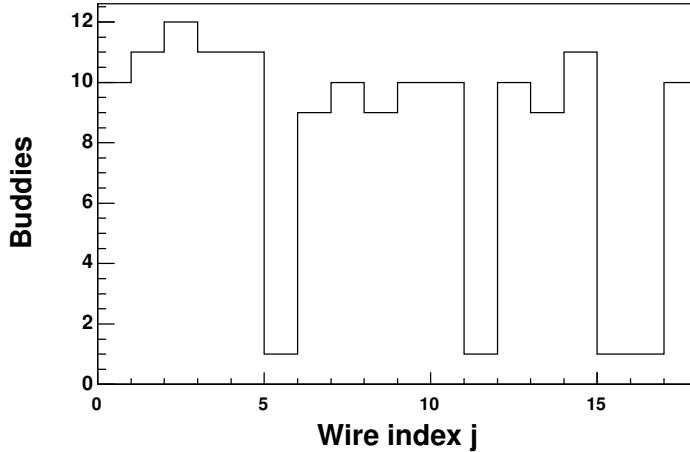


Figure 2.10: The next neighbor technique: the *buddies* histogram. Wire 3 has the maximum number of *buddies*.

The sub-sample that maximizes *buddies* is formed by good wires⁵. In this example wire 3 has 12 buddies.

The sub-sample is used to calculate the expectation value A for the occupancy of $w(i, S)$. A is the average of the occupancy in the the sub-sample. (in the example of table 2.2 and Figure 2.10 $A = 695191$).

The efficiency of $w(i, S)$ is in this case

$$E = \text{Occupancy}/\text{Expectation} = 670080/695191 = 0.96387$$

An efficiency table was incorporated in clas database and the GSIM MonteCarlo output is processed so that the simulated wire occupancy is a good representation of the real one [49]. Figure 2.11 shows the comparison of real and simulated efficiency for sector 5.

⁵Since usually there are $\sim 5,000$ defective wires among the 36,000, the probability that they maximize *buddies* is negligible.

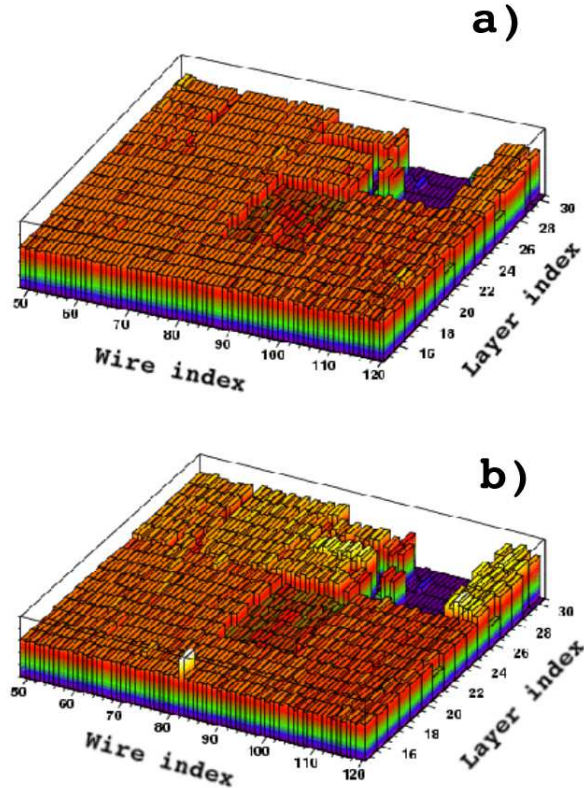


Figure 2.11: Comparison between real and simulated efficiency (z -axis) for sector 5. (a) simulation. (b) real data. A hole at layers 26 – 28 is visible. A Depleted region at layers 20 – 24 is also visible. The hot wire ($i = 80$) is not reproduced in the MonteCarlo because it does not affect the tracking.

2.3 Bethe Heitler events

As a check for the cuts applied in Section 1.8 to remove the elastic radiative tail, and to verify that the π^0 's lost with those cuts are properly taken into account, the same cuts are applied to the MonteCarlo simulation. Elastic events with radiative tail were generated and combined with the MonteCarlo π^0 events.

The cut described in Figure 1.40 is reproduced in Figure 2.12 for the MonteCarlo. A good agreement is found for the resolution in each W bin and the spread and position of the elastic radiative tail.

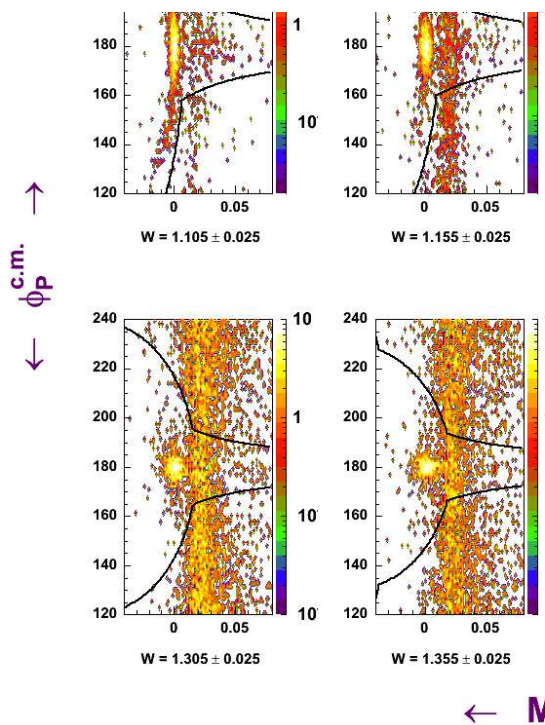


Figure 2.12: $\phi_P^{c.m.}$ versus missing mass M_x^2 for different W values for the MonteCarlo events. Good agreement with the data plotted in Figure 1.40 is found.

In Figure 2.13 is shown the missing mass M_x^2 spectra for data and MonteCarlo. One can see π^0 events lost in the data with the Bethe-Heitler cuts are also lost in the MonteCarlo so that they will be recovered with the acceptance calculation.

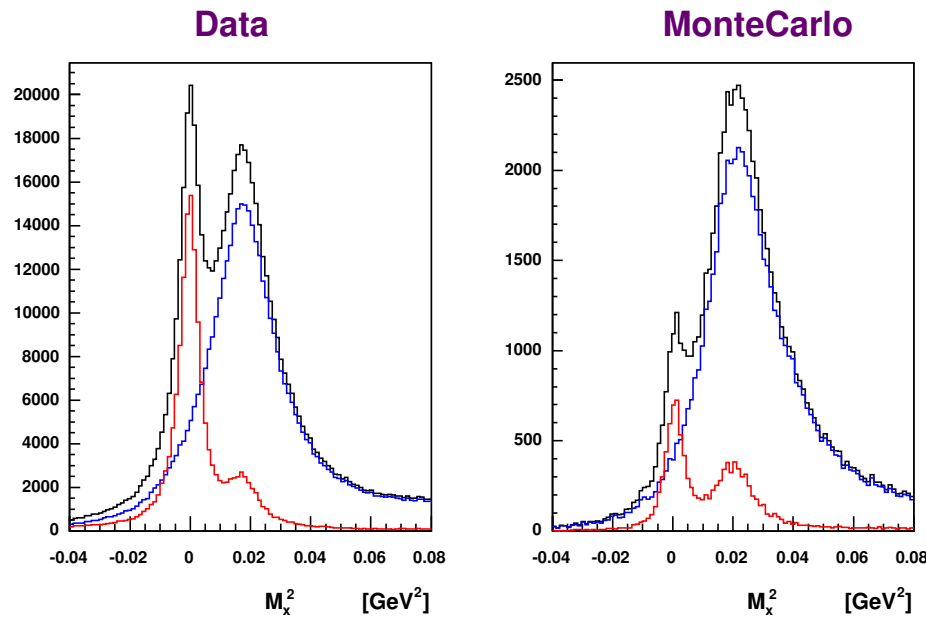


Figure 2.13: Missing mass M_x^2 spectra for data (left) and MonteCarlo (right). π^0 events lost in the data with the Bethe-Heitler cuts are also lost in the MonteCarlo.

2.4 Comparison between data and MonteCarlo

A final check on the quality of the MonteCarlo simulation is shown in Figure 2.14 where the missing mass M_x^2 spectra is plotted for different values of kinematic variables. A good agreement is found between data and MonteCarlo for the whole range of W and Q^2 .

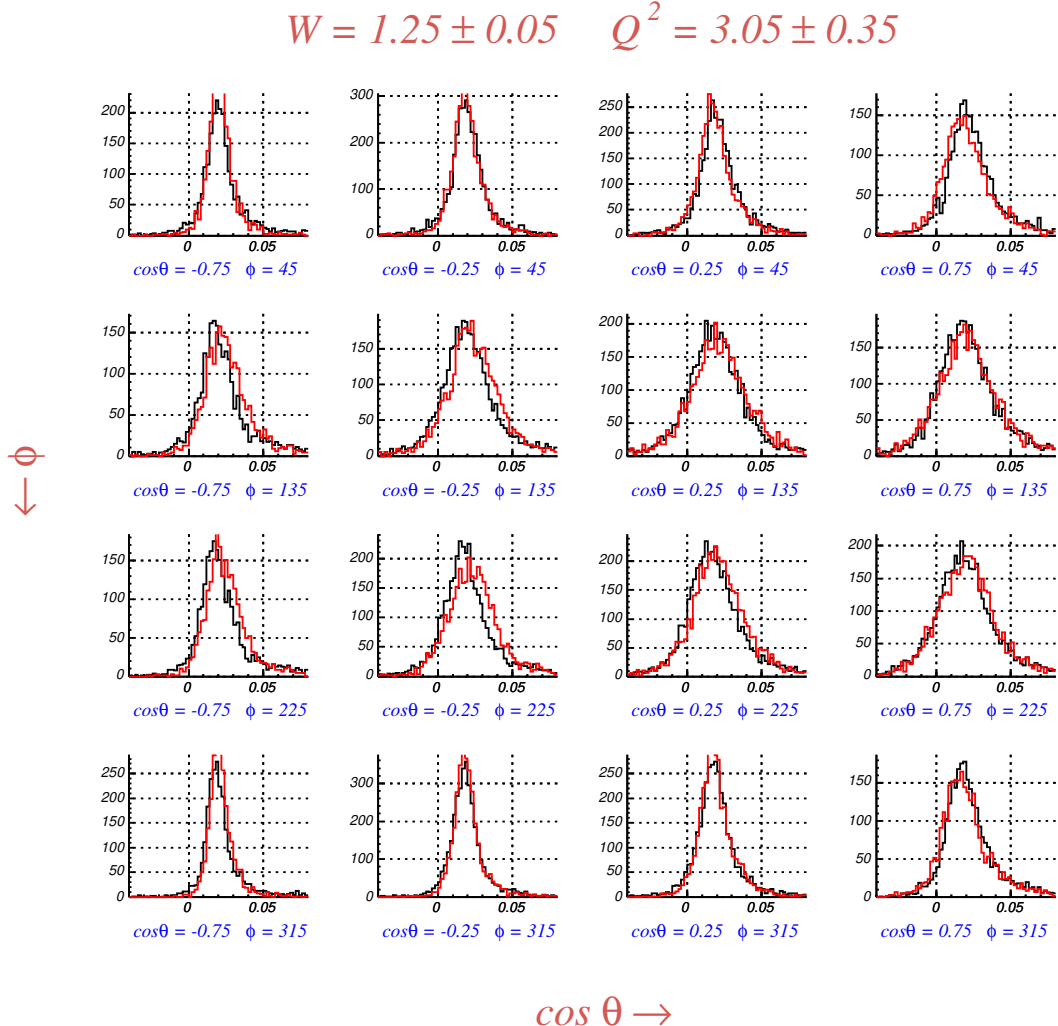


Figure 2.14: Missing mass M_x^2 spectra for data (black) and MonteCarlo (red) for $1.2 < W < 1.3$, $Q^2 = 3.05 \pm 0.35$ and different ϕ^* , $\cos \theta^*$ values. A good agreement for mean position and resolution in different region of phase space is found.

See

http://www.jlab.org/~ungaro/pi0eprod/com_phi

http://www.jlab.org/~ungaro/pi0eprod/com_miss
http://www.jlab.org/~ungaro/pi0eprod/com_costh

for a bin by bin comparison of the ϕ^* , $\cos \theta^*$, missing mass M_x^2 between data and Monte-Carlo distributions.

2.5 Acceptance calculation

In each bin considered for the analysis (see Section 3.1) the acceptance A is the ration of the number R of generated events to the number G of generated events:

$$A = \frac{R}{G} \quad (2.4)$$

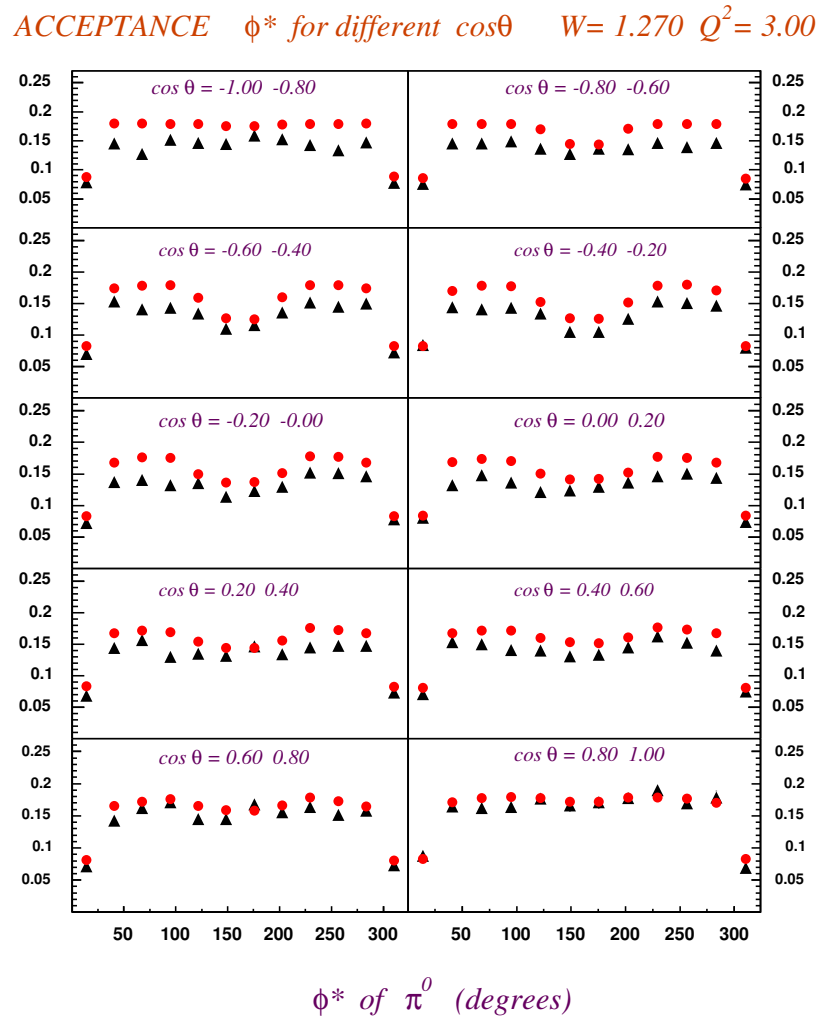


Figure 2.15: Acceptance calculation for $1.26 \leq W \leq 1.28$ GeV and $Q^2 = 3.0$ GeV 2 . Red: geometrical acceptance. Black: MonteCarlo acceptance.

In Figure 2.15 and Figure 2.16 the acceptance (black triangles) is shown as a function of ϕ^* for different $\cos\theta^*$. The geometrical acceptance (red points) is shown for comparison.

The difference between the two distributions is due to various effects as detector efficiency, bin migration, detector resolution.

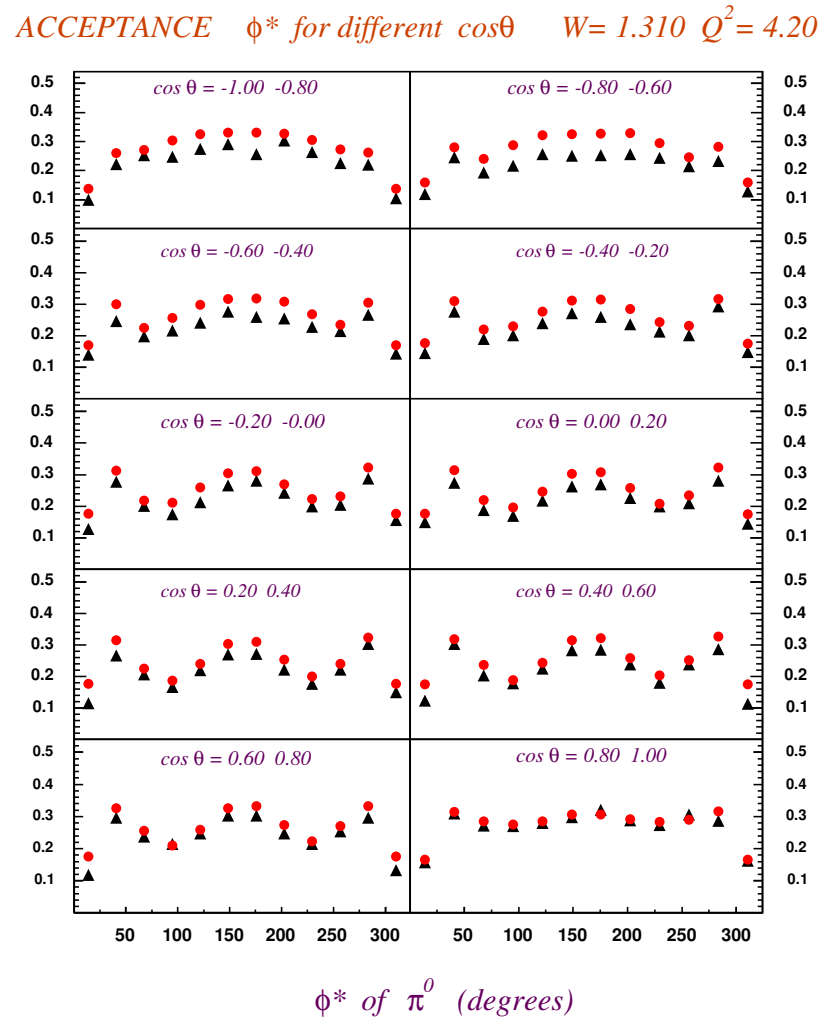


Figure 2.16: Acceptance calculation for $1.30 \leq W \leq 1.32$ GeV and $Q^2 = 4.2$ GeV 2 . Red: geometrical acceptance. Black: MonteCarlo acceptance.

See

http://www.jlab.org/~ungaro/pi0eprod/acc_plots

for the acceptance correction in each bin considered as a function of ϕ^* or $\cos\theta^*$.

CHAPTER 3

Analysis

3.1 Bins size

The choice of bins size in the variables W , Q^2 , $\cos \theta^*$, ϕ^* is illustrated in Fig. 3.1 and Fig. 3.2. The bin sizes were chosen to agree with previous and ongoing analyses.

W was divided in 15 bins from 1.1 GeV to 1.4 GeV in step of $\Delta W = 0.02$ GeV. ΔQ^2 is variable and such that $\Delta Q^2/Q^2 \simeq 0.18$. The values are in table 3.1.

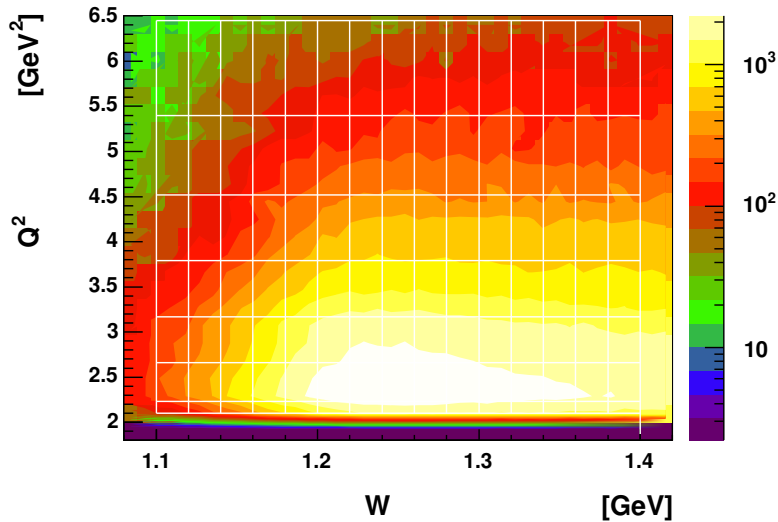


Figure 3.1: W and Q^2 binning for π^0 events (all angles). Notice the increasing ΔQ^2 size with Q^2 .

Q^2	2.15	2.4	3.0	3.5	4.2	5.0	6.0
Q^2_{min}	2.10	2.23	2.66	3.17	3.79	4.52	5.40
Q^2_{max}	2.23	2.66	3.17	3.79	4.52	5.40	6.45

Table 3.1: The binning in Q^2 .

The angular bins are taken as follows: $\Delta \cos \theta^* = 0.2$ and $\Delta \phi^* = 30^\circ$ so that there are 10 bins in $\cos \theta^*$ and 12 in ϕ^* as shown in Fig. 3.2.

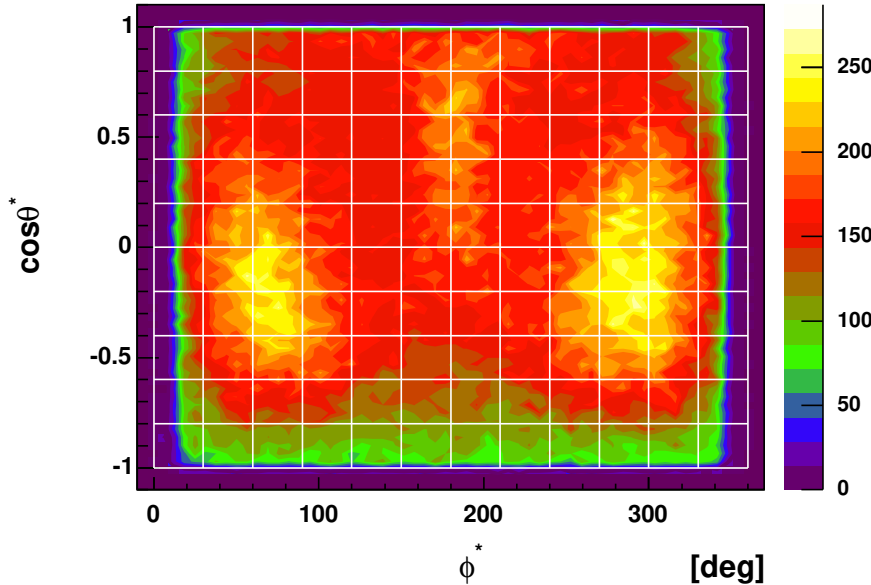


Figure 3.2: $\cos \theta^*$ and ϕ^* binning for π^0 events (all W and Q^2).

3.2 Bin averaging correction

When calculating the cross section, an average in each bin occurs (see Figure 3.3). If the cross section distribution is linear in all variables inside the bins then the value at center corresponds to the value obtained. This is not the case in the more realistic situation when the data distribution has some structure inside the bin.

To take in account this effect each bin was divided into subdivisions. The cross section in each subdivision (using a model) was calculated to obtain the average A in that whole bin. The value at the center of the bin C was calculated as well. The resulting correction is

$$R = \frac{C}{A}$$

The model **maid 2000 extended** [17] is used to calculate the correction. Each of the $15 \times 7 \times 12 \times 10 = 12600$ bins is divided into $15^4 = 50625$ subdivisions (15 for each of the variables $W, Q^2, \cos \theta, \phi$). This gives a total of ~ 600 million calculated cross section points. The correction in each bin is

$$R_{w, q^2, \cos \theta, \phi} = \frac{C_{w, q^2, \cos \theta, \phi}}{A_{w, q^2, \cos \theta, \phi}}$$

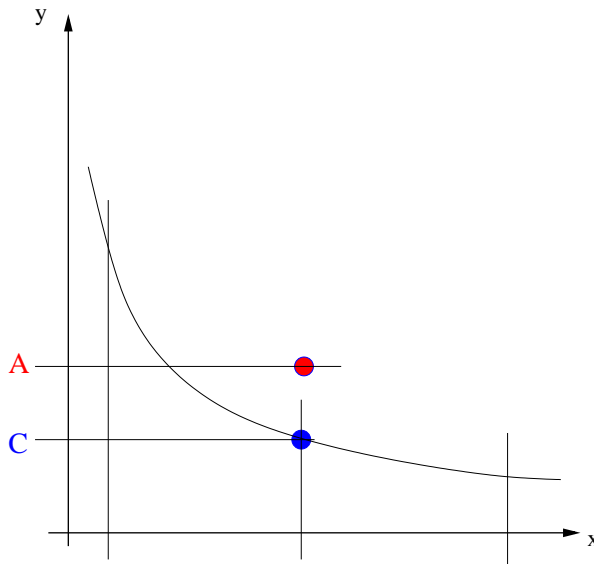


Figure 3.3: The bin correction. C is the value of the cross section at the center of the bin, while A is its average in that bin. The correction is $R = A/C$.

Figure 3.4 illustrates the correction as a function of $\cos \theta$, ϕ for different Q^2 bins at the peak of the $\Delta(1232)$ resonance.

See

http://www.jlab.org/~ungaro/pi0eprod/bin_ave

for the correction in each bin considered as a function of ϕ^* or $\cos \theta^*$.

3.3 Raw data

To see the statistic in each bin considered as a function of ϕ^* or $\cos \theta^*$ see See

http://www.jlab.org/~ungaro/pi0eprod/raw_plots

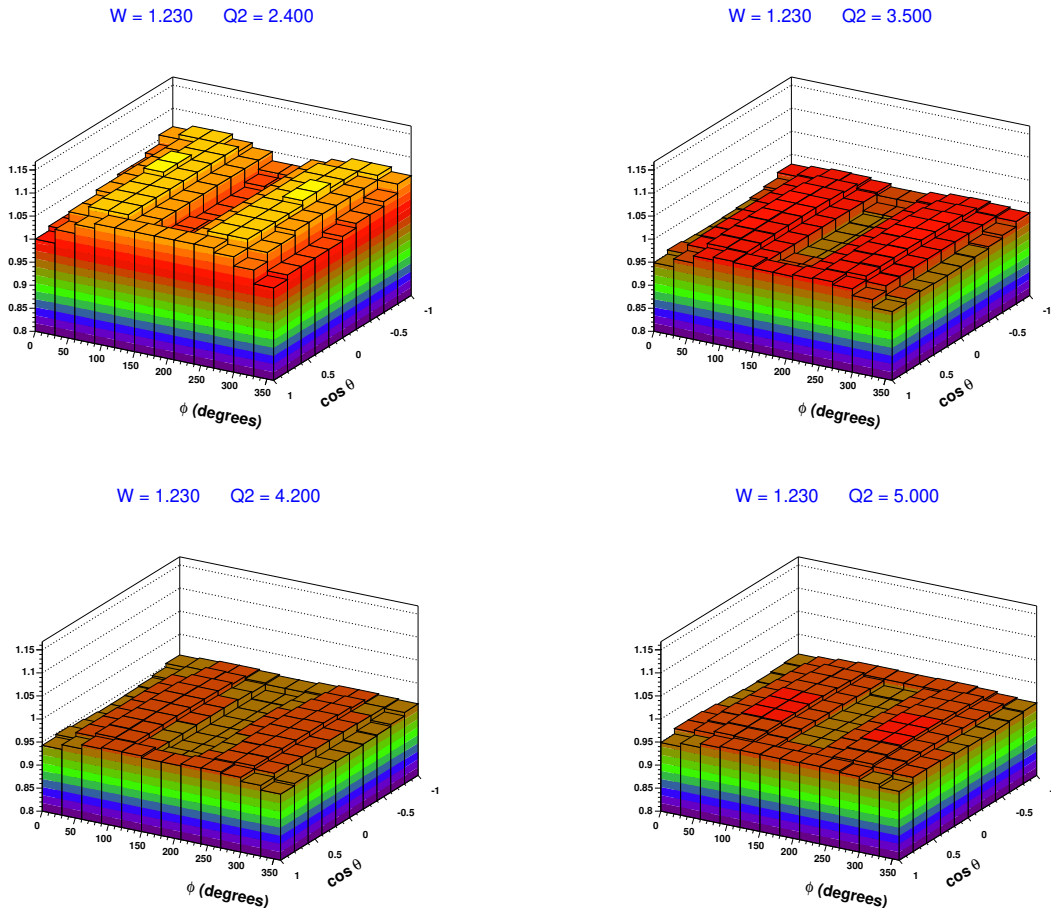


Figure 3.4: Bin averaging correction.

3.4 Radiative correction

The π^0 production illustrated in Figure 3.5 a) is not the only process contributing to the electroproduction cross section. A photon or a e^+e^- pair could be produced as well and the amplitudes of these processes interfere with each other. The measured W, Q^2 changes in case of radiation (for example the momentum of a scattered electron that emits a photon differs from the one at the leptonic vertex of Figure 3.5 b) so a *radiative correction* is necessary.

The following radiative processes are present (in the lowest order of the fine structure constant).

- the Bremsstrahlung, Figure 3.5 b) and c) where a photon is emitted by the incoming or outgoing electron.
- the vertex correction, Figure 3.5 d), where a photon is emitted by the incoming electron and absorbed by the outgoing electron.
- the vacuum polarization, Figure 3.5 e), where the virtual photon produces temporarily an e^+e^- pair.

To account for the radiative processes the approach of reference [2], which is based on a covariant method for infrared cancellation [7], is used . Multiple soft photon radiation is included via exponentiation [45], [50]. This method is preferred over Mo and Tsai the procedure [34] because:

- 1) It addresses *exclusive* electroproduction rather than inclusive, thus involving all four unpolarized structure functions, as opposed to the Mo and Tsai formalism which accounts only for two structure functions and inclusive scattering and it is independent of outgoing hadron angles. In principle, the general formulas of Mo and Tsai can be adapted to the coincidence framework if the integration over the photon phase space is done properly.
- 2) The infrared cancellation is independent of the unphysical parameter Δ separating the phase space of soft and hard photons necessary in the Mo and Tsai procedure and leading to uncertainties.
- 3) The approach of ref. [2] does not rely on the peaking approximation, avoiding uncertainties at a few percent level associated with it.

The matrix element of the unradiated process Figure 3.5 a) can be written as

$$M^2 = \frac{e^4}{Q^4} L_{\mu\nu} W^{\mu\nu} \quad (3.1)$$

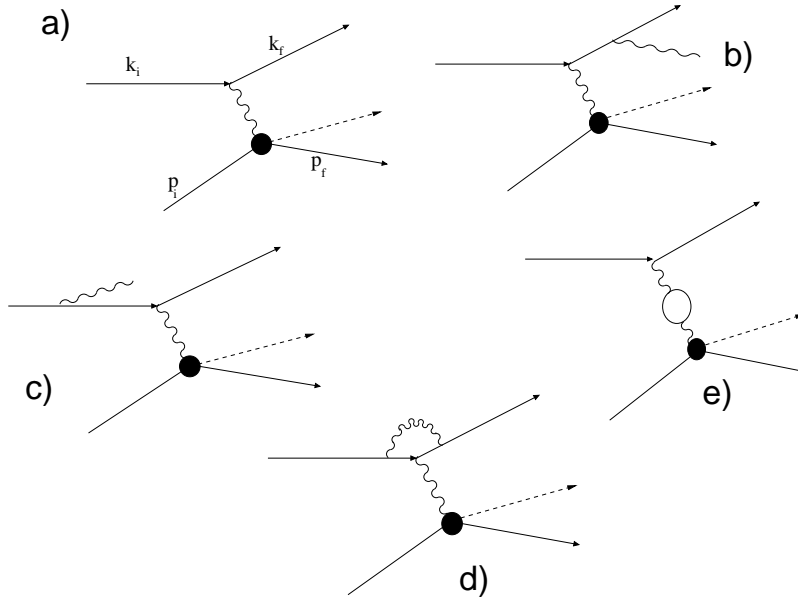


Figure 3.5: Feynman diagrams for the Born and radiative processes. a) Born electroproduction, b) and c) Bremsstrahlung d) vertex correction, e) vacuum polarization.

where $L_{\mu\nu}$ and $W^{\mu\nu}$ are the leptonic and hadronic tensors:

$$L_{\mu\nu} = \frac{1}{2} \text{Tr} (\not{k}_f + m) \gamma_\mu (\not{k}_i + m) (1 + i\gamma_5 \xi) \gamma_\nu \quad (3.2)$$

The leptonic tensor for the radiative processes illustrated in Figure 3.5 b), c), d) and e) changes into

$$L_{\mu\nu}^R = \frac{1}{2} \text{Tr} (k_f + m) \Gamma_{\mu\alpha} (k_i + m) (1 + i\gamma_5 \xi) \hat{\Gamma}_{\alpha\nu} \quad (3.3)$$

where the tensor $\Gamma_{\mu\alpha}$ contains the photon information k_γ^μ .

The contraction of $L_{\mu\nu}^R$ with $W^{\mu\nu}$ gives the matrix element M_R^2 for the radiative processes:

$$M_R^2 = -\frac{2e^6}{\tilde{Q}^4} L_{\mu\nu}^R W^{\mu\nu} = -\frac{2e^6}{\tilde{Q}^4 R_w} \sum_{i=1}^5 \theta_i H_i \quad (3.4)$$

where $\tilde{Q}^2 = -(q - k_\gamma)^2$ and $R_w = W^2 - (p + q - k_\gamma)^2$. One can see the involvement of

all the structure functions H_i and the intuitive modification to the normal definitions of \tilde{Q}^2 and R_w with the presence of a radiated photon.

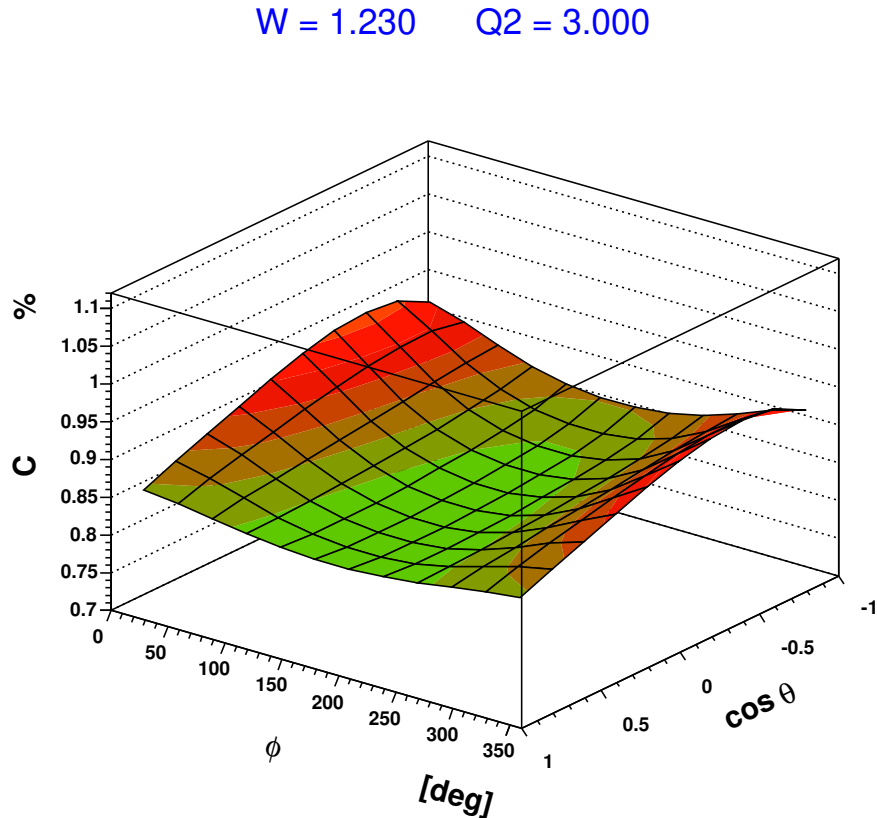


Figure 3.6: Radiative correction as a function of $\cos \theta^*$ and ϕ^* for $W = 1.23$ GeV and $Q^2 = 3$ GeV^2 .

A program named *EXCLURAD* which is described in [2] has been developed to calculate the matrix element (3.4) using existing models (like MAID or DMT) for the structure functions. This program gives the radiative correction C as the ratio of the radiative and unradiative four fold cross section:

$$C(W, Q^2, \cos \theta^*, \phi^*) = \frac{\sigma_{RAD}}{\sigma_{UNRAD}}$$

which has been used as the radiative correction in this analysis. Dependence on the missing mass cutoff parameter is tacit. Figure 3.6 shows the correction as a function of $\cos \theta^*$ and

ϕ^* for $W = 1.23$ GeV and $Q^2 = 3$ GeV 2 . Note that this procedure is different from that one followed for our published lower Q^2 data. See

http://www.jlab.org/~ungaro/pi0eprod/rad_plots/

for the correction in each bin considered as a function of ϕ^* or $\cos\theta^*$.

3.5 Extraction of the structure functions

The π^0 differential cross section in the resonance center of mass assumes the form

$$\frac{d\sigma}{d\Omega_{\pi^0}^*} = \frac{2Wp_{\pi^0}^*}{W^2 - m_P^2} \left(\sigma_T + \epsilon\sigma_L + \epsilon\sigma_{TT}\sin^2\theta\cos 2\phi + \sigma_{LT}\sqrt{2\epsilon_L(\epsilon+1)}\sin\theta\cos\phi \right) \quad (3.5)$$

where ϕ and θ are the azimuthal and polar angle of the π^0 in the c.m. frame and $\sigma_T, \sigma_L, \sigma_{LT}, \sigma_{TT}$ are the structure functions. The ϕ distributions are modulated only by the terms $\cos\phi$ and $\cos 2\phi$ while all the other terms vary with W, Q^2 and $\cos\theta$ (but not with ϕ). Therefore the structure functions can be extracted with a ϕ fit.

For each W, Q^2 and $\cos\theta$ bin the quantity in parenthesis is fitted with the functional form

$$y = a + b\cos\phi + c\cos 2\phi \quad (3.6)$$

The structure functions are then calculated with the formulas:

$$\begin{aligned} \sigma_T + \epsilon\sigma_L &= a \\ \sigma_{LT} &= \frac{b}{\sin\theta\sqrt{2\epsilon_L(\epsilon+1)}} \\ \sigma_{TT} &= \frac{c}{\sin^2\theta\epsilon_T} \end{aligned} \quad (3.7)$$

See

http://www.jlab.org/~ungaro/pi0eprod/cro_plots

for the cross section plots in each bin considered and for different cuts applied during this analysis.

Figure 3.7 shows the ϕ fits of the cross section for $W = 1.1 \pm 0.01$ GeV and $Q^2 = 2.4$ GeV 2 .

Figure 3.8 shows the χ^2/ν distribution for all the fits at different Q^2 values (black points) along with the expected χ^2/ν distribution (red line)

$$\chi^2/\nu(x) = \frac{2}{2^{\nu/2}\Gamma(\nu/2)} x^{\nu-1} e^{-x^2/2} \quad (3.8)$$

There are 12 bins in ϕ and there are 3 fit parameters therefore

$$\nu = N - \text{constraints} = 9.$$

Figure 3.9 shows $\sigma_L + \epsilon\sigma_T$ resulting from the fit at $Q^2 = 2.4$ GeV 2 .

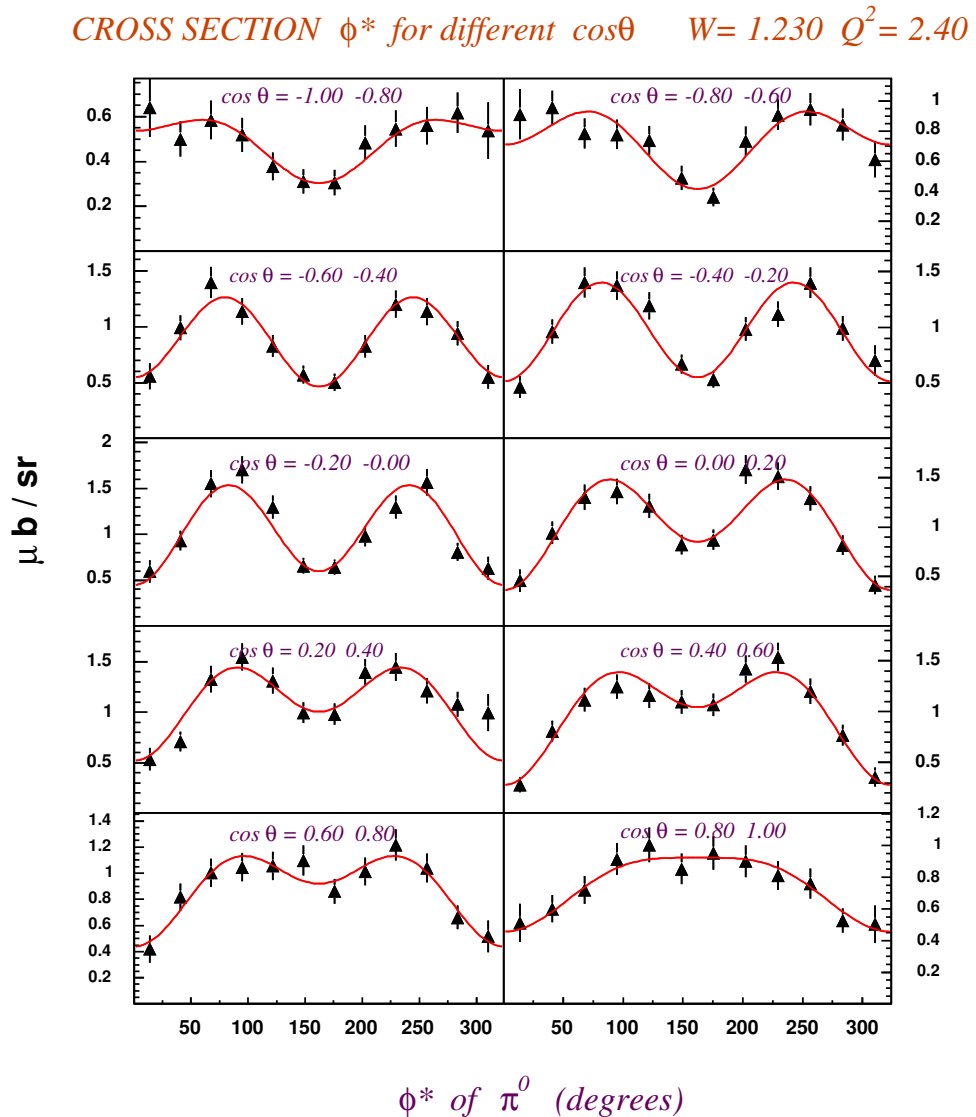


Figure 3.7: ϕ fits of the cross section for different $\cos\theta$ values. The function used for the fit is $y = a + b \cos\phi + c \cos 2\phi$ and the structure functions follow from the parameters a, b, c .

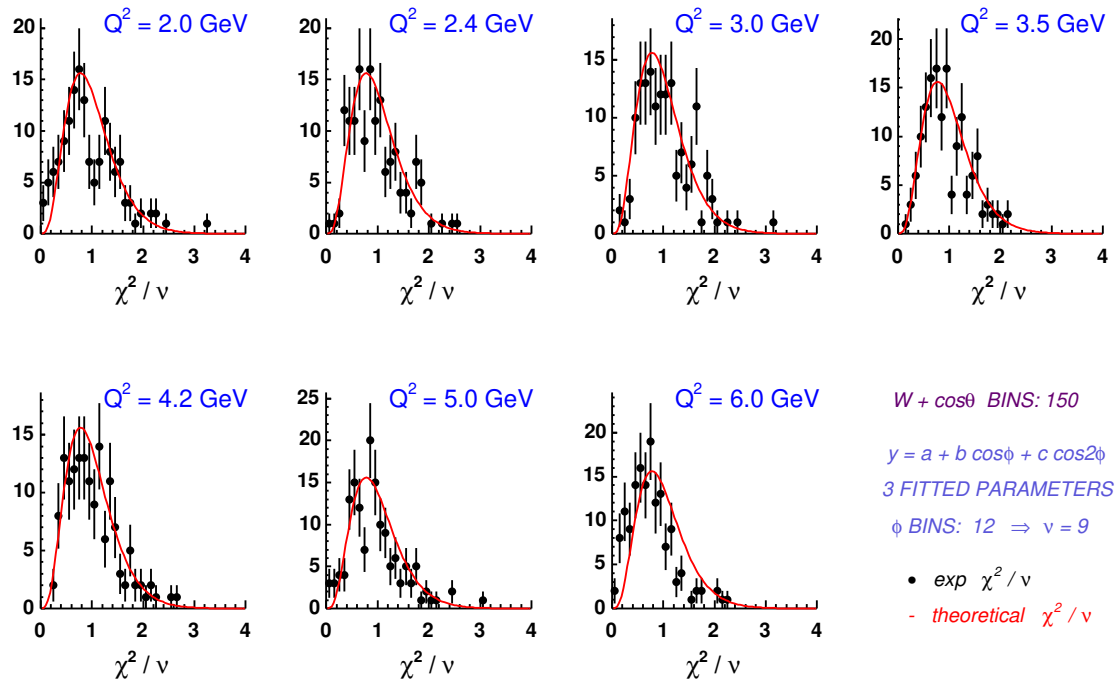


Figure 3.8: Reduced χ^2 distribution of the ϕ fits. The distributions show consistency with the expected χ^2 distribution for 150 fits (15 W bins and 10 $\cos \theta$ bins) and 9 degrees of freedom.

3.6 Multipole Truncation Analysis

While the extraction of the structure functions is model independent, assumptions on the partial waves of the background and other resonances have to be made in order to extract quantities such as the coefficients of the legendre expansion of the structure functions or the electromagnetic multipoles.

3.6.1 Legendre expansion

In order to extract the multipoles, the structure functions were fitted with orthogonal Legendre polynomials with ℓ up to d-waves (both the cases $\ell \leq 1$ and $\ell \leq 2$ have been considered). In the case of $\ell \leq 1$ the expansion is:

$$\begin{aligned}\sigma_T + \epsilon\sigma_L &= A_0 + A_1 P_1(\cos\theta) + A_2 P_2(\cos\theta) \\ \sigma_{TT} &= C_0 \\ \sigma_{LT} &= D_0 + D_1 P_1(\cos\theta)\end{aligned}$$

In the case of $\ell \leq 2$ the expansion is:

$$\begin{aligned}\sigma_T + \epsilon\sigma_L &= A_0 + A_1 P_1(\cos\theta) + A_2 P_2(\cos\theta) + A_3 P_3(\cos\theta) + A_4 P_4(\cos\theta) \\ \sigma_{TT} &= C_0 + C_1 P_1(\cos\theta) \\ \sigma_{LT} &= D_0 + D_1 P_1(\cos\theta) + D_2 P_2(\cos\theta)\end{aligned}$$

Figures 3.9, 3.10 and 3.11 show the fits for $\sigma_L + \epsilon\sigma_T$, σ_{TT} and σ_{LT} for different W at $Q^2 = 2.4 \text{ GeV}^2$. Figure 3.12 shows the obtained and the expected χ^2/ν distributions for the various response functions.

To see the fits for $\sigma_L + \epsilon\sigma_T$, σ_{TT} and σ_{LT} for all the Q^2 bins and $\ell \leq 1$ and $\ell \leq 2$ cases, see

<http://www.jlab.org/~ungaro/pi0eprod/responses>

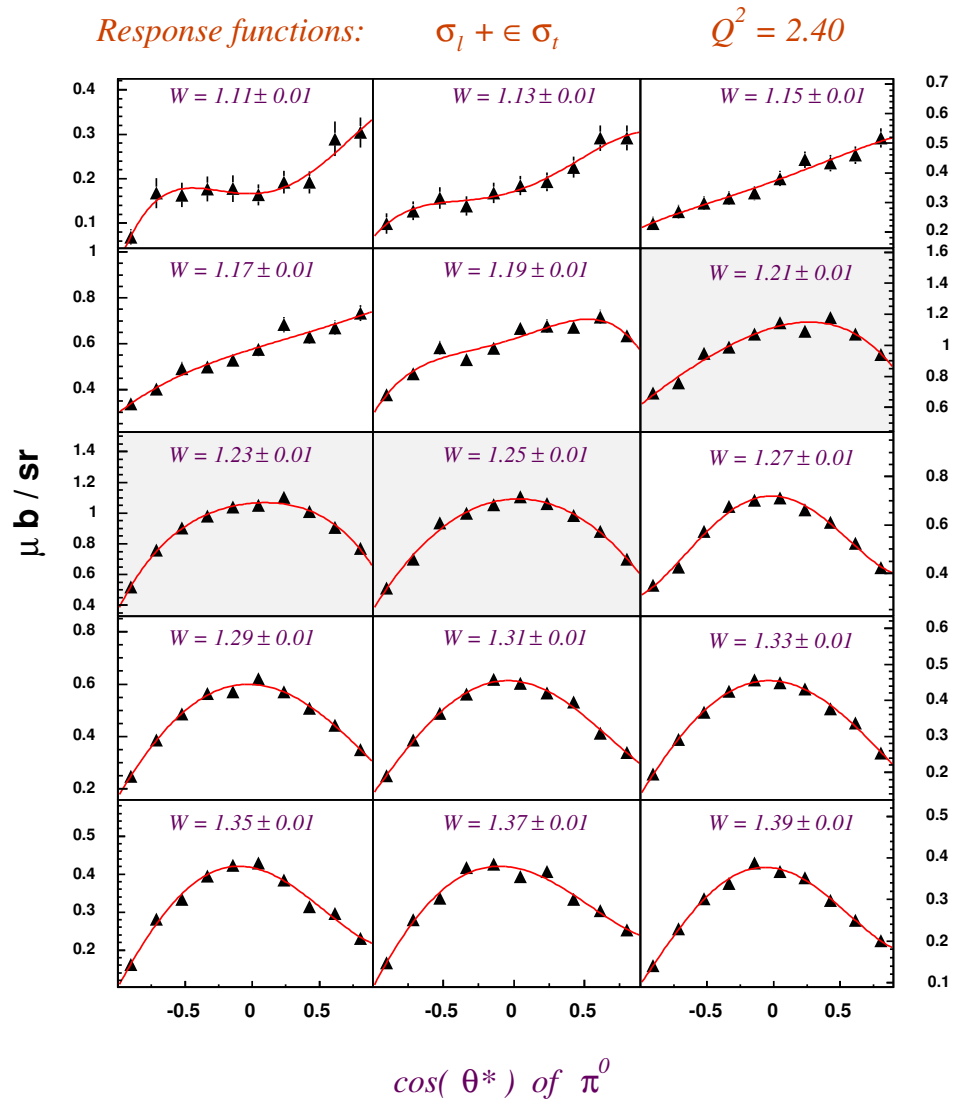


Figure 3.9: $\sigma_L + \epsilon\sigma_T$ for different W at $Q^2 = 2.4$ GeV 2 . The legendre expansion (red line fit) is: $\sigma_T + \epsilon\sigma_L = A_0 + A_1 P_1(\cos\theta) + A_2 P_2(\cos\theta) + A_3 P_3(\cos\theta) + A_4 P_4(\cos\theta)$. Regions near the Δ region are shaded.

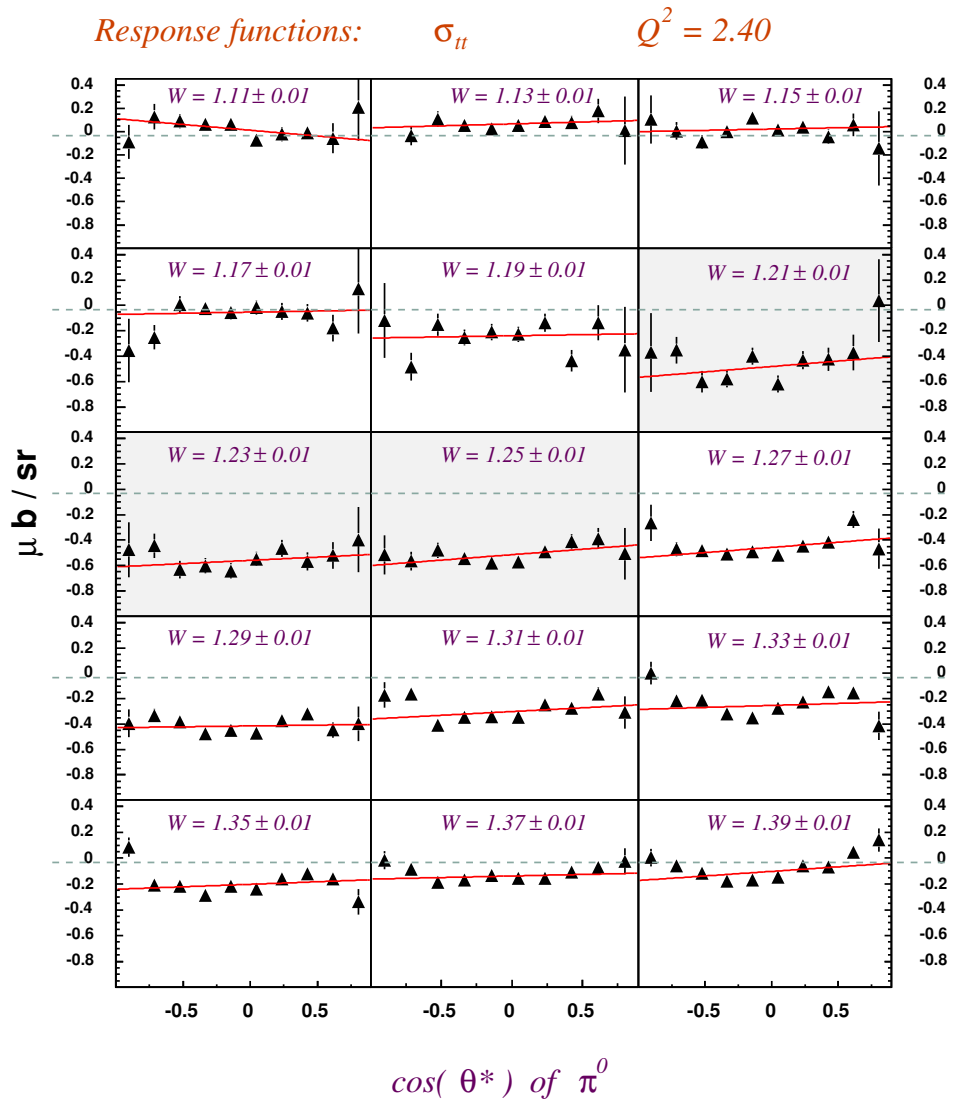


Figure 3.10: σ_{TT} for different W at $Q^2 = 2.4$ GeV 2 . The legendre expansion (red line fit) is:
 $\sigma_{TT} = C_0 + C_1 P_1(\cos\theta)$.
Regions near the Δ region are shaded.

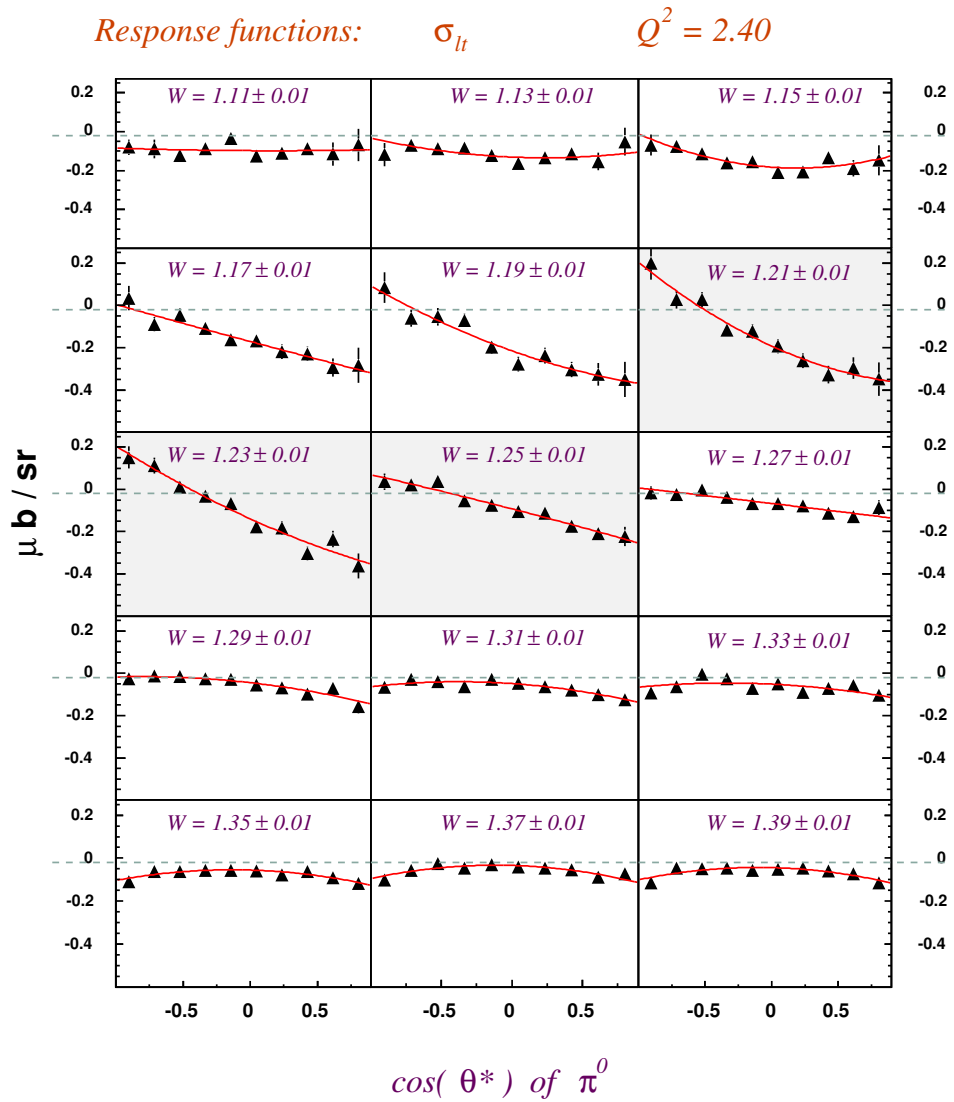


Figure 3.11: σ_{LT} for different W at $Q^2 = 2.4$ GeV 2 . The legendre expansion (red line fit) is:

$$\sigma_{LT} = D_0 + D_1 P_1(\cos\theta) + D_2 P_2(\cos\theta).$$

Regions near the Δ region are shaded.

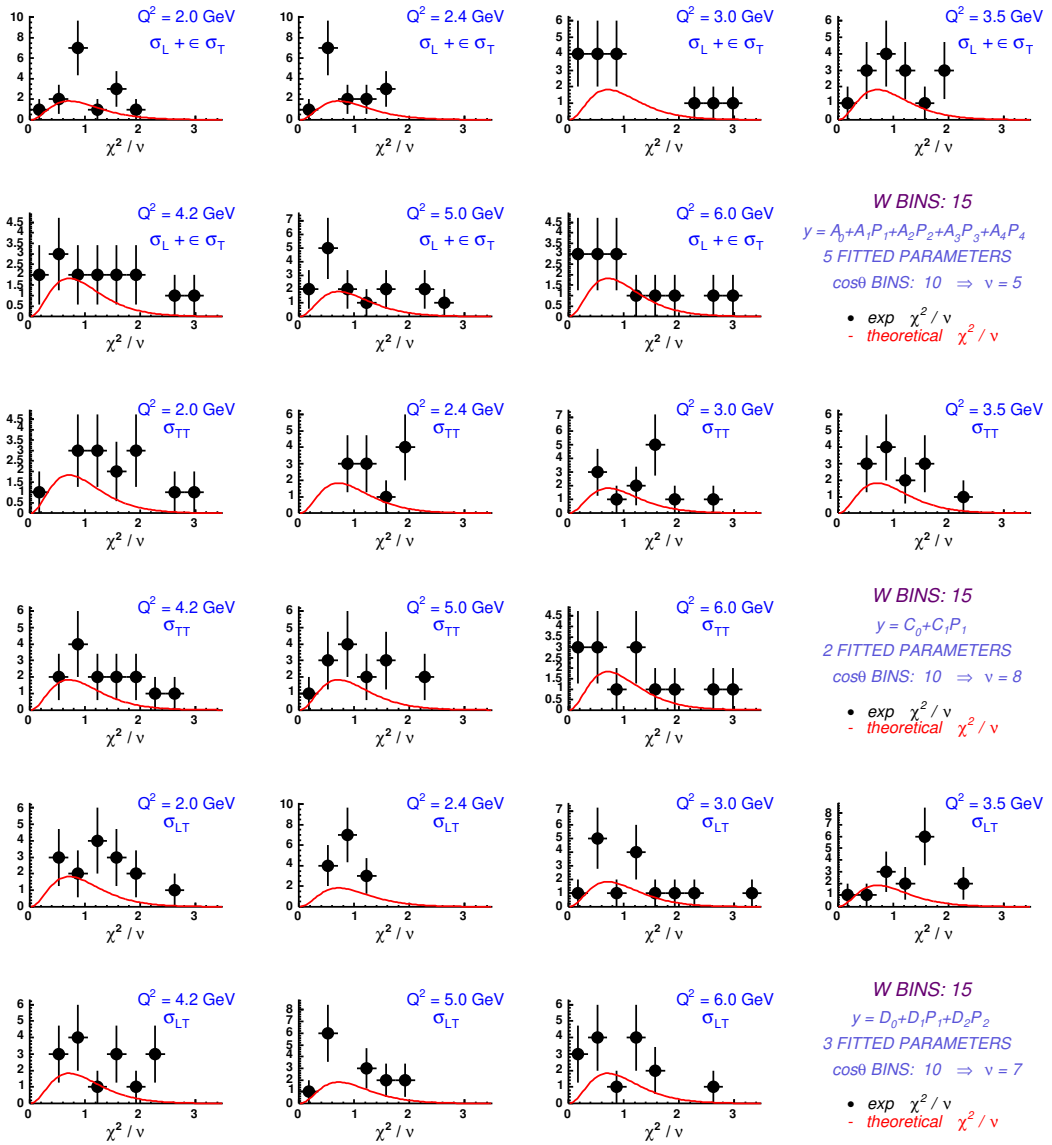


Figure 3.12: Reduced χ^2 distribution of the Legendre fits. The $\sigma_L + \epsilon \sigma_T$, σ_{TT} and σ_{LT} have respectively 5, 8, and 7 degrees of freedom. Each plot has only 15 points (there are 15 W bins) so the statistic of the χ^2/ν distributions is poor. The red line is the expected χ^2 distribution.

Figure 3.13 shows the coefficients of the Legendre expansion for $Q^2 = 2.4 \text{ GeV}^2$. The coefficient A_0 , proportional to M_{1+} if $\sigma_L \ll \sigma_T$ (see Eqn 3.9) and to the total c.m. cross section, shows the characteristic resonance behaviour at the peak of the Δ .

$$\sigma_{t\bar{t}} = A_0 + A_1 P_1(\cos\theta) + A_2 P_2(\cos\theta) + A_3 P_3(\cos\theta) + A_4 P_4(\cos\theta)$$

$$\sigma_{tt} = C_0 + C_1 P_1(\cos\theta)$$

$$\sigma_{lt} = D_0 + D_1 P_1(\cos\theta) + D_2 P_2(\cos\theta)$$

$$Q^2 = 2.4$$

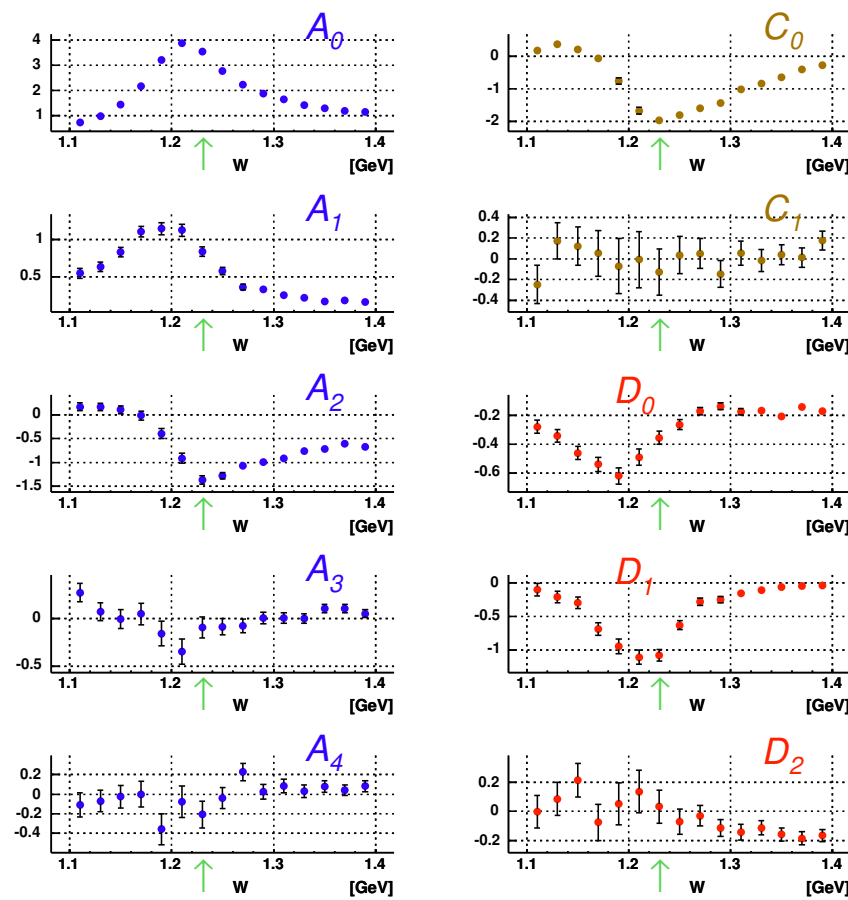


Figure 3.13: Legendre coefficients at $Q^2 = 2.4 \text{ GeV}^2$. The green arrow shows the Δ mass position. The coefficient A_0 is proportional to M_{1+} and to the total c.m. cross section.

See

<http://www.jlab.org/~ungaro/pi0eprod/coefficients>

for the plots of the various coefficients for different cuts used in the analysis.

3.6.2 The M_{1+} dominance assumption

The approximation made of ℓ up to d-waves is a good approximation: one can see from Figure 3.13 that A_4 , C_1 , D_2 are rather small around the Δ compared to their respective coefficients with smaller ℓ . In order to make a model independent extraction of the multipoles a further approximation is needed.

Previous measurements at lower Q^2 showed that E_{1+} and S_{1+} are relatively small compared to M_{1+} . All models that apply in this range of Q^2 show that M_{1+} is the multipole that has the greatest strength.

The M_{1+} dominance approximation consists in considering only the multipoles that interfere with M_{1+} . With this approximation the relation between the Legendre coefficients and the electromagnetic multipoles is [40]:

$$\begin{aligned} |M_{1+}|^2 &= A_0/2 \\ \text{Re}(E_{1+}M_{1+}^*) &= (A_2 - 2C_0/3)/8 \\ \text{Re}(S_{1+}M_{1+}^*) &= D_1/6 \\ \text{Re}(E_{0+}M_{1+}^*) &= A_1/2 \\ \text{Re}(S_{0+}M_{1+}^*) &= D_0 \\ \text{Re}(M_{1-}M_{1+}^*) &= -(A_2 + 2(A_0 + C_0))/8 \end{aligned} \tag{3.9}$$

To obtain the various multipole ratios \mathfrak{R}_m at the resonance peak, a Taylor expansion distribution around $M_W = 1.232 \text{ GeV}$ is performed, as shown in Figure 3.14 Figure 3.15:

$$\mathfrak{R}_m(W) \sim a_0 + a_1(x - M_W) + a_2(x - M_W)^2 + \dots = \sum_i a_i(x - M_W)^i$$

with this expansion, at the Δ peak we have $\mathfrak{R}_m = a_0$.

To see all the multipoles and multipoles ratios plots see

<http://www.jlab.org/~ungaro/pi0eprod/multipoles>

3.6.3 Effect of M_{1+} dominance and $\ell \leq 2$ approximation

The M_{1+} dominance assumption and the limited order ($\ell \leq 2$) in the Legendre expansion of the structure functions introduce an uncertainty in the extraction of the multipoles which is expected to become greater with increasing Q^2 .

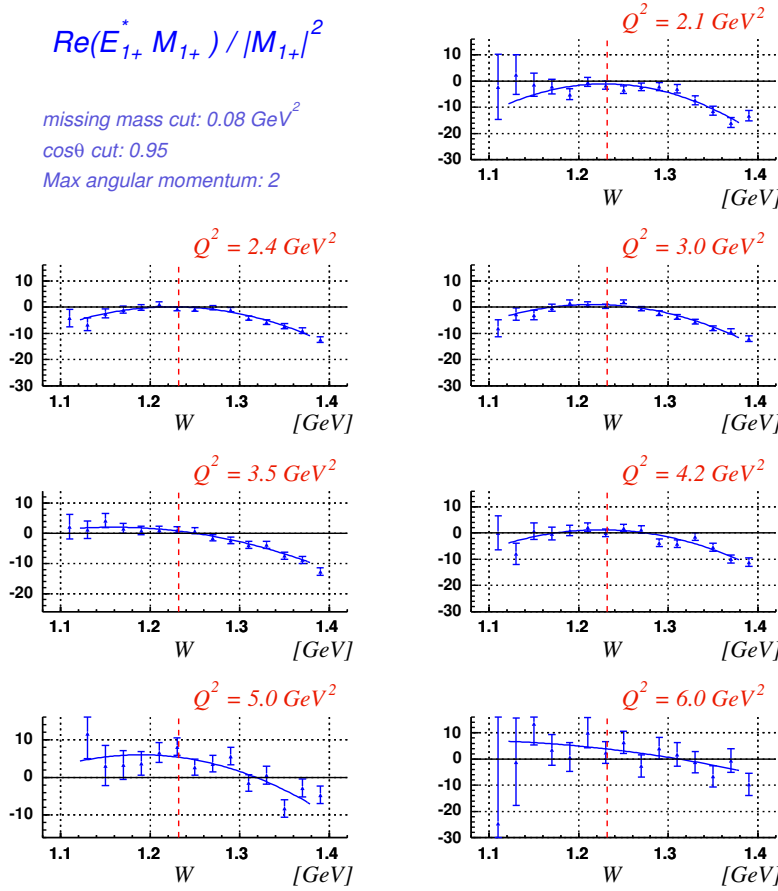


Figure 3.14: $Re(E_{1+}^* M_{1+})$ as a function of W for different Q^2 . The value at the Δ peak is the a_0 coefficient of the Taylor expansion around $M_W = 1.232$

In order to evaluate such uncertainty two models (MAID, DMT) were used to generate the cross sections σ_{MAID} and σ_{DMT} . These models provide the multipoles $E_{\ell\pm}$, $S_{\ell\pm}$, $M_{\ell\pm}$ with ℓ up to 5.

The generated cross section were fitted as described in Section 3.5 to extract the structure functions. The structure functions were fitted with orthogonal Legendre polynomials with ℓ up to d-waves as in Section 3.6.1. The approximation (3.9) was used in order to extract the multipoles.

Figure 3.16 and Figure 3.17 show the model and extracted multipole ratios for $Q^2 = 3.5 \text{ GeV}^2$.

One can see that in the Δ region DMT prescribes a smaller value of S_{1+} than MAID. The differences become even larger at higher Q^2 . E_{1+} remains negative and constant for MAID while it becomes positive in DMT between Q^2 of 3 and 4 GeV^2 .

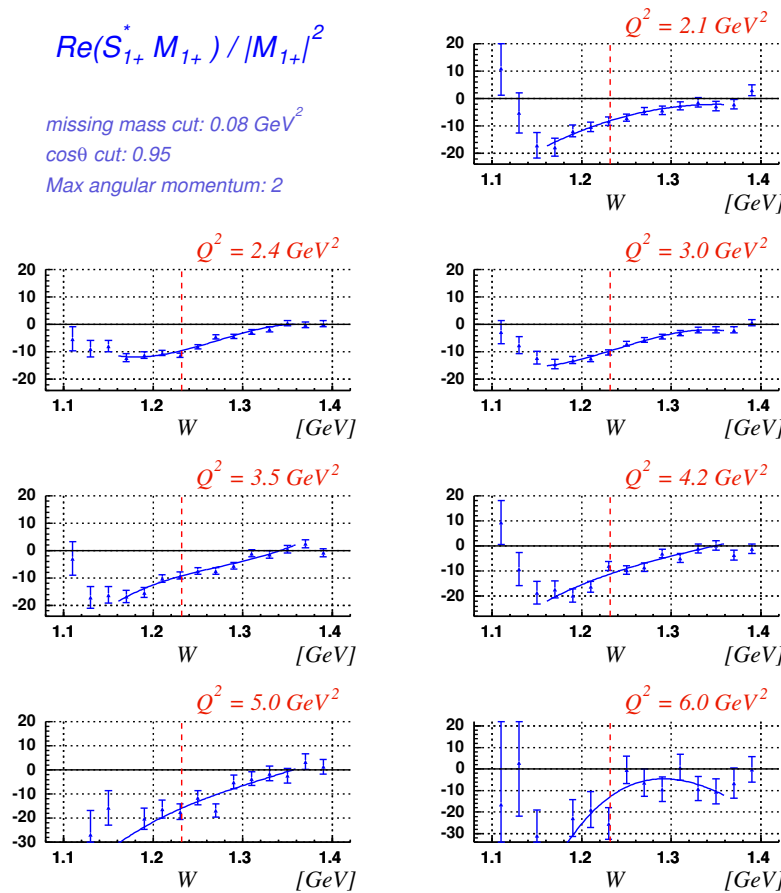


Figure 3.15: $Re(S_{1+}^* M_{1+})$ as a function of W for different Q^2 . The value at the Δ peak is the a_0 coefficient of the Taylor expansion around $M_W = 1.232$

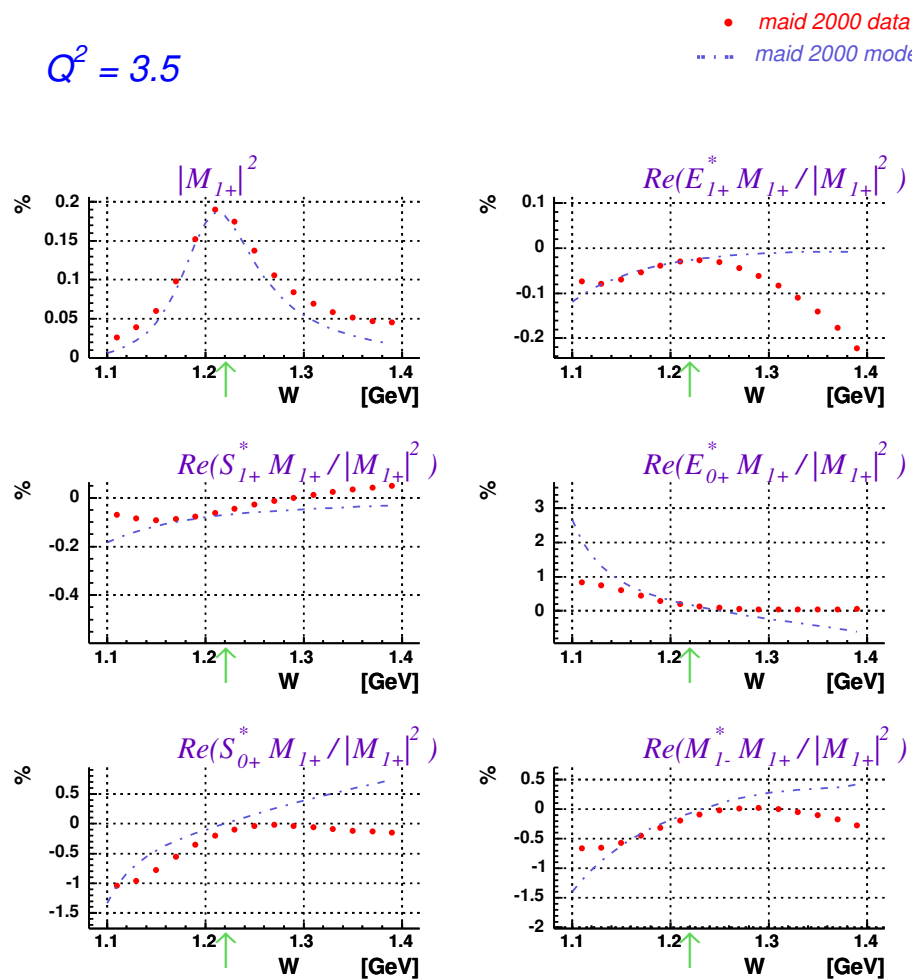


Figure 3.16: Comparison between the model and extracted multipole ratios for MAID 2000 at $Q^2 = 3.5 \text{ GeV}^2$.

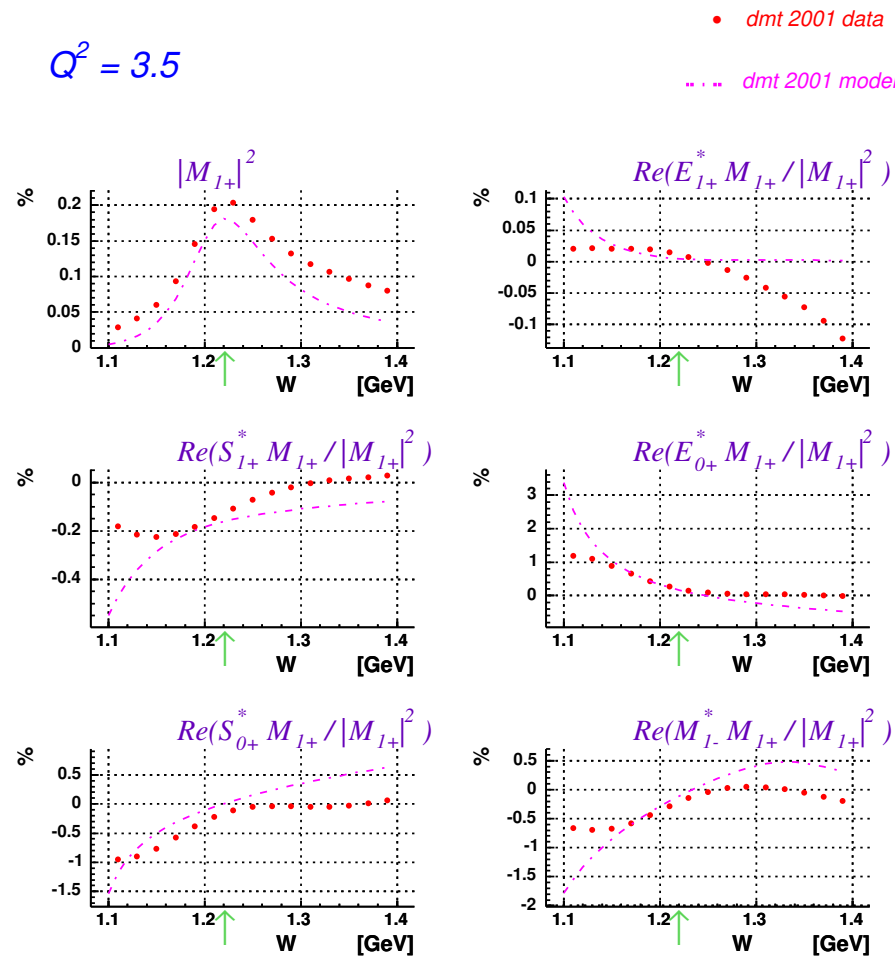


Figure 3.17: Comparison between the model and extracted multipole ratios for DMT 2001 at $Q^2 = 3.5 \text{ GeV}^2$.

The difference between the extracted multipole with the model prediction at the Δ peak is illustrated in Figure 3.18 for E_{1+}/M_{1+} and in Figure 3.19 for S_{1+}/M_{1+} .

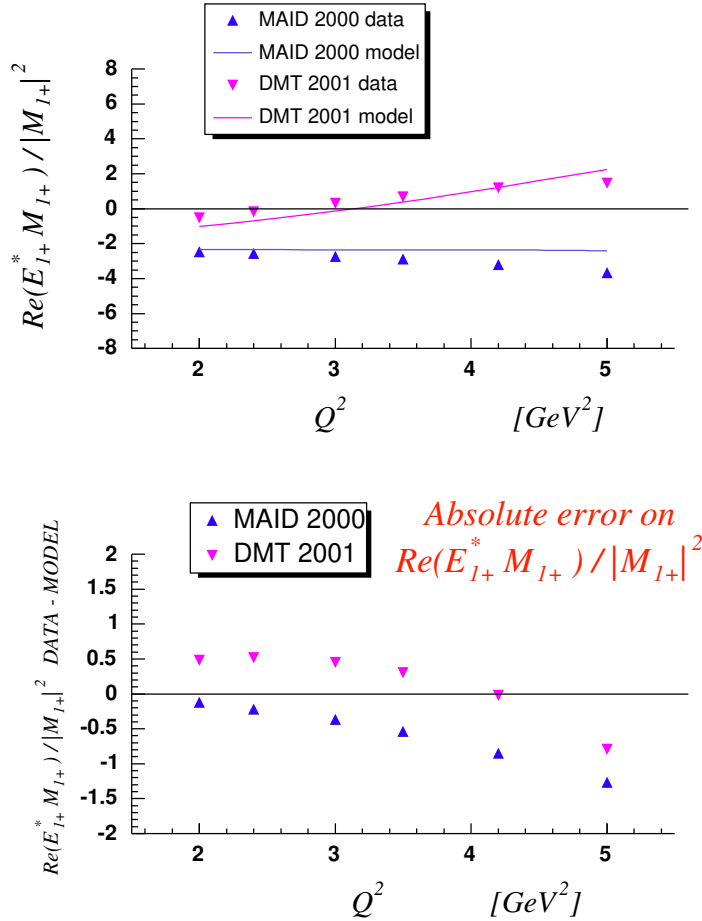


Figure 3.18: Model and M_{1+} dominance extracted E_{1+}/M_{1+} as a function of Q^2 . Top: the points are the value from the fit and the approximations described in the text. The lines are the model prediction. Bottom: absolute difference between between extracted value and model prediction.

When MAID is used the ratio E_{1+}/M_{1+} is always underestimated, starting at $\sim 0.2\%$ at $Q^2 = 2 \text{ GeV}^2$ and up to $\sim 1.2\%$ at $Q^2 = 5 \text{ GeV}^2$. When DMT is used a rather constant overestimation by $\sim 0.5\%$ of E_{1+}/M_{1+} up to $Q^2 = 3.5 \text{ GeV}^2$ is obtained. At $Q^2 = 4.2$ the value extracted is the same as in the model but at $Q^2 = 5$ E_{1+}/M_{1+} is underestimated by $\sim 0.8\%$.

As regarding S_{1+}/M_{1+} , the extraction from both models yields a rather significant

overestimation increasing in value with Q^2 .

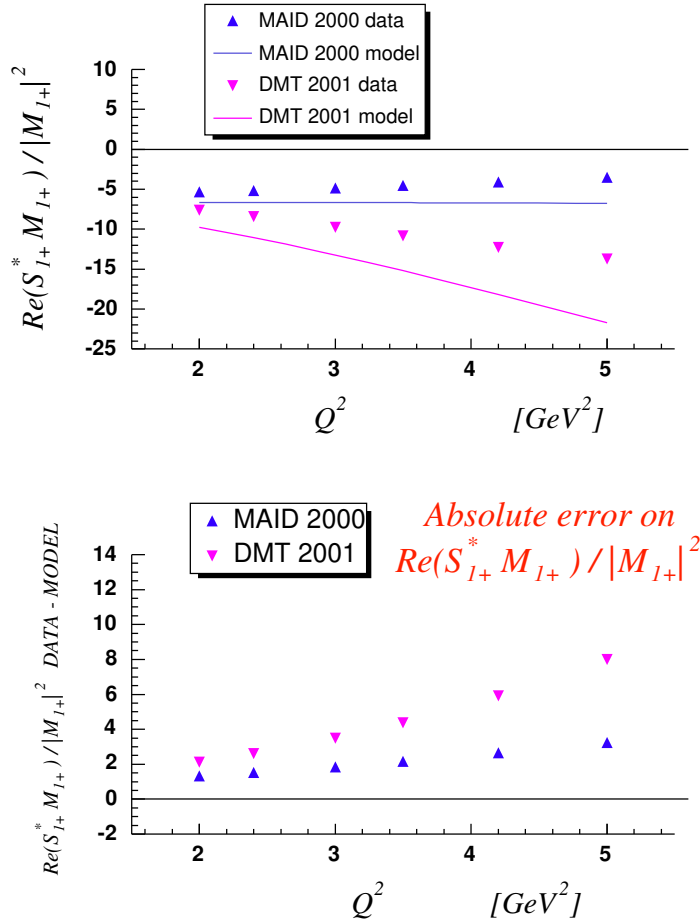


Figure 3.19: Model and M_{1+} dominance extracted S_{1+}/M_{1+} as a function of Q^2 . Top: the points are the value from the fit and the approximations described in the text. The lines are the model prediction. Bottom: absolute difference between between extracted value and model prediction.

3.6.4 Multipole Truncation Results for R_{EM} and R_{SM}

The result for the ratios R_{EM} and R_{SM} are shown in Table 3.2 for different values of Q^2 .

The fits suggest a zero crossing for R_{EM} between Q^2 of 3.0 and 4.0 GeV 2 .

Q^2 (GeV 2)	R_{EM} (%), E_{STAT}, E_{SYS})	R_{SM} (%), E_{STAT}, E_{SYS})
2.15	$-1.0 \pm 0.7 \pm 0.05$	$-10.0 \pm 0.9 \pm 0.06$
2.4	$0.4 \pm 0.3 \pm 0.2$	$-11.7 \pm 0.5 \pm 0.2$
3	$1.3 \pm 0.4 \pm 0.3$	$-12.5 \pm 0.5 \pm 0.07$
3.5	$1.2 \pm 0.5 \pm 0.3$	$-12.9 \pm 0.7 \pm 0.2$
4.2	$1.7 \pm 0.6 \pm 0.4$	$-17.3 \pm 1.0 \pm 0.14$
5	$6.0 \pm 1.0 \pm 0.5$	$-24.0 \pm 1.8 \pm 0.24$
6	$4.8 \pm 1.8 \pm 0.7$	$-24.0 \pm 4 \pm 0.4$

Table 3.2: Results for R_{EM} and R_{SM} in the multipole truncation analysis.

R_{EM} is shown in Figure 3.20 along with the prediction from DMT 2001 and MAID 2000 models. Previous data from CLAS and Hall C (using M_{1+} dominance and $\ell \leq 1$ approximations) are also plotted.

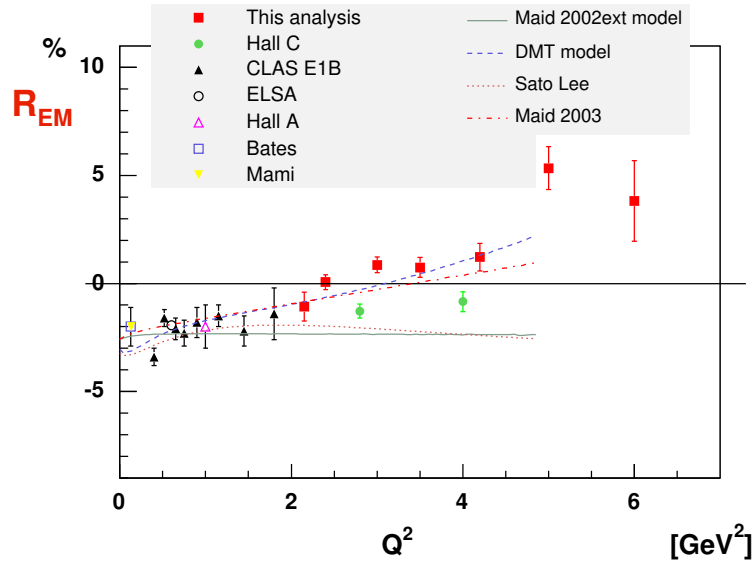


Figure 3.20: Result for R_{EM} as a function of Q^2 obtained in the M_{1+} dominance approximation.

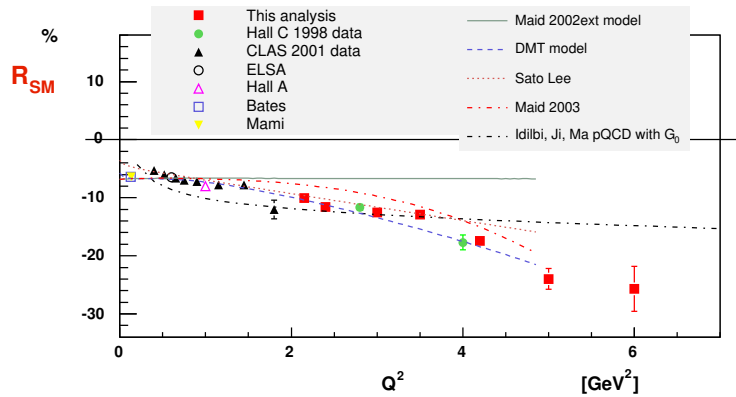


Figure 3.21: Result for R_{SM} as a function of Q^2 obtained in the M_{1+} dominance approximation.

3.6.5 Amplitudes of M_{1-} , E_{0+} , S_{0+}

Equations (3.9) holds if $|M_{1+}| \gg |M_{\ell\pm}|$ where $M_{\ell\pm}$ is any e.m. multipole that can contribute to the process. The extraction of M_{1-} , E_{0+} and S_{0+} using (3.9) is a consistency check of the M_{1+} dominance assumption. In Figure 3.22 and Figure 3.23 it is shown the result of the ratios $\text{Re}(M_{1-}^* M_{1+}) / |M_{1+}|^2$, $\text{Re}(E_{0+}^* M_{1+}) / |M_{1+}|^2$ and $\text{Re}(S_{0+}^* M_{1+}) / |M_{1+}|^2$. These amplitudes are about $10 - 20\%$ of in $|M_{1+}|$ amplitude, increasing with Q^2 . This rather large result suggest that Equations (3.9) are only approximate.

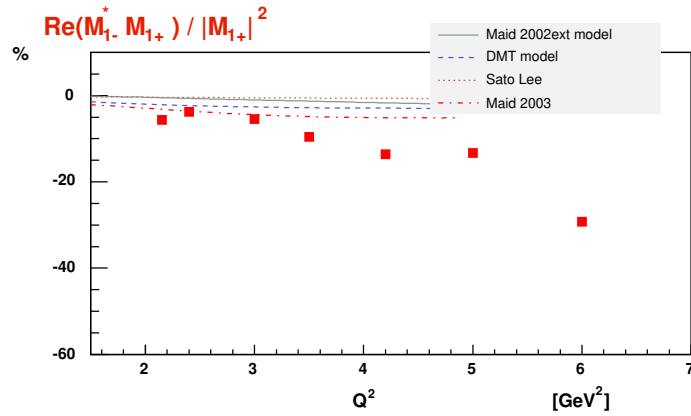


Figure 3.22: Result for M_{1-} as a function of Q^2 obtained in the M_{1+} dominance approximation.

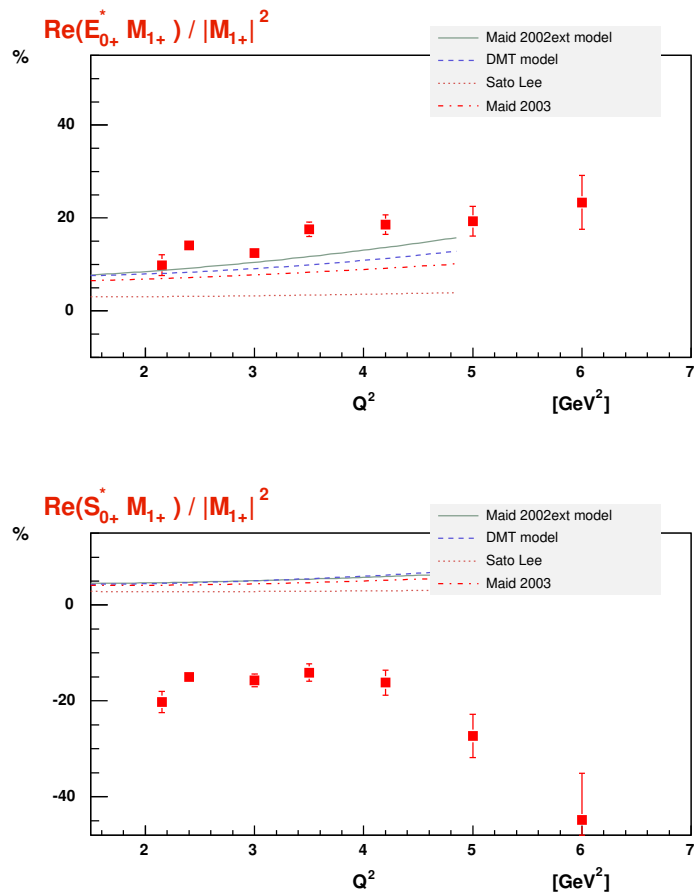


Figure 3.23: Result for E_{0+} and S_{0+} as a function of Q^2 obtained in the M_{1+} dominance approximation.

3.7 The JANR fit

The JANR model [4], [5] incorporates the unitary isobar approach [17] modified in order to include the Regge poles. The resonances contribute as Breit-Wigner, while non resonant background is built from the Born terms and the t -channel ρ and ω contributions. To calculate the Born terms the latest calculation of the nucleon and pion form factors was used.

The parameters obtained by fitting the cross section data are the magnitudes of the multipoles corresponding to the resonance from the first and second resonance regions at the resonance positions. After extracting the multipoles, the JANR program can recalculate the cross section. An example of this process is illustrated in Figure 3.24 where both the data (blue triangles) and the JANR cross section (solid black line) are plotted. The JANR global fit well reproduces the experimental data behaviour.

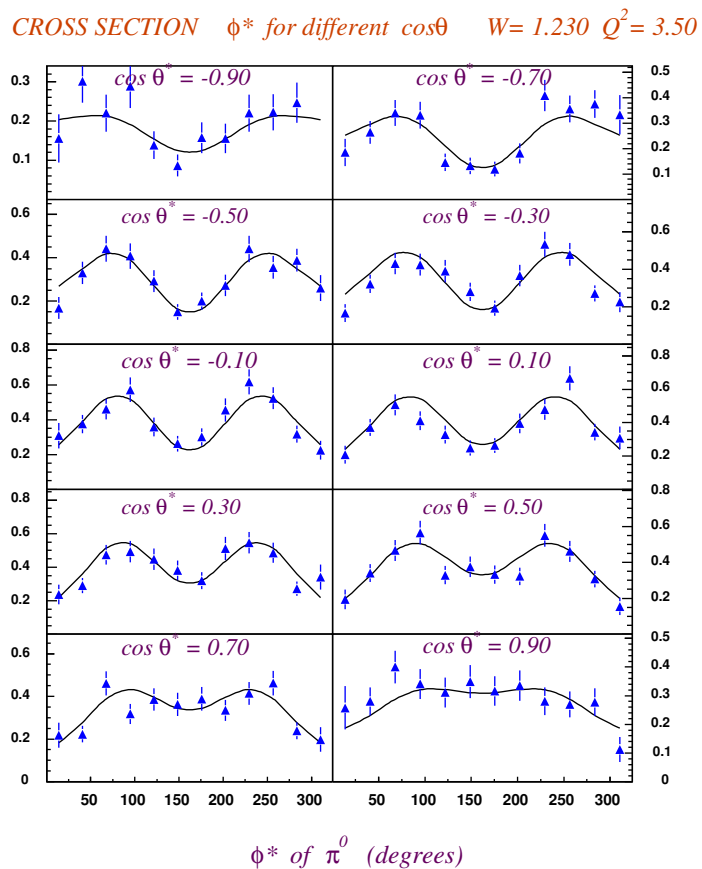


Figure 3.24: JANR fit of the cross section. The blue triangles represent the experimental data points. The solid black line is the JANR calculated cross section after the fit.

To further investigate the JANR fit result, the JANR obtained cross section was fitted with Legendre polynomials as described in 3.5, and the structure functions were extracted. An example is shown in Figure 3.25, Figure 3.26 and Figure 3.27, where $\sigma_T + \epsilon_L \sigma_L$, σ_{LT} and σ_{TT} are shown respectively.

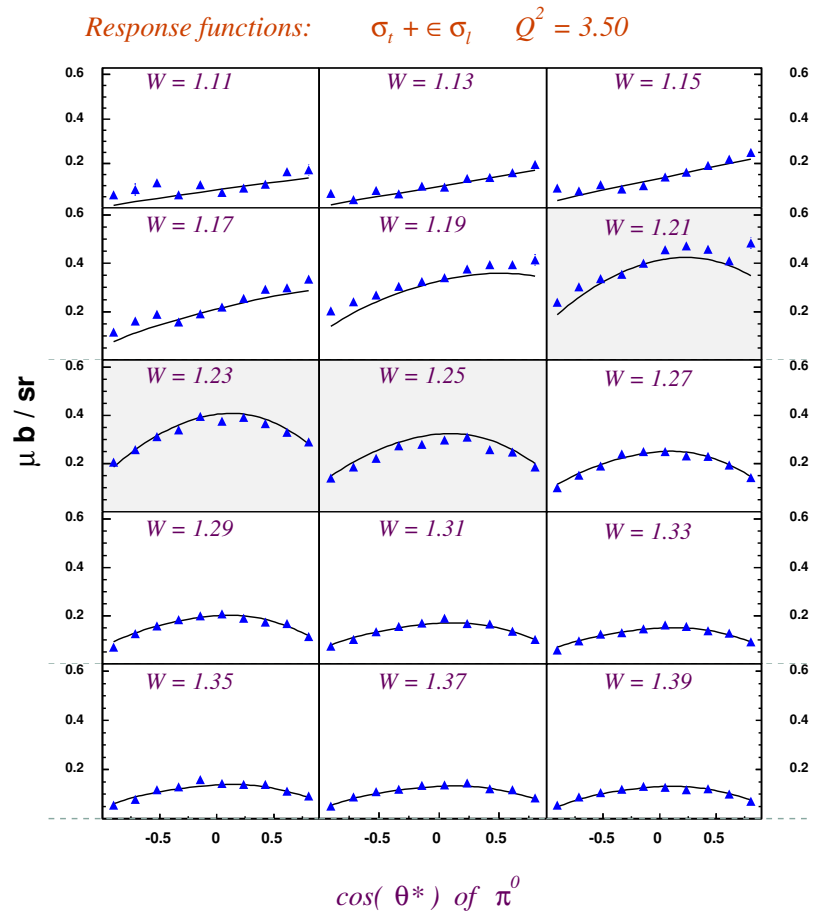


Figure 3.25: JANR fit and $\sigma_T + \epsilon_L \sigma_L$. The blue triangles represent the experimental data points. The solid black line is the JANR calculated cross section after the JANR fit.

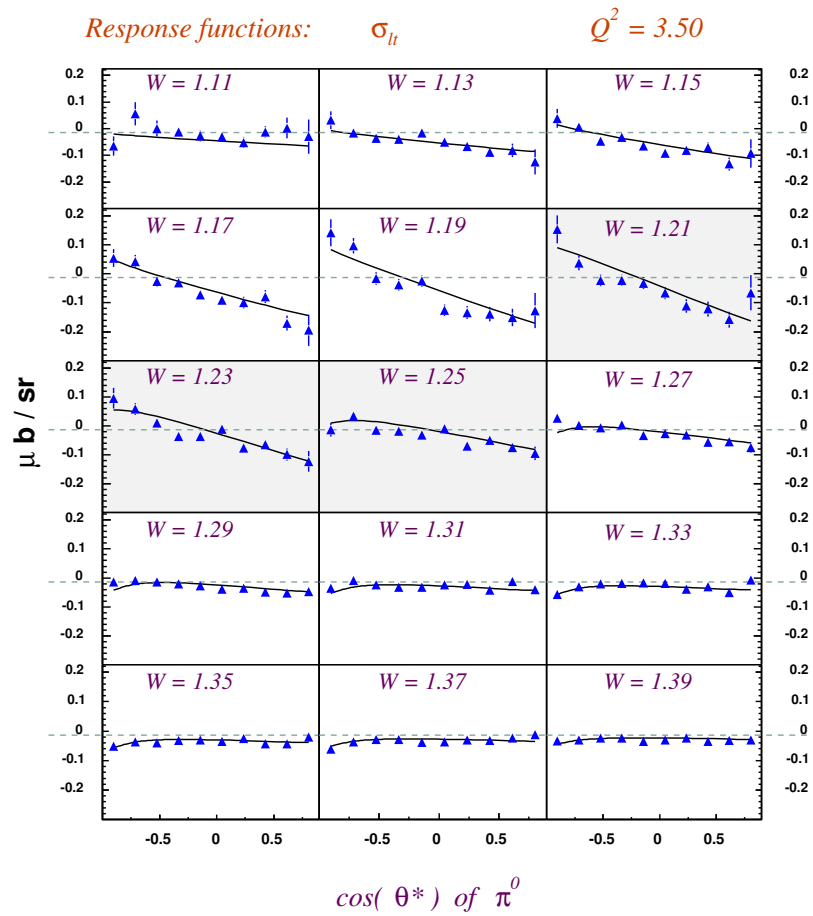


Figure 3.26: JANR fit and σ_{LT} . The blue triangles represent the experimental data points. The solid black line is the JANR calculated cross section after the JANR fit.

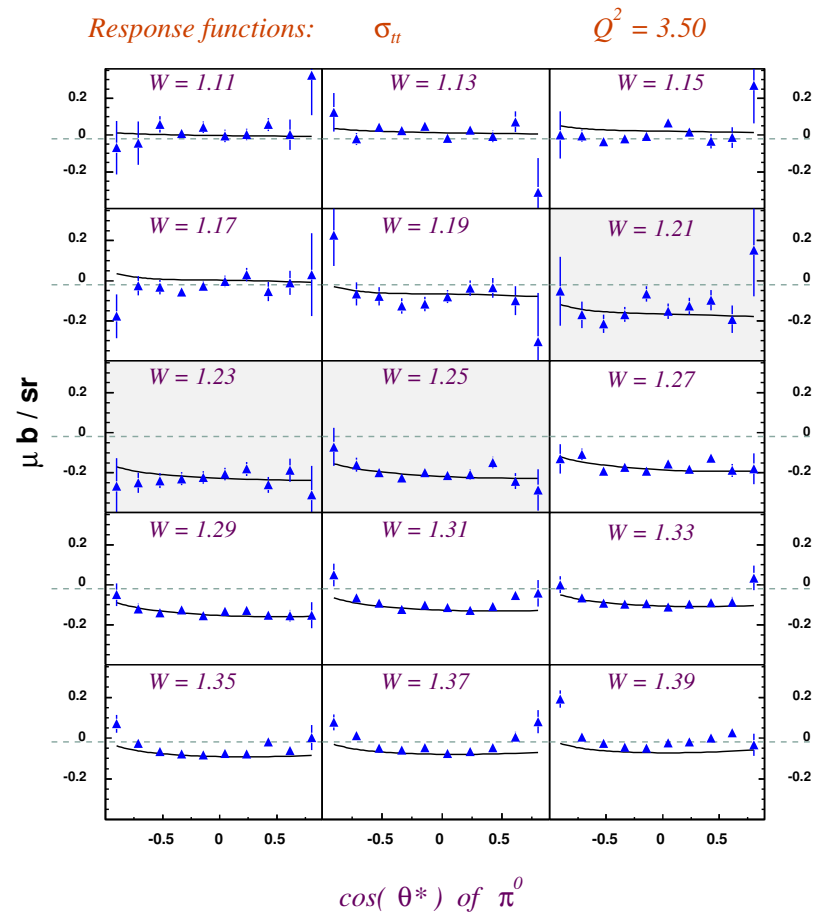


Figure 3.27: JANR fit and σ_{TT} . The blue triangles represent the experimental data points. The solid black line is the JANR calculated cross section after the JANR fit.

3.7.1 JANR Results for R_{EM} and R_{SM}

In Figure 3.28 and Figure 3.29 the results for R_{EM} and R_{SM} of the JANR fit is shown. While R_{SM} is consistent with the multipole truncation result, R_{EM} presents significantly lower values. To investigate this discrepancy, the JANR obtained cross section was analyzed using the multipole truncation method. The result for R_{EM} is shown in Figure 3.30, where one can see that the multipole truncation introduce a systematic shift on R_{EM} , increasing in value with Q^2 . The result in Figure 3.30 is somewhat consistent with the multipole truncated analysis fit of the experimental data shown in Figure 3.20.

When comparing the JANR fit of this data with the previous Hall-C data, a significantly smaller value for the M_{1-} amplitude is found. See Sec. 3.8

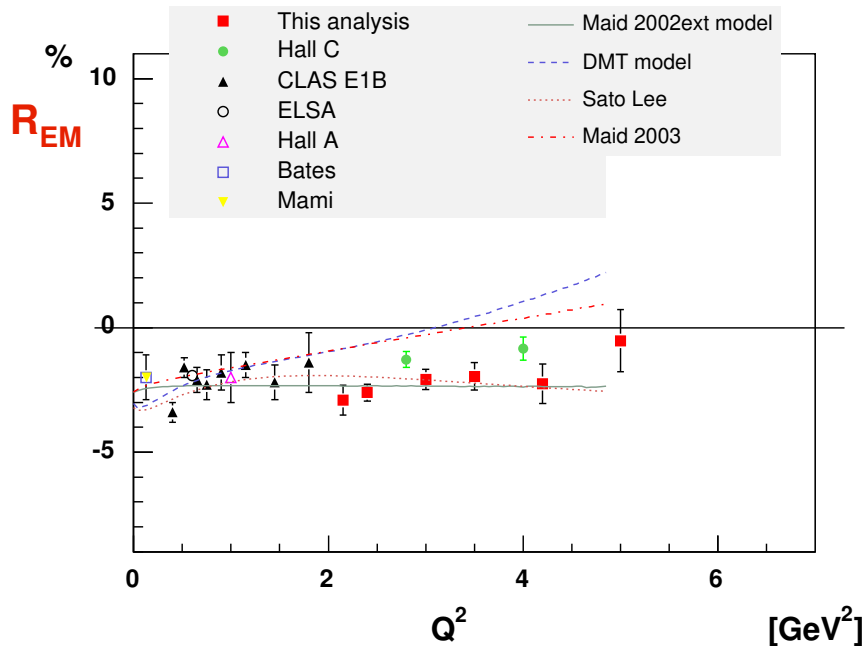


Figure 3.28: Result for R_{EM} as a function of Q^2 obtained with JANR.

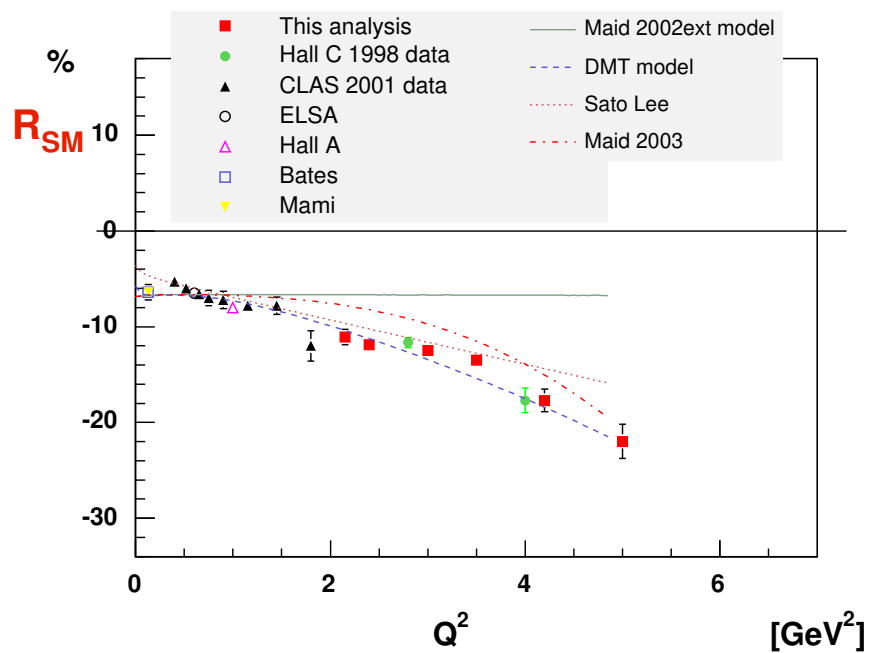


Figure 3.29: Result for R_{SM} as a function of Q^2 obtained with JANR.

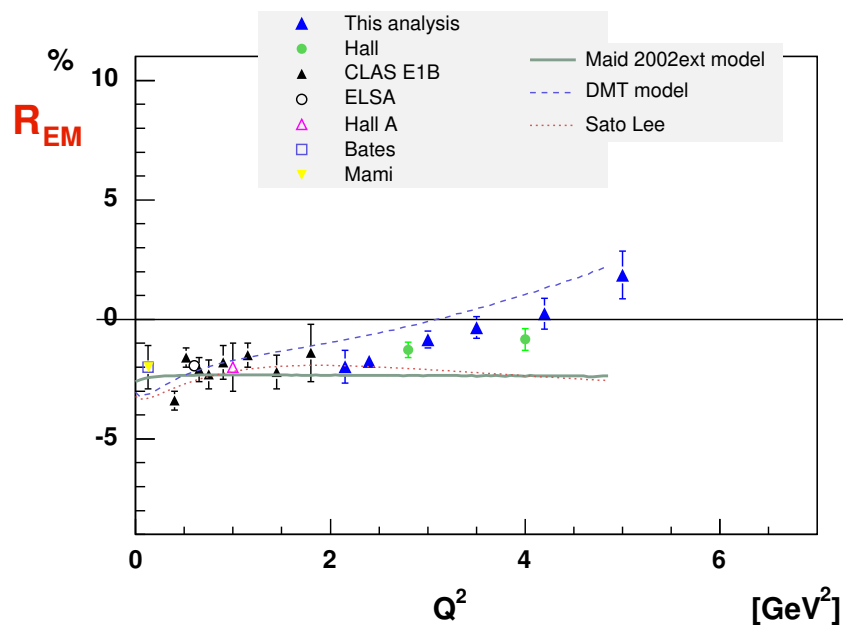


Figure 3.30: Result for R_{EM} as a function of Q^2 obtained applying the multipole truncation method to the JANR obtained cross section. Compare this plot with Figure 3.28 to see how much the result changes with the fit method used. Compare this plot with Figure 3.20 to see the multipole truncation fit to the real data.

3.8 Different models and the P_{11} signal

The data has been compared with the models *maid2000*, *maid2002ext*, *maid2003* [17]¹ *DMT2001* [26]. When using the maid2003 model, the cross section has been calculated with or without the P_{11} resonance. The data has also been compared with the cross section calculated by JANR as a result of the fit to this data as a check for consistency. All the cross sections, response functions, coefficient, multipoles distributions can be found on the web at, respectively:

```
http://www.jlab.org/~ungaro/pi0eprod/cro\_plots
http://www.jlab.org/~ungaro/pi0eprod/responses
http://www.jlab.org/~ungaro/pi0eprod/coefficients
http://www.jlab.org/~ungaro/pi0eprod/multipoles
http://www.jlab.org/~ungaro/pi0eprod/results
```

by clicking the appropriate model check box at the top of the page.

Each model cross section has been fitted as described in Sec. 3.5 and the response functions have been expanded in Legendre polynomial. The coefficents of the expansion have been compared to the real data. Here we report the comparison of the A coefficients for the Legendre expansion of $\sigma_T + \epsilon_L \sigma_L$ at $Q^2 = 3.5 \text{ GeV}^2$ and $\ell \leq 2$.

The JANR fit is a good match to the data, as expected. The coefficient A_2 is directly linked to R_{EM} (see Eq. [3.9]). Maid 2002 consistently underestimates A_2 , while DMT matches the data at the Δ peak, but fails at higher W values. Good agreement is found for the Maid 2003 model.

When turning on and off the P_{11} resonance in the Maid 2003 model (see Figure 3.34 and Figure 3.35) one can see differences in the A_0 and A_1 coefficients. Without the Roper resonance Maid 2003 seems to better reproduce the data. These behaviour is seen at all Q^2 .

¹see also <http://www.kph.uni-mainz.de/MAID>

$$\sigma_T + \epsilon_L \sigma_L = A_0 + A_1 P_1(\cos\theta) + A_2 P_2(\cos\theta) + A_3 P_3(\cos\theta) + A_4 P_4(\cos\theta)$$

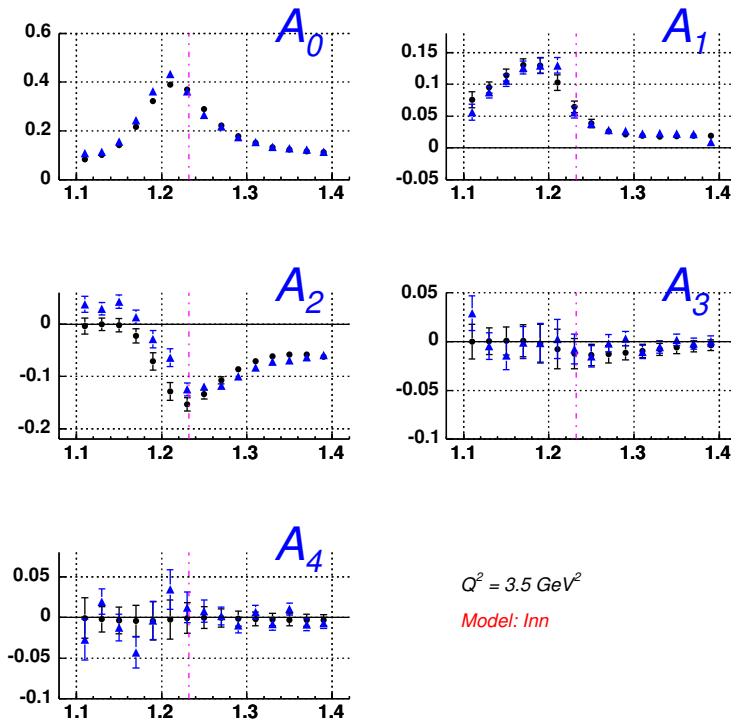


Figure 3.31: Coefficients of the Legendre expansion of $\sigma_T + \epsilon_L \sigma_L$ for the JANR generated cross section (black) and experimental data (blue)

$$\sigma_T + \epsilon \sigma_L = A_0 + A_1 P_1(\cos\theta) + A_2 P_2(\cos\theta) + A_3 P_3(\cos\theta) + A_4 P_4(\cos\theta)$$

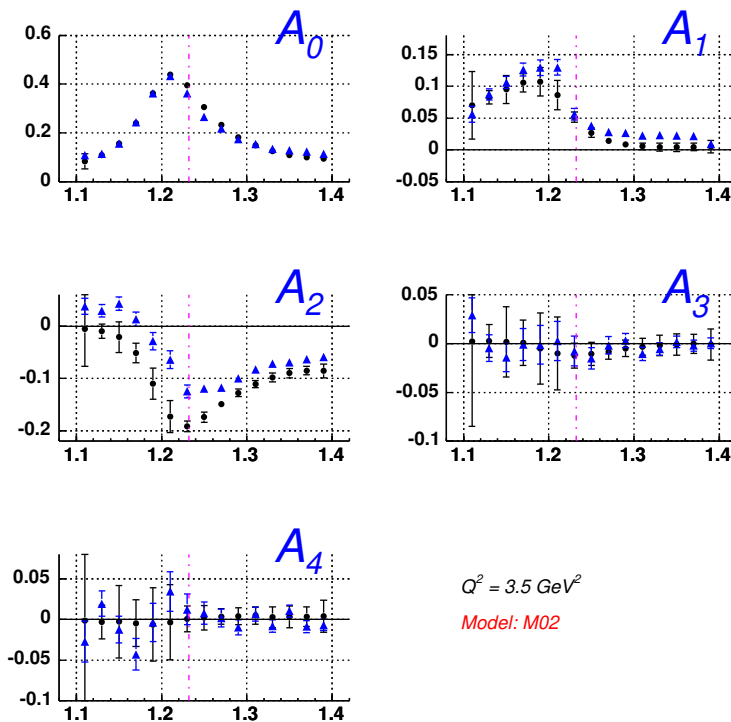


Figure 3.32: Coefficients of the Legendre expansion of $\sigma_T + \epsilon_L \sigma_L$ for the maid 2002 generated cross section (black) and experimental data (blue)

$$\sigma_T + \epsilon_L \sigma_L = A_0 + A_1 P_1(\cos\theta) + A_2 P_2(\cos\theta) + A_3 P_3(\cos\theta) + A_4 P_4(\cos\theta)$$

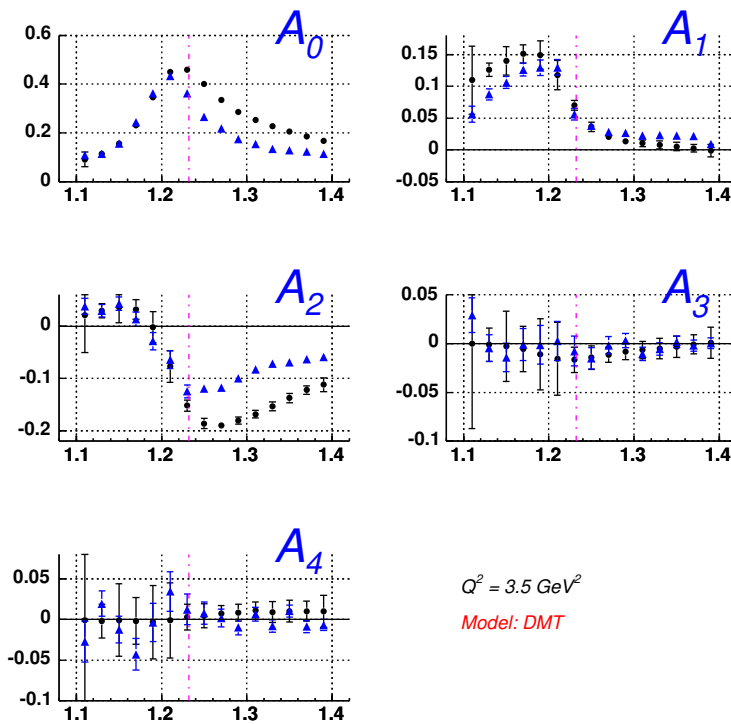


Figure 3.33: Coefficients of the Legendre expansion of $\sigma_T + \epsilon_L \sigma_L$ for the DMT generated cross section (black) and experimental data (blue)

$$\sigma_T + \epsilon \sigma_L = A_0 + A_1 P_1(\cos\theta) + A_2 P_2(\cos\theta) + A_3 P_3(\cos\theta) + A_4 P_4(\cos\theta)$$

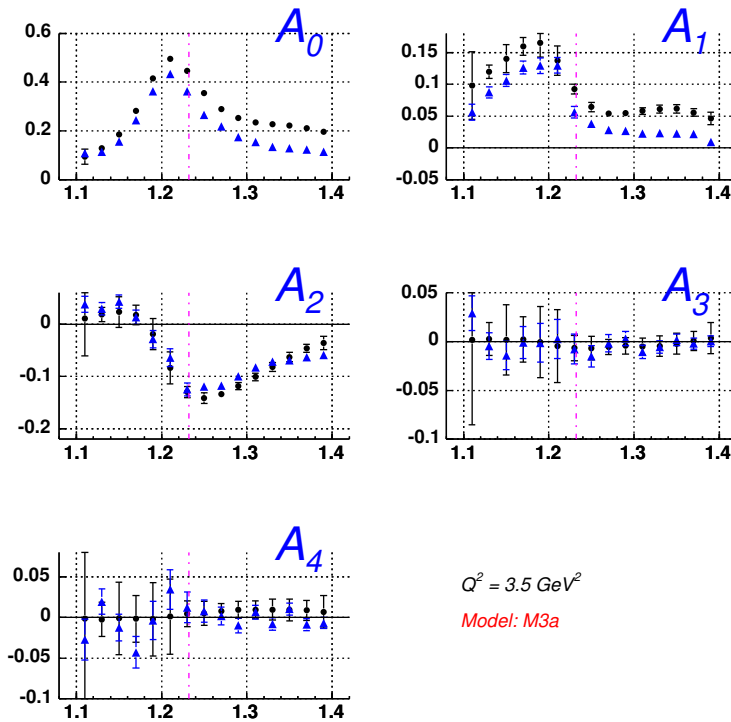


Figure 3.34: Coefficients of the Legendre expansion of $\sigma_T + \epsilon L \sigma_L$ for the maid 2003 with Roper on generated cross section (black) and experimental data (blue)

$$\sigma_T + \epsilon \sigma_L = A_0 + A_1 P_1(\cos\theta) + A_2 P_2(\cos\theta) + A_3 P_3(\cos\theta) + A_4 P_4(\cos\theta)$$

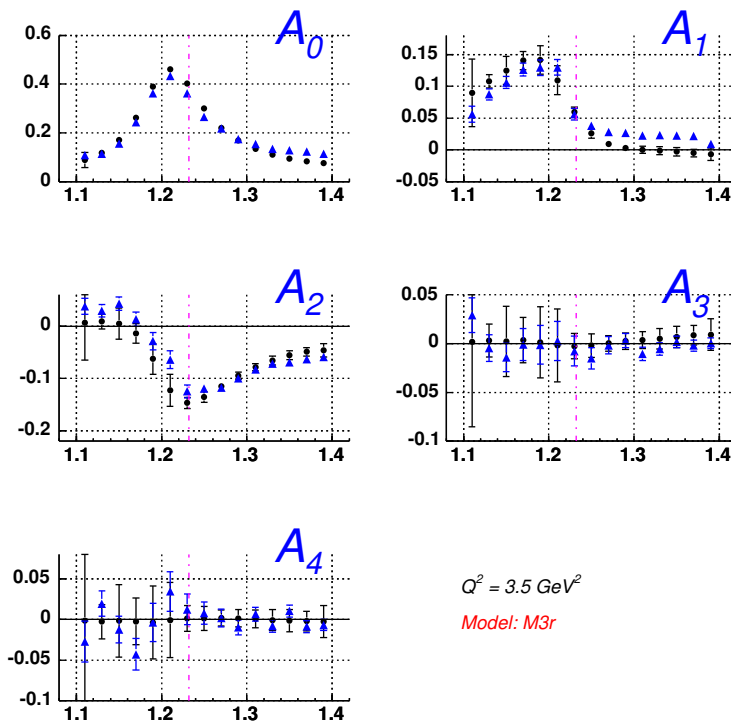


Figure 3.35: Coefficients of the Legendre expansion of $\sigma_T + \epsilon_L \sigma_L$ for the maid 2003 with Roper off generated cross section (black) and experimental data (blue)

3.9 Conclusions

The differential cross section for the π^0 electroproduction in the Δ resonance has been measured in the Q^2 range 2 to 6 GeV^2 and $1.1 \leq W \leq 1.4 \text{ GeV}$, with full coverage of the π^0 c.m. angles. The structure functions $\sigma_T + \epsilon_L \sigma_L$, σ_{LT} and σ_{TT} have been extracted using the ϕ^* dependance of the cross section.

Two calculations of the ratios R_{EM} and R_{SM} have been presented.

A multipoles truncation fit of the data has been performed using the M_{1+} dominance and $\ell \leq 2$ approximation. This extraction of the ratio R_{EM} suggest a zero crossing between Q^2 of 3 and 4.0 GeV^2 , while the ration R_{SM} is about -10% and decreases with Q^2 . This result for R_{EM} would prove that the helicity is not conserved in this range of momentum transferred. The validity of the M_{1+} dominance assumption is questionable, given the fact that the multipoles coming from background and other resonances reach values up to $20 - 40\%$ of $|M_{1+}|$.

A JANR fit that use the JLAB unitarian isobar model has been performed for Q^2 up to 5 GeV^2 . This extraction of the ratio R_{EM} shows a constant negative value of around -2.5% with the point at 5 GeV^2 consistent with zero. The JANR fit suggest a smaller M_{1-} amplitude when compared with the previous Hall-C data, suggesting that the P_{11} signal is not as strong.

CHAPTER 4

Systematic Errors Study

4.1 Calculation of the c.m. angle θ^*

The π^0 c.m. angle θ^* can be calculated in two ways:

- 1) **Lorentz method:** using the four vectors of the final electron and proton, one can calculate the c.m. four vectors with a lorentz transformation from the lab to the c.m.
- 2) **boost method:** assuming the reaction is a $\Delta \rightarrow \pi^0 P$, one can calculate the momentum of the proton in the C.M frame using just the electron four vector and kinematics.

Previous analysis of lower energy data showed that the systematic on the proton reconstruction favors method 2), as it is independent of the proton detection. However this method is also more affected by radiation of the electron. Monte Carlo studies below show that the Lorentz method gives better results.

4.1.1 The Lorentz Method

As described in Appendix A, H_μ is the outgoing hadrons mass four vector $H_\mu = q_\mu + P_\mu$ ($W = \sqrt{H_\mu H^\mu}$), where $q_\mu = e_\mu - e'_\mu$ (all quantities in the lab). The π^0 lab four vector is $x_\mu = H_\mu - P'_\mu$.

In Figure 4.1 is illustrated the definition of the angles ϕ^* and θ^* . To obtain x_μ^{CM} we can rotate the lab frame in order to overlap the $z-axis$ with the \vec{q} direction, then perform a $\beta = (t, x, y, z) = (0, 0, 0, |\vec{H}|/H_0)$ lorentz boost $x'_\mu = \Lambda(\beta)_\mu^\nu x_\nu$ where

$$\Lambda(\beta)_\mu^\nu = \begin{pmatrix} \gamma & 0 & 0 & -\beta\gamma \\ 0 & 1 & 0 & 0 \\ 0 & 0 & 1 & 0 \\ -\beta\gamma & 0 & 0 & \gamma \end{pmatrix}$$

4.1.2 The Invariant Method

The calculation of θ^* with the invariant method is based on the identity $p_z = |\vec{p}| \cos \theta$. While p_z is calculated using the Lorentz method described above, $|\vec{p}|$ is derived using electron kinematics and the assumption of $\Delta \rightarrow p, \pi^0$ decay using the two body decay in the c.m. formula:

$$p = \frac{\sqrt{[W^2 - (m_p - m_{\pi^0})^2][(W^2 - (m_p + m_{\pi^0})^2]}}{2}$$

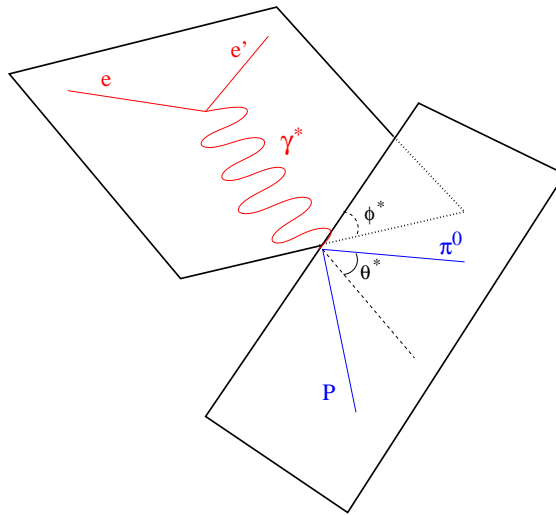


Figure 4.1: Schematics of π^0 electroproduction. The $z - axis$ is oriented along the beam line (incoming e) . On the right the definitions of the angles ϕ^* and θ^* .

4.1.3 Comparison

In order to study the above methodologies, a Monte Carlo simulation was used. Furthermore, the data were fitted using both methods.

An example of the simulation result is illustrated in Figure 4.2, where the $\cos \theta^*$ distribution is plotted for generated, "lorentz" and "invariant" events (meaning, events where $\cos \theta^*$ was calculated using the Lorentz and Invariant method respectively). The histos are normalized for a better comparison. When calculating the c.m. angle for the generated events, the original π^0 four vector was used, since it was kept in the datastream. For the Lorentz and Invariant case, the scattered electron and proton four vectors were used instead, as during the data analysis. Hereafter, the **Lorentz** method events will be plotted in blue, while the the **Invariant** method ones will be plotted in red.

Figure 4.2 a) shows the three methods for the generated events (before they are processed with GSIM). The differences between the distributions are due to the radiation of the electron arm (see Figure 3.5). In Figure 4.2 b) the same quantities are plotted after the fiducial cuts are applied (and still before GSIM). A slight distortion is seen. At forward angles, the Lorentz method is closer to the generated π^0 angle. In Figure 4.2 c) the distributions after GSIM and software reconstruction. Both at backward and forward angle, the Lorentz method is closer to the generated π^0 angle. The Invariant method shows some unphysical $\cos \theta^* > 1$ events. These are due to the smearing introduced by the CLAS detectors and reconstruction software and possibly to the rescattering of the proton in the torus coils. While the calculation of $|\vec{p}|$ is based on the assumption of $\Delta \rightarrow p, \pi^0$ decay and

uses only the electron kinematics, the calculus of p_z is not and this can lead to events where $p_z > |\vec{p}|$. In the Lorentz method, $\cos \theta^*$ is calculated from the four vector components of x_μ^{CM} so by definition its limits are $-1, 1$.

The events with $\cos \theta^* > 1$ for the invariant method are dealt in three ways, all included in the analysis: 1) They are rejected. 2) A cut at $\cos \theta^* < 1.05$ is introduced to recover the "smeared" events, but to still reject possible rescattering from the coils. In this case, the events with $1 < \cos \theta^* < 1.05$ are inserted in the last $\cos \theta^*$ bin. 3) They are all inserted in the last $\cos \theta^*$ bin. See App. C for the same plots at different Q^2 .

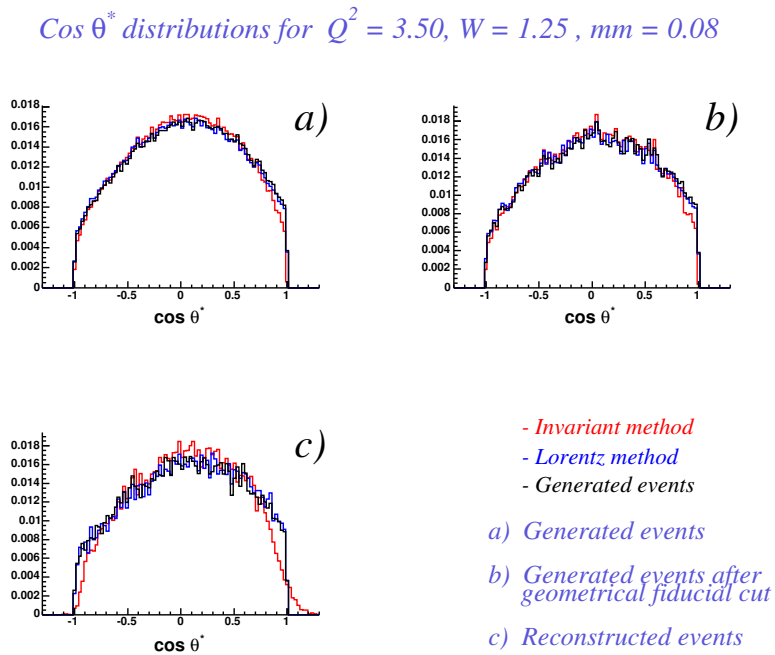


Figure 4.2: Generated, Lorentz and Invariant reconstructed $\cos\theta^*$ distribution for $Q^2 = 3.5 \text{ GeV}^2$. All histograms are normalized to 1.

In Figure 4.3 the acceptance is shown for the same (W, Q^2) bin of Figure 4.2. The differences peak at the $\cos \theta^*$ extremes. The c.m. differential cross section is shown in Figure 4.4. When performing the $a + b \cos \phi^* + c \cos 2\phi^*$ fit and extracting the structure functions, such small difference at extremes $\cos \theta^*$ play an important rule. The curvature of $\sigma_T + \epsilon \sigma_L$ at the Δ pole is most sensitive to the electric quadrupole amplitude E_{1+} . Differences of the $\sigma_T + \epsilon \sigma_L$ are illustrated in Figure 4.5. During the analysis, the structure functions were expanded in Legendre polynomials. The coefficients of the $\sigma_T + \epsilon \sigma_L$ expansions for the two methods are illustrated in Figure 4.5. The A_2 coefficient (which is basically the curvature of $\sigma_T + \epsilon \sigma_L$), differs by a factor of two. A non zero value of the A_3, A_4 coefficients would

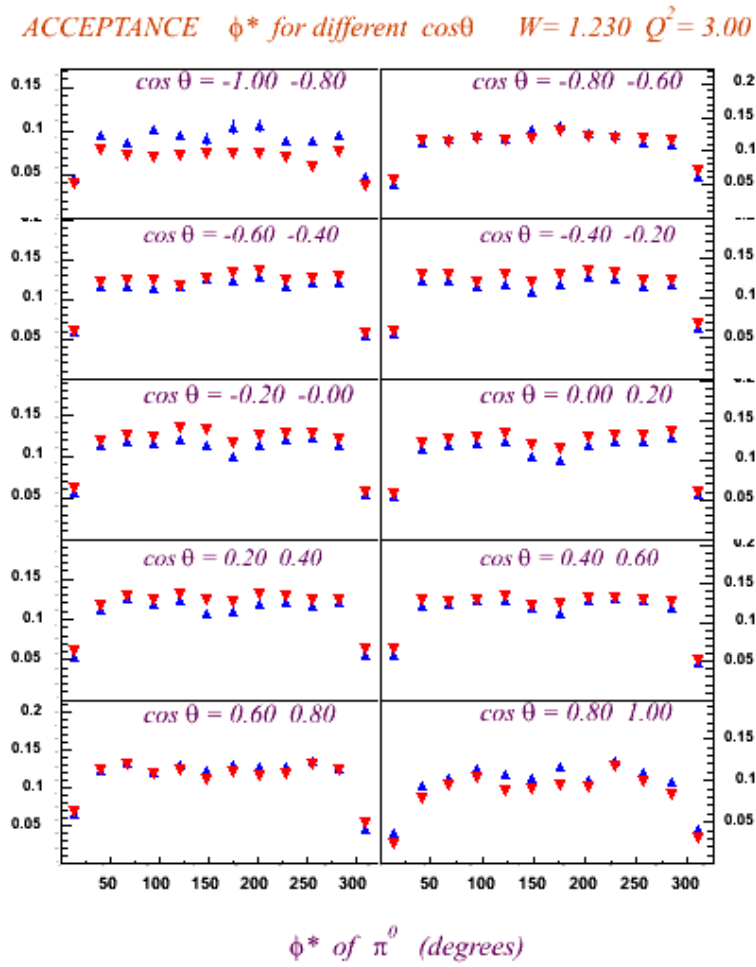


Figure 4.3: Acceptance for $W = 1.23$ GeV and $Q^2 = 3.0$ GeV 2 . Blue: Lorentz method. Red: Invariant method. The differences of the two methods are maximum at the extremes $\cos\theta^*$, especially at $\cos\theta^* = -0.9$

be the signal of $\ell > 1$ components of the (π^0, p) orbital angular momentum.

During the multipole truncation analysis, the M_{1+} dominance is assumed and the ratios E_{1+}/M_{1+} and S_{1+}/M_{1+} are calculated. Both the cases $\ell \leq 1$ and $\ell \leq 2$ are considered. An example of this extraction is shown in Figure 4.7.

4.1.4 Conclusions

The Lorentz method better reproduces the generated Monte Carlo π^0 c.m angle (see Figure 4.2 and App. C) The discrepancy in calculating the cross section is amplified during the analysis. The invariant method presents unlikely results for the orbital angular momentum of the (π^0, p) system and for the E_{1+}/M_{1+} ratio (based on continuity from previous measurements). For this reasons only the Lorentz method will be considered

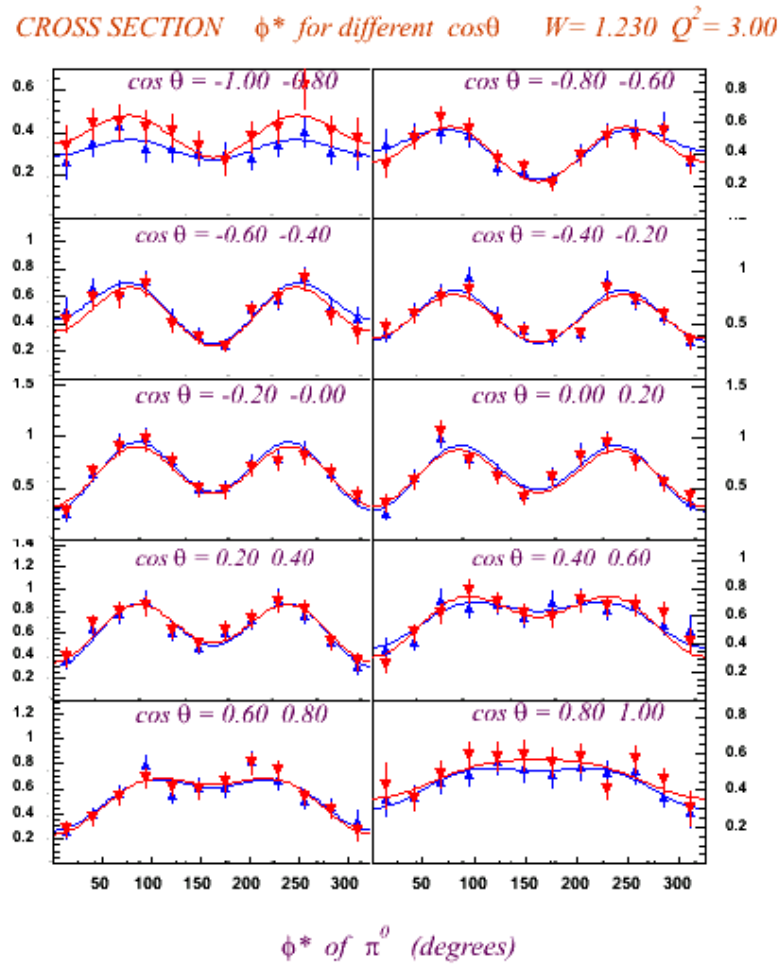


Figure 4.4: C.m. cross section for $W = 1.23$ GeV and $Q^2 = 3.0$ GeV 2 . Blue: Lorentz method. Red: Invariant method. the two methods are similar except at the $\cos\theta^*$ extremes.

in the analysis. Different cuts at the $\cos\theta^*$ extremes are performed and included in the systematic errors.

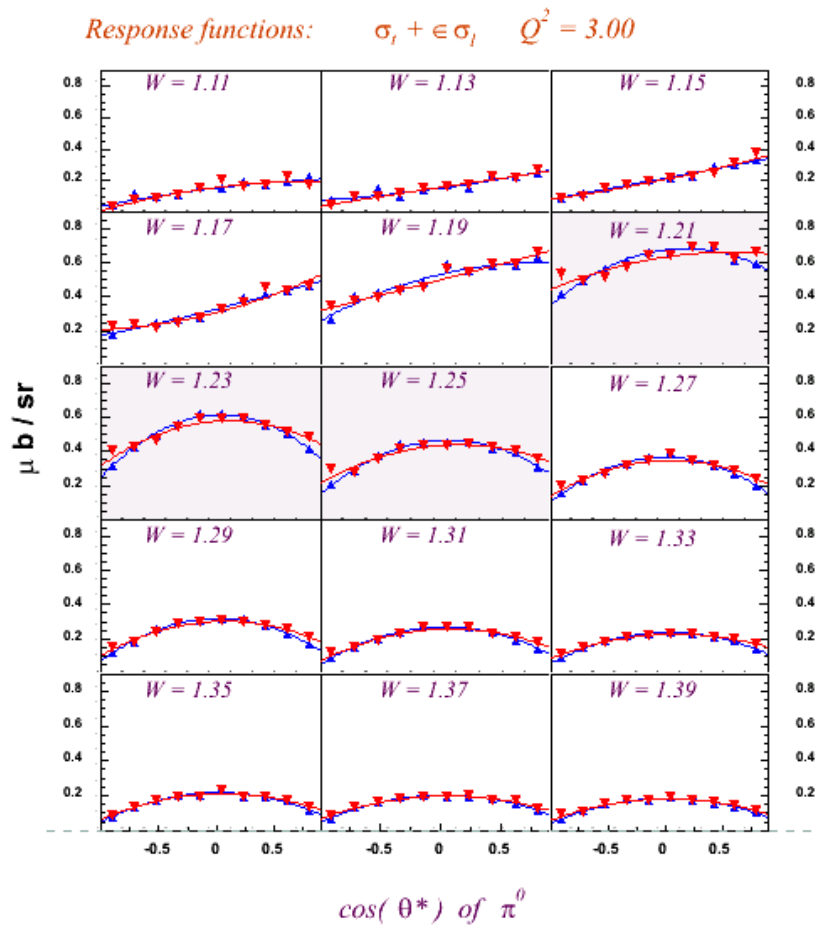


Figure 4.5: $\sigma_T + \epsilon \sigma_L$ for $Q^2 = 3.0 \text{ GeV}^2$. Blue: Lorentz method. Red: Invariant method. Note that the curvature of $\sigma_T + \epsilon \sigma_L$ at the Δ pole determines the amplitude of the electric quadrupole E_{1+} . See also Figure 4.6

$$\sigma_T + \epsilon \sigma_L = A_0 + A_1 P_1(\cos\theta) + A_2 P_2(\cos\theta) + A_3 P_3(\cos\theta) + A_4 P_4(\cos\theta)$$

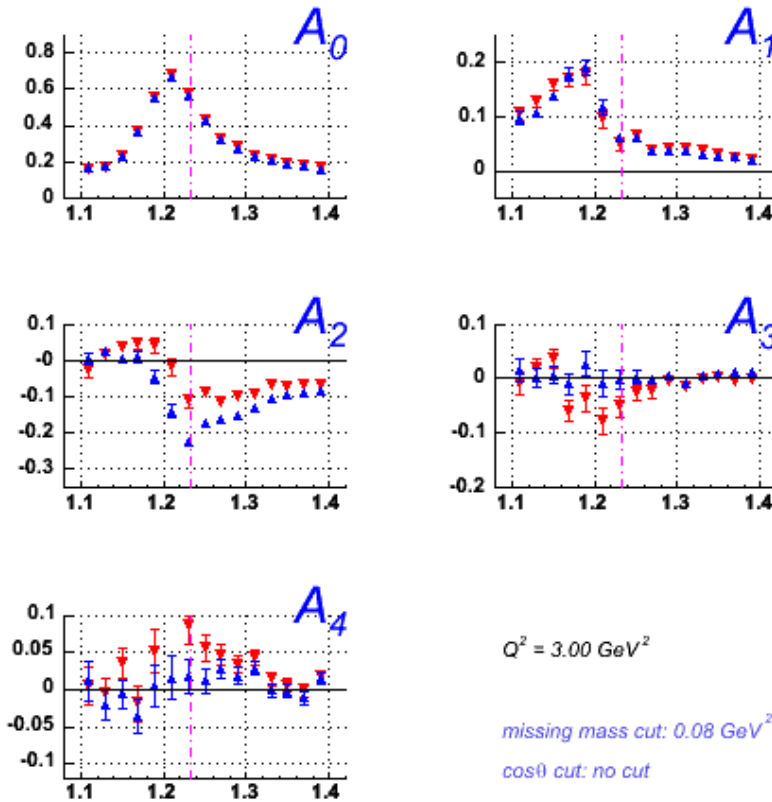


Figure 4.6: The coefficients of the $\sigma_T + \epsilon \sigma_L$ expansions as a function of W for the Invariant and Lorentz method. Blue: Lorentz method. Red: Invariant method. The A_2 coefficient at the Δ pole differs by a factor of two. A non zero value of the A_3, A_4 coefficients would be the signal of $\ell > 1$ components of the (π^0, p) orbital angular momentum.

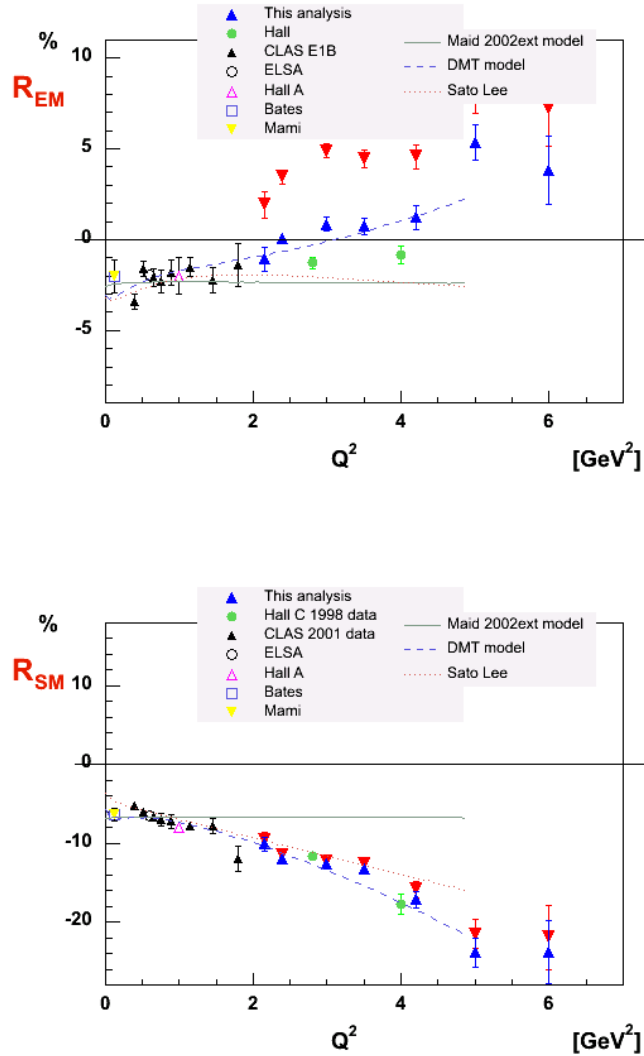


Figure 4.7: The E_{1+}/M_{1+} and S_{1+}/M_{1+} ratios calculated using the truncated multipole analysis for the Invariant and Lorentz method. Blue: Lorentz method. Red: Invariant method. The big discrepancy for E_{1+}/M_{1+} is due to the curvature difference of the $\sigma_T + \epsilon\sigma_L$ at the Δ pole.

4.2 Missing mass cuts

Background coming from a residual $ep \rightarrow e'p'\gamma$ and from two pion production processes has been taken into account in the calculation of the systematic errors by varying the missing mass cut according to Table 4.1.

min (GeV^2)	max (GeV^2)
-0.05	0.08
-0.04	0.075
-0.04	0.07
-0.03	0.065
-0.02	0.06

Table 4.1: Missing mass cuts

The cuts are illustrated in Figure 4.8.

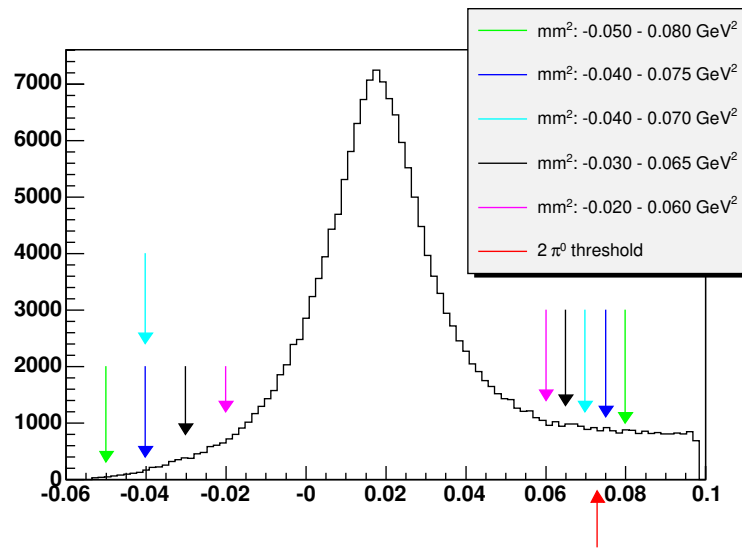


Figure 4.8: Missing mass square distribution for π^0 events and the different cuts used for the systematic study.

The variation of the ratios R_{EM} and R_{SM} for the first and last cut is illustrated in Figure 4.9.

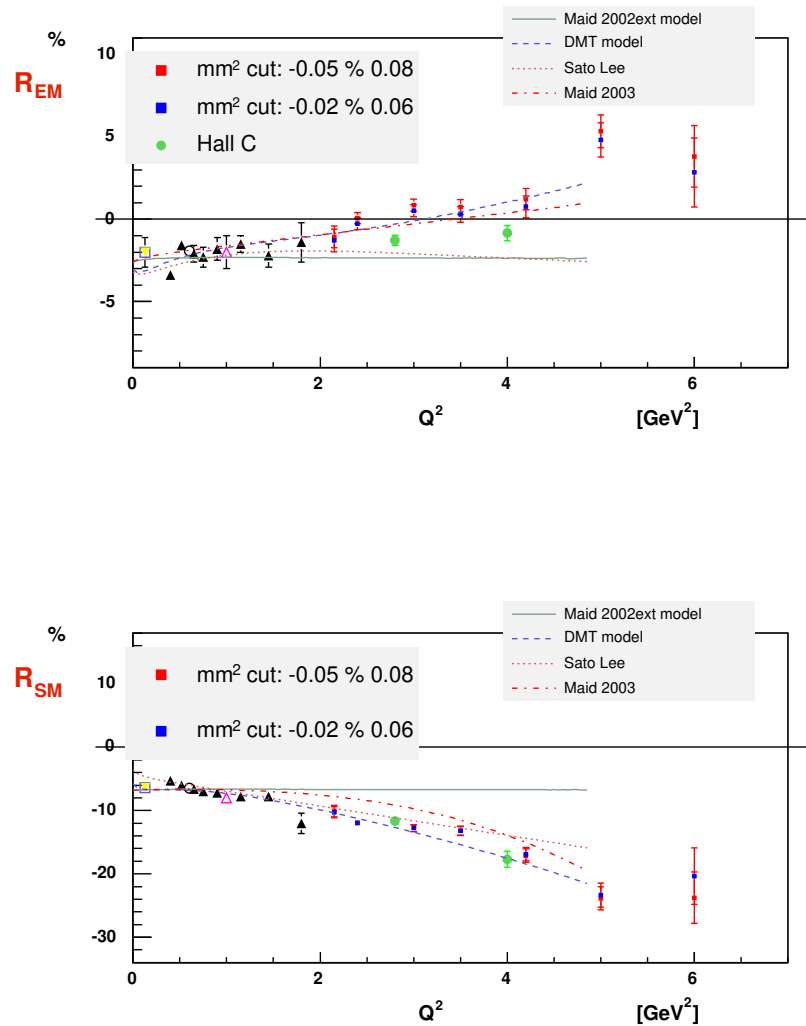


Figure 4.9: Variation of the ratios R_{EM} (top) and R_{SM} (bottom) for the missing mass square cuts: $-0.05 < mm^2 < 0.08$ and $-0.02 < mm^2 < 0.06$

4.3 $\cos \theta^*$ cuts

In Section 4.1.3 it was mentioned that the Invariant method of calculating $\cos \theta^*$ yielded unphysical results at $\cos \theta^*$ extremes due to the smearing introduced by the CLAS detectors and reconstruction software and possibly to the rescattering of the proton in the torus coils. In order to study this possible cause of systematic errors, different cuts have been applied to $\cos \theta^*$. The values are shown in Table 4.2.

min max

-1	1
-0.95	0.95
-0.90	0.90
-0.85	0.85

Table 4.2: $\cos \theta^*$ cuts

The cuts are illustrated in Figure 4.10.

Cos θ^ distributions for $Q^2 = 2.00$, $W = 1.15$, $mm = 1.00$*

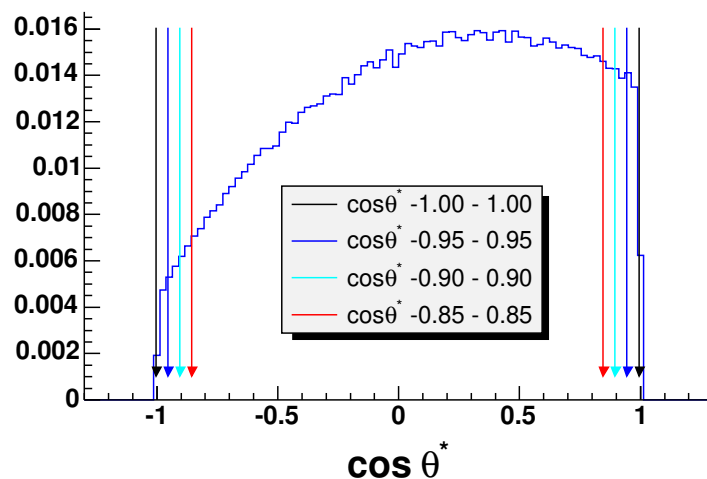


Figure 4.10: Different cuts for $\cos \theta^*$ as shown in Table 4.2. The distribution comes from the MonteCarlo reconstructed events, and it's normalized to 1.

The variation of the ratios R_{EM} and R_{SM} for the first and second cut is illustrated in Figure 4.11.

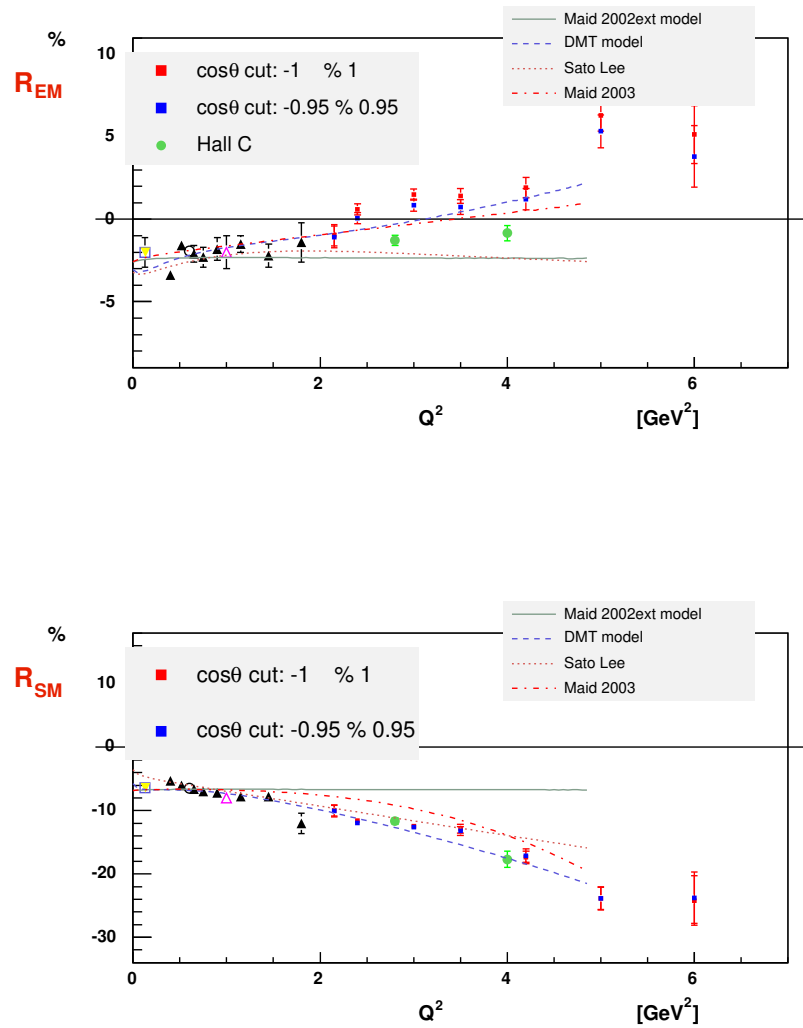


Figure 4.11: Variation of the ratios R_{EM} (top) and R_{SM} (bottom) for the $\cos \theta^*$ cuts: $-1 < \cos \theta^* < 1$ and $-0.95 < \cos \theta^* < 0.95$.

4.4 χ^2 plots for the systematic studies

See

http://www.jlab.org/~ungaro/pi0eprod/bin_ave

for the χ^2 distributions for different cuts in missing mass and $\cos \theta^*$ and for Lorentz/Invariant method.

LITERATURE CITED

- [1] G. Adams et al., *Nucl. Instrum. Meth.* **A465** 414-427 (2001)
- [2] A. Afanasev, I. Akushevich, V. Burkert, K. Joo, *PiN Newslett.* **16**, 343 (2002)
- [3] M. Amarian et al., *NIM A* **460** (2001) 239
- [4] I. Aznauryan , *Phys. Rev. D* **67** (2003)
- [5] I. Aznauryan , *Phys. Rev. D* **68** (2003)
- [6] M. Anselmino, *Rev. Mod. Phys.* **65**, (1993) 1199
- [7] D.Y. Bardin, N.M. Shumeiko, *Nucl. Phys. B* **127**, 242 (1977)
- [8] C. Becchi, G, Morpurgo, *Phys. Lett.* **17** (1965) 352
- [9] V. D. Burkert *Few Body Syst. Suppl.* **9** (1995) 324
- [10] C. E. Carlson *Phys. Rev. D* **34** (1986) 2704
- [11] G.F. Chew, M.L. Goldberger, F.E. Low, Y. Nambu, *Phys. Rev.* **106** (1957) 1345-1337
- [12] F. Close, Z. Li, *Phys. Rev.* **D42**, (1990) 2194
- [13] L.A. Copley, G. Karl, E. Obruk, *Phys. Lett.* **B29**, (1969) 117
- [14] R.M. Davidson, N.C. Mukhopadhyay, R. Wittman, *Phys. Rev. Lett* **56**, (1986) 804
- [15] R. H. Dalitz, D. G. Sutherland *Phys. Rev.* **146** (1966) 1180
- [16] R.M. Davidson, N.C. Mukhopadhyay, R. Wittman, *Phys. Rev.* **D43**, (1991) 871
- [17] D. Drechsel, O. Hanstein, S.S. Kamalov, L. Tiator, *Nucl. Phys.* **A645** (1999) 145-174
- [18] K.S. Egiyan, *CLAS NOTE 99 - 007*
- [19] R. Feuerbach, *PhD thesis*
- [20] R.P. Feynman, *Phys. Rev.* **D3**, (1971) 2706
- [21] V. V. Frolov et al. *Phys. Rev. Lett.* **82** (1999) 45
- [22] O. Hanstein, *Nucl.Phys.* **A632** (1998) 561

LITERATURE CITED

- [23] C. T. Hung, S.N. Yang, T. S. Lee *J. Phys* **G20** (1994) 1531
- [24] N. Isgur, G. Karl, *Phys. Rev.* **D18**, (1978) 4187
- [25] K. Joo, L.C. Smith et al *Phys. Rev. Lett.* **88** (2002) 122001
- [26] S.S. Kamalov, S.N. Yang, D. Drechsel, L. Tiator, *Phys. Rev. Lett.* **83** (1999) 4494
- [27] S.S. Kamalov, S.N. Yang, G. Y. Chen, *Phys. Rev. Lett.* **522** (2001) 27
- [28] G. Knöchlein, D. Drechsel, L.Tiator *Z. Phys.* **A352** 327-343,(1995)
- [29] Valeri Koubarovski, *private communication.*
- [30] Valeri Koubarovski, *private communication.*
- [31] A. Idilbi, X. Ji, J. P. Ma, *hep-ph/0308018*
- [32] C. W. Leeman, D. R. Douglas, G. A. Krafft, *Ann. Rev. Nuc. Part. Sci.*, **51:413-450** (2001)
- [33] G. P. Lepage, S. J. Brodsky *Phys. Rev. D* **22** (1980) 2157
- [34] Mo and Tsai, *Rev. Mod. Phys.* **41** (1969)
- [35] L. Morand, *private communication.*
- [36] S. Morrow, D. Doré, M. Garcon, L. Morand, F. Sabatié, *CLAS internal document*
- [37] B. Niczyporuk, *CLAS NOTE 91 - 001*
- [38] R. Niyazov and L.B. Weinstein, *CLAS NOTE 01 - 013*
- [39] K. Park, *private communication.*
- [40] A.S. Raskin, T.W. Donnelly, *Ann. Phys.*, **C63**, 78 (1989)
- [41] T. Sato, T.S. Lee, *nucl-th/0010025*
- [42] T. Sato, T.S Lee, *Phys. Rev.* **C54**, (1996) 2660
- [43] T. Sato, T.S Lee, *Phys. Rev.* **C63**, (2001)
- [44] Herbert Schildt *C++: The complete reference*, 291, 627 (1998)
- [45] N. M. Shumeiko *Sov. J. Nucl. Phys.*, **29**, 807 (1979)
- [46] A. Silva, D. Urbano, T. Watabe, M. Fiolhais, K. Goeke, *hep-ph/9905326*

LITERATURE CITED

- [47] Elton Smith et al., *NIM A* **432** (1999) 265
- [48] Paul Stoler *Phys. Rev. Lett* **91** vol. 17 (2003) 172303
- [49] M. Ungaro, Ji Li, *CLAS NOTE* 03 - 006
- [50] D. R. Yennie, S. C. Frautschi, H. Suura *Ann. Phys.* **13** 379 (1961)
- [51] R. L. Walker, *Phys. Rev.* **182** (1969) 1729-1748
- [52] M. Warns, H. Schroder, W. Pfeil, H. Rollnik, *Z. Phys. C* **45** (1990) 627
- [53] X. Ji, J. P. Ma, F. Yuan, *Phys. Rev. Lett.* **90** (2003) 241601
- [54] X. Ji, *Phys. Rev. Lett.* **78** (1997) 610

APPENDIX A

Kinematic variables

The relevant 4-vectors for the process in Figure A.1 are listed below.

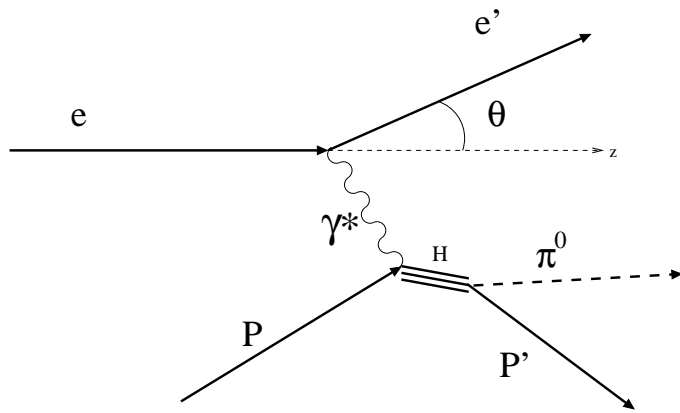


Figure A.1: Schematics of π^0 electroproduction.

e_μ : incident electron, $e_\mu = (E, 0, 0, E)$. E is the beam energy.

e'_μ : scattered electron.

P_μ : target (incident proton), $P_\mu = (M_p, 0, 0, 0)$, M_p being the mass of the proton.

P'_μ : scattered proton.

q_μ : virtual photon, $q_\mu = e_\mu - e'_\mu$.

H_μ : outgoing hadrons mass, $H_\mu = q_\mu + P_\mu$.

x_μ : missing particle, $x_\mu = H_\mu - P'_\mu$.

so that

$$\begin{aligned} W &= \sqrt{H_\mu H^\mu} && \leftarrow \text{outgoing hadron invariant mass} \\ Q^2 &= -q_\mu q^\mu && \leftarrow \text{mass square of the virtual photon} \\ M_x^2 &= \sqrt{x_\mu x^\mu} && \leftarrow eP \text{ missing mass} \end{aligned}$$

APPENDIX B

Summary of cuts used

B.1 Electron particle id cuts

B.1.1 Čerenkov signal cut

Denoting with nphe the ECPB variable, i.e. $10 \times$ number of photoelectrons:

$$nphe > 25$$

B.1.2 Total energy in calorimeter and lower momentum cut

$$Y_{min} \leq E_{TOT}/p \leq Y_{max}$$

where

$$\begin{aligned} Y_{max} &= 0.395332 - 0.044357p + 0.0193197p^2 - 0.00272412p^3 \\ Y_{min} &= 0.137908 + 0.084991p - 0.0245721p^2 + 0.00276102p^3 \end{aligned}$$

These cuts comes from [29].

Furthermore

$$p \geq 0.639$$

from [18].

B.1.3 Inner - Outer energy in calorimeter cut

$$E_{in}/p \geq 0.19 - E_{out}/p$$

B.1.4 Inner / Outer energy cut

$$E_{in}/E_{out} \geq 0.4$$

B.2 Proton particle id cuts

$$0.6 \leq M \leq 1.6$$

B.2.1 Electron fiducial cuts

$$\Delta\phi = C_4 (\sin(\theta - \theta_{cut}))^E$$

$$E = C_3 p^{C_5}$$

$$\theta_{cut} = C_1 + \frac{C_2}{p + C_6}$$

Sector	C_1	C_2	C_3	C_4	C_5	C_6
1	12.0	20.0	0.32	32.0	0.416667	0.14
2	//	20.7	0.36	34.0	//	//
3	//	20.2	0.32	32.0	//	//
4	//	20.5	0.32	32.0	//	//
5	//	20.5	0.29	32.0	//	//
6	//	20.0	0.32	32.0	//	//

B.2.2 Electron bad regions

In what follows p is the electron momentum in units of GeV and θ is the electron angle in units of degrees.

Sector 2:

$$\begin{aligned} 34 - 4\sqrt{p - 1.5} &\leq \theta \leq 35.5 - 4\sqrt{p - 1.5} \\ &\times \\ 26.7 - 4.8\sqrt{p - 1.5} &\leq \theta \leq 27.3 - 4.8\sqrt{p - 1.5} \\ &\times \\ 28.1 - 4.8\sqrt{p - 1.5} &\leq \theta \leq 28.5 - 4.8\sqrt{p - 1.5} \end{aligned}$$

Sector 5:

$$\begin{aligned} 21.3 - 2.4\sqrt{p - 2} &\leq \theta \leq 21 \\ &\times \\ 26.3 - 2.4\sqrt{p - 1.9} &\leq \theta \leq 26.3 + 2.4\sqrt{p - 1.9} \end{aligned}$$

Sector 6:

$$\begin{aligned} 29.5 - 5.2\sqrt{p - 1.5} &\leq \theta \leq 31 - 5\sqrt{p - 1.5} \\ &\times \\ 36 - 3\sqrt{p - 1.5} &\leq \theta \leq 38 - 3\sqrt{p - 1.5} \end{aligned}$$

B.2.3 Proton fiducial cuts

In what follows p is the proton momentum in units of GeV and θ and ϕ are the proton angles in units of degrees.

$$\begin{aligned} a_i &= c_0 + c_1 p + c_2 p^2 \\ b_i &= d_0 + d_1 p + d_2 p^2 \end{aligned}$$

Sector 1:

	c_0	d_0	c_1	d_1	c_2	d_2
a_0, b_0	39.4471	-1.42891	-4.28941	-20.8695	0.0910672	4.85237
a_1, b_1	-5.95718	-0.40323	-0.0915413	4.15143	0.113486	-0.873097
a_2, b_2	0.233019	0.0877448	0.010272	-0.206594	-0.00585689	0.0422065
a_3, b_3	-0.0043921	-0.00209527	-4.57015e-05	0.0038365	8.66512e-05	-0.000787643
a_4, b_4	3.22474e-05	1.40471e-05	-1.63838e-06	-2.40801e-05	-2.99613e-07	5.06479e-06

Sector 2:

	c_0	d_0	c_1	d_1	c_2	d_2
a_0, b_0	44.2525	4.94857	-8.53036	-20.3406	0.481749	4.03726
a_1, b_1	-6.9053	-1.97407	0.769652	4.2043	0.00638363	-0.753544
a_2, b_2	0.281855	0.184416	-0.0321893	-0.218929	-0.000844245	0.0372669
a_3, b_3	-0.00536168	-0.0045072	0.000722783	0.00432631	1.03893e-05	-0.000703947
a_4, b_4	3.88746e-05	3.6027e-05	-6.23593e-06	-3.06811e-05	1.41789e-08	4.85139e-06

Sector 3:

	c_0	d_0	c_1	d_1	c_2	d_2
a_0, b_0	48.8643	13.224	-13.6046	-22.7071	1.54434	3.47116
a_1, b_1	-8.14818	-2.07311	1.59337	3.88685	-0.16267	-0.529604
a_2, b_2	0.370884	0.177999	-0.0920444	-0.193177	0.01175	0.0225649
a_3, b_3	-0.00764513	-0.00419906	0.00230433	0.00365751	-0.000322689	-0.000357837
a_4, b_4	5.84148e-05	3.1048e-05	-2.01461e-05	-2.34094e-05	2.93282e-06	1.75395e-06

Sector 4:

	c_0	d_0	c_1	d_1	c_2	d_2
a_0, b_0	42.7907	-14.6804	0.557686	-4.28155	-1.93386	0.545166
a_1, b_1	-7.06612	2.32197	-0.589287	0.811594	0.366981	-0.0287077
a_2, b_2	0.301463	-0.0327651	0.0330414	-0.0501169	-0.0179363	-0.000611366
a_3, b_3	-0.00580282	-0.000419906	-0.000743318	0.00126087	0.000384465	2.22975e-05
a_4, b_4	4.16703e-05	8.18104e-06	5.97558e-06	-1.03781e-05	-3.01804e-06	-2.27518e-07

Sector 5:

	c_0	d_0	c_1	d_1	c_2	d_2
a_0, b_0	52.0838	4.57043	-15.8603	-17.2084	1.38223	2.43805
a_1, b_1	-8.31577	-0.143877	3.14067	2.7247	-0.389671	-0.325088
a_2, b_2	0.393192	0.0654633	-0.22493	-0.1203	0.0333465	0.00937443
a_3, b_3	-0.00862513	-0.00157316	0.00610496	0.00175928	-0.000950539	1.01077e-05
a_4, b_4	7.12059e-05	1.11448e-05	-5.65199e-05	-7.58069e-06	8.93644e-06	-1.50299e-06

Sector 6:

	c_0	d_0	c_1	d_1	c_2	d_2
a_0, b_0	66.7155	-4.17306	-22.5136	-17.1484	4.17892	3.71364
a_1, b_1	-10.6179	-0.407384	4.06603	4.34246	-0.859252	-0.834831
a_2, b_2	0.47953	0.122555	-0.249083	-0.258914	0.0558406	0.0479698
a_3, b_3	-0.00970942	-0.00360644	0.00620864	0.00583929	-0.00141667	-0.00107312
a_4, b_4	7.30481e-05	3.08354e-05	-5.37051e-05	-4.52976e-05	1.23011e-05	8.33686e-06

$$\phi_{MIN} = a_0 + a_1\theta + a_2\theta^2 + a_3\theta^3 + a_4\theta^4$$

$$\phi_{MAX} = b_0 + b_1\theta + b_2\theta^2 + b_3\theta^3 + b_4\theta^4$$

B.2.4 Proton bad regions

In what follows p is the proton momentum in units of GeV and θ is the proton angle in units of degrees.

Sector 2:

$$31 + 8.7\sqrt{p - 0.9} \leq \theta \leq 33.4 + 8\sqrt{p - 0.9}$$

×

$$24.7 \leq \theta \leq 27.2$$

Sector 3:

$$31.5 + 9.0\sqrt{p - 0.9} \leq \theta \leq 37.7 + 6\sqrt{p - 0.9}$$

Sector 5:

$$13.5 - 0.38(p - 4)^2 \leq \theta \leq 12.2 + 3.5\sqrt{p - 0.9}$$

×

$$10.1 \leq \theta \leq 11.2$$

×

$$18 + \sqrt{p - 0.9} \leq \theta \leq 19 + \sqrt{p - 0.9}$$

×

$$22.6 + 1.3\sqrt{p - 0.9} \leq \theta \leq 24.6 + 1.3\sqrt{p - 0.9}$$

Sector 6:

$$\begin{aligned} 26 - 1.3(p - 3.5)^2 &\leq \theta \leq 29.2 - 1.9(p - 3.2)^2 \\ &\times \\ 10 + 14\sqrt{p - 0.9} &\leq \theta \leq 29.2 - 1.9(p - 3.2)^2 \\ &\times \\ 30.7 + 5.5\sqrt{p - 0.9} &\leq \theta \leq 32.4 + 5\sqrt{p - 0.9} \\ &\times \\ 6.5 + 9\sqrt{p - 0.9} &\leq \theta \leq 7.5 + 9\sqrt{p - 0.9} \end{aligned}$$

APPENDIX C

$\cos \theta^*$ plots

$\cos \theta^$ distributions for $Q^2 = 2.00$, $W = 1.25$, $mm = 0.08$*

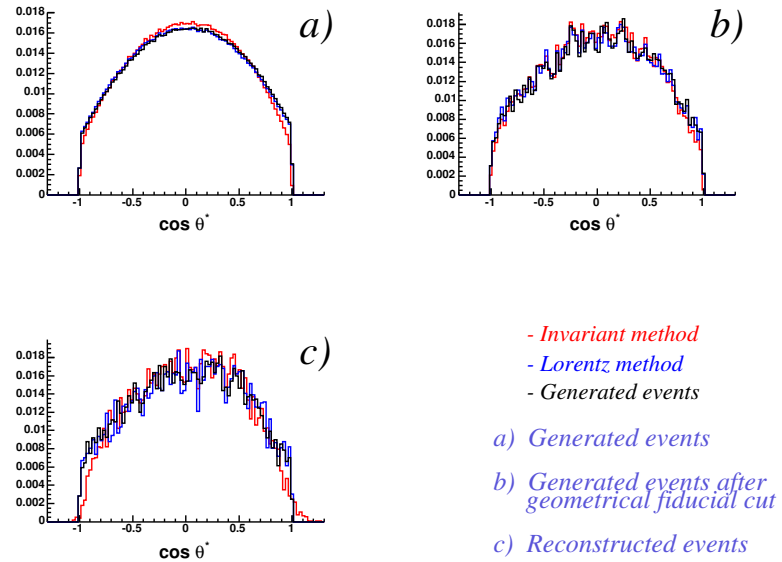


Figure C.1: Generated, Lorentz and Invariant reconstructed $\cos\theta^*$ distribution for $Q^2 = 2$ GeV^2 . All histograms are normalized to 1.

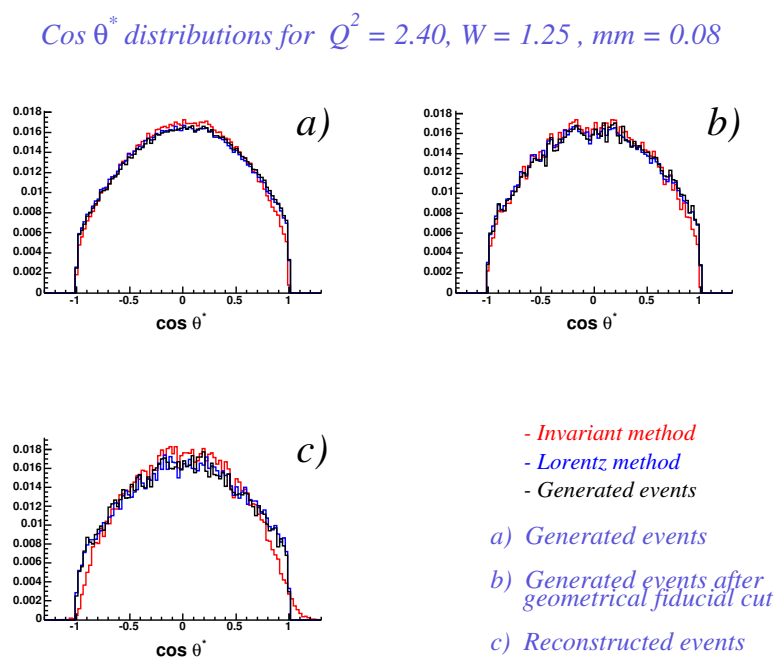


Figure C.2: Generated, Lorentz and Invariant reconstructed $\cos\theta^*$ distribution for $Q^2 = 2.4 \text{ GeV}^2$. All histograms are normalized to 1.

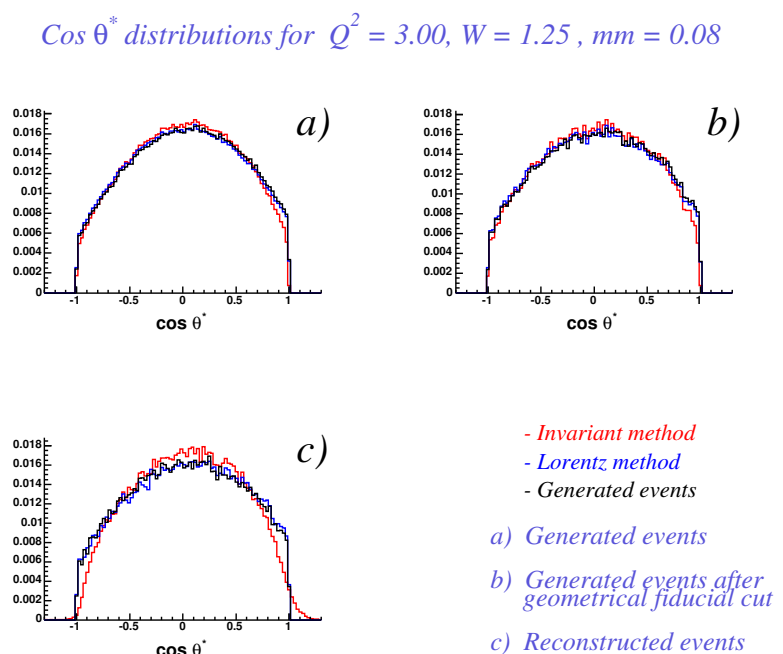


Figure C.3: Generated, Lorentz and Invariant reconstructed $\cos\theta^*$ distribution for $Q^2 = 3$ GeV^2 . All histograms are normalized to 1.

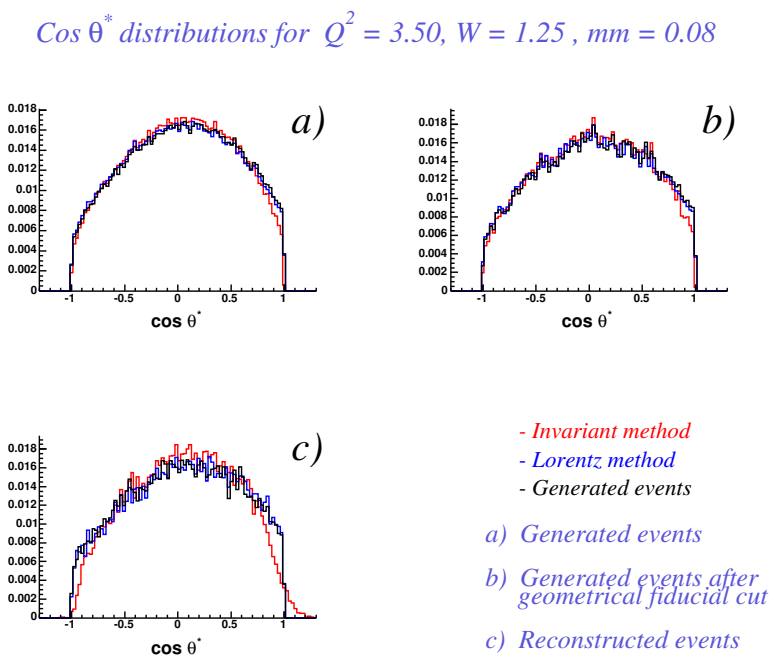


Figure C.4: Generated, Lorentz and Invariant reconstructed $\cos\theta^*$ distribution for $Q^2 = 3.5$ GeV^2 . All histograms are normalized to 1.

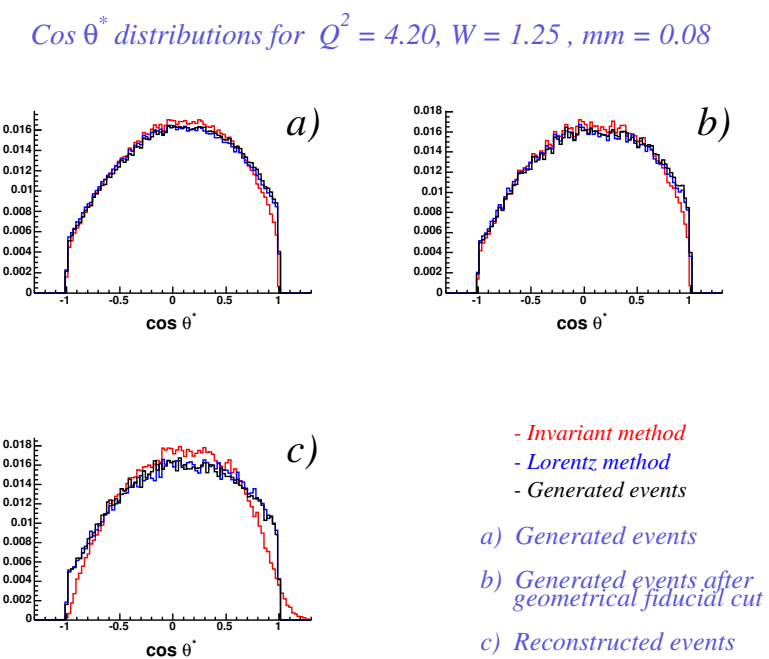


Figure C.5: Generated, Lorentz and Invariant reconstructed $\cos\theta^*$ distribution for $Q^2 = 4.2$ GeV^2 . All histograms are normalized to 1.

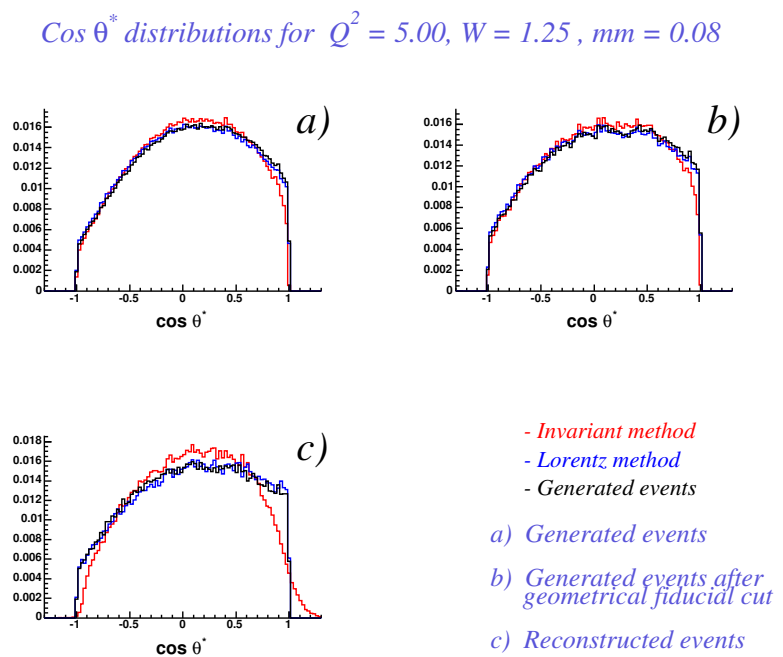


Figure C.6: Generated, Lorentz and Invariant reconstructed $\cos\theta^*$ distribution for $Q^2 = 5$ GeV^2 . All histograms are normalized to 1.

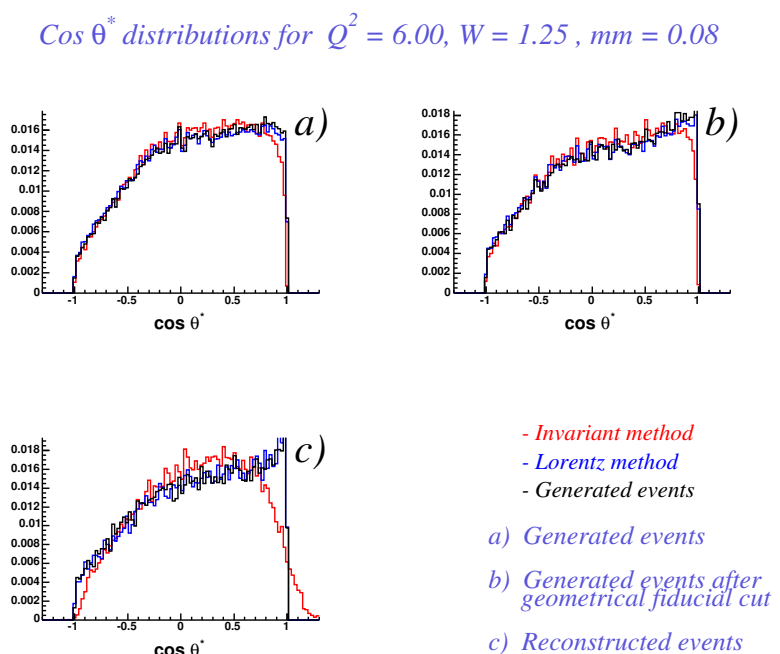


Figure C.7: Generated, Lorentz and Invariant reconstructed $\cos\theta^*$ distribution for $Q^2 = 6 \text{ GeV}^2$. All histograms are normalized to 1.